The recent dynamics of Moscow University Glacier and Moscow University Ice Shelf, East Antarctica (1963 – 2022)

CONSTANCE MARY HARPUR

The recent dynamics of Moscow University Glacier and Moscow University Ice Shelf, East Antarctica (1963 – 2022)

Constance M. Harpur

Thesis submitted for the degree of MSc by Research

Department of Geography

Durham University

Abstract

Mass loss from the Antarctic Ice Sheet is dominated by ice discharge through outlet glaciers, many of which are buttressed by peripheral ice shelves. In Wilkes Land, East Antarctica, an ocean-driven increase in ice flux from several large outlet glaciers has caused accelerated mass loss over recent decades. Wilkes Land overlies the Aurora Subglacial Basin (ASB), which contains an ice volume large enough to raise global sea level by 5 m and is potentially susceptible to pervasive retreat. However, ice dynamics within some areas of Wilkes Land remain largely unstudied. This includes Moscow University Glacier (MUG) and Moscow University Ice Shelf (MUIS), which regulate ice discharge from a catchment containing 128 cm of potential sea level rise within the ASB and are subject to intrusions of warm Circumpolar Deep Water. Employing optical satellite imagery and remote sensing datasets to record changes in terminus position, ice surface velocity, ice surface elevation, grounding line location and sea ice distribution, this thesis aims to investigate the ice dynamics of MUIS and MUG between 1963 and 2022. Migration of the MUIS ice front is limited to the unconfined ice shelf region. Both MUG and MUIS exhibited negligible change in flow velocity between 2000 and 2021, and the results suggest limited grounding line retreat of 1.4 km between 1996 and 2017 (~67 m yr^{-1}). Ice surface elevation remained stable from 1993 to 2010, but MUG was recorded to thin at an accelerated rate (0.86 m yr^{-1}) between 2011 and 2016, and regions of enhanced surface lowering were observed to correlate with areas of faster ice flow. Overall, these findings imply that MUG and MUIS have remained largely stable in recent decades, but may be starting to exhibit the early indicators of dynamic change. It is suggested that topography exerts critical stabilising stresses on MUIS, enhancing its capacity to buttress the flow of MUG. Continued monitoring of MUG and MUIS, as well as topographically-constrained ice flow modelling, will be important in understanding the response of the Moscow University catchment to future ocean forcing.

List of Figures

List of Tables

List of Abbreviations

AIS	Antarctic Ice Sheet
AIS CCI	Antarctic Ice Sheet Climate Change Initiative
AMSR-E	Advanced Microwave Scanning Radiometer -EOS
AP	Antarctic Peninsula
ASB	Aurora Subglacial Basin
DInSAR	Differential Interferometric Synthetic Aperture Radar
DIT	Dalton Iceberg Tongue
DP	Dalton Polynya
DSW	Dense Shelf Water
EAIS	East Antarctic Ice Sheet
ENVEO	Environmental Earth Observation Information Technology GmbH
ERS-1/2	European Remote-Sensing Satellite
ETM+	Enhanced Thematic Mapper Plus
GL	Grounding line
GMSL	Global mean sea level
GRACE	Gravity Recovery and Climate Experiment
GrIS	Greenland Ice Sheet
IBSCO	International Bathymetric Chart of the Southern Ocean
IceSAT-2	Ice, Cloud, and land Elevation Satellite-2
IPCC	Intergovernmental Panel on Climate Change
ITS_LIVE	Inter-mission Time Series of Land Ice Velocity and Elevation
LIMA	Landsat Image Mosaic of Antarctica
MAR	Modèle Atmosphérique Régionale
mCDW	Modified Circumpolar Deep Water
MEaSUREs	Making Earth System Data Records for Use in Research Environments
MICI	Marine ice cliff instability
MISI	Marine ice sheet instability
MSS	Multispectral Scanner System
MOA	Mosaic of Antarctica
MODIS	Moderate Resolution Imaging Spectroradiometer
MUG	Moscow University Glacier
MUIS	Moscow University Ice Shelf
OLI	Operational Land Imager

RACMO	Regional Atmospheric Climate Model
RAMP	RADARSAT Antarctic Mapping Project
RCP	Representative Carbon pathway
REMA	Reference Elevation Model of Antarctica
RSB	Recovery Subglacial Basin
SAR	Synthetic Aperture Radar
SEC	Surface elevation change
SLC	Single Look Complex
SLE	Sea level equivalent
SLR	Sea level rise
SMB	Surface mass balance
TIS	Totten Ice Shelf
WAIS	West Antarctic Ice Sheet
WSB	Wilkes Subglacial Basin

Statement of copyright

Acknowledgements

I would like to thank my supervisors, Professor Chris Stokes and Professor Stewart Jamieson, who helped to shape my interest in glaciology as an undergraduate student and for whose guidance, encouragement and patience over the course of this project I am hugely grateful.

My thanks also go to those who make up the wider Department of Geography at Durham, for four brilliant years of learning.

Finally, I would like to thank my friends and family, for all of their love and support.

1 Introduction

1.1 Rationale

The Greenland (GrIS) and Antarctic (AIS) ice sheets hold enough water to raise global mean sea level (GMSL) by ~65 metres (Morlighem et al., 2020). Driven by climate and ocean forcing, accelerating mass loss from these major ice masses led to 21 ± 2 mm of sea level rise (SLR) between 1992 and 2020 (Rignot et al., 2019; The IMBIE Team, 2020; Velicogna et al., 2020). This contribution is expected to increase throughout the twenty-first century (Noble et al., 2020), exposing an estimated 630 million people to coastal flooding by 2100 if carbon emissions remain unchecked (Kulp and Strauss, 2019). In the past, ice sheets have responded sensitively to atmospheric and ocean warming analogous with projections for the near future (Overpeck et al., 2006; Carlson and Winsor, 2012; Dutton et al., 2015; DeConto and Pollard, 2016). Records show that global sea level was 6 to 9.3 m higher than present during the last interglacial (Marine Isotope Stage 5e, 130,000 to 115,000 years ago), implying significant retreat of both the AIS and the GrIS (Kopp et al., 2009; 2013) and therefore indicating their vulnerability to future change (Joughin and Alley, 2011).

The rate of change in ice sheet mass – the mass balance – is a result of the difference between mass gained from precipitation and lost through processes of ablation (Hanna et al., 2013). Since the 1990s, over half of GrIS mass losses have been driven by melt-induced surface runoff (The IMBIE Team, 2020), which has increased in line with regional atmospheric warming (Hanna et al., 2012; Fettweis et al., 2013; van den Broeke et al., 2016; Trusel et al., 2018). By comparison, mass loss from the AIS is dominated by ice discharge through outlet glaciers which drain into the Southern Ocean (Rignot et al., 2011; Pritchard et al., 2012; Shepherd et al., 2019).

Peripheral ice shelves modulate drainage by buttressing the flow of more than 80% of Antarctica's grounded ice (Figure 1.1; Pritchard et al., 2012; Fürst et al., 2016; Gudmundsson et al., 2019). Recently, ocean-forced basal melting has caused some ice shelves to thin (Pritchard et al., 2012; Rignot et al., 2013; Hogg et al., 2021) and calve (Greene et al., 2022) at increasing rates (Paolo et al., 2015), leading to the acceleration (Mouginot et al., 2017), drawdown (Pritchard et al., 2009; Schröder et al., 2019) and retreat (Christie et al., 2016; Konrad et al. 2018; Milillo et al., 2022) of outlet glaciers. Much of the observed change has been concentrated within the Amundsen Sea sector of Western Antarctica, where enhanced discharge from Pine Island and Thwaites glaciers has led to a widespread and persistent dynamic imbalance (Sutterly et al., 2014; Seroussi et al., 2017; Shepherd et al., 2019). As a result, annual mass loss from the AIS has increased by almost

350% over the past three decades (The IMBIE Team, 2018). Observations of recent changes in ice shelf and glacier dynamics are critical to understanding overall trends in Antarctic mass balance, and in turn represent an important constraint on projections of future mass loss and sea level rise (Hanna et al., 2020; Slater et al., 2020).

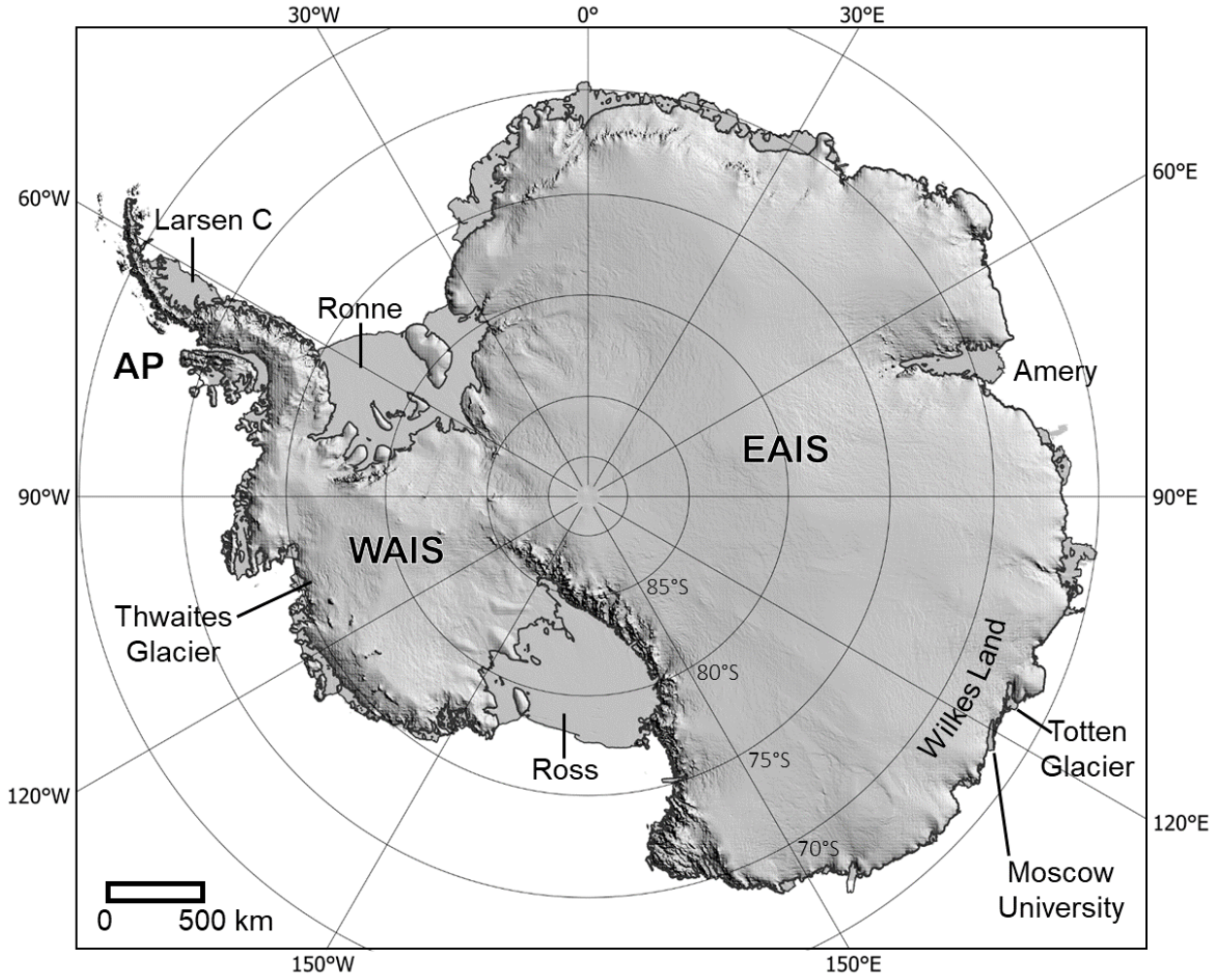

Figure 1.1: The Antarctic Ice Sheet, including the West Antarctic Ice Sheet (WAIS), East Antarctic Ice Sheet (EAIS) and Antarctic Peninsula (AP). Background image is the Reference Elevation Model of Antarctica (REMA; Howat et al., 2019) and the grounding and coast lines are from the MEaSUREs Antarctic Boundaries dataset (Rignot et al., 2016).

Following a growth in scientific attention over the past 50 years, the dynamics of the West Antarctic Ice Sheet (WAIS; ~5.3 m sea level equivalent, SLE, Morlighem et al., 2020) are increasingly well understood (Noble et al., 2020). By comparison, the mass balance of the East Antarctic Ice Sheet (EAIS) remains uncertain (Stokes et al., 2022), with large (~100 Gt yr^{-1}) discrepancies between estimates which suggest either minor mass gains (e.g. Gardner

et al., 2018; Smith et al., 2020; Zwally et al., 2021) or losses (Rignot et al., 2019). Importantly, recent work has observed regions of dynamic loss in the EAIS (Shen et al., 2018; The IMBIE Team, 2018; Miles et al., 2022). This includes Wilkes Land, where ice shelf melting due to incursions of warm coastal Circumpolar Deep Water (mCDW) has caused some major outlet glaciers to thin and retreat at rates similar to those reported from the WAIS (Rintoul et al., 2016; Roberts et al., 2018; Gardner et al., 2018; van Wijk et al., 2022). Indeed, numerical modelling predicts substantial mass loss from Wilkes Land in the future (DeConto and Pollard, 2016), and retrograde slopes in the underlying bed topography of the wider Aurora Subglacial Basin (ASB; Morlighem et al., 2020) may facilitate runaway retreat if fringing ice shelves were to collapse (Greenbaum et al., 2015; Golledge et al., 2015; Sun et al., 2016; Thompson et al., 2018). The EAIS contains 90% (~58 m) of the total AIS SLE (Morlighem et al., 2020), ~ 5.1 metres of which are held in the ASB (Greenbaum et al., 2015). In turn, there is now an increasing focus on the EAIS and its response to climate and ocean forcing.

Located on the Wilkes Land coastline, Moscow University Glacier (MUG) and Moscow University Ice Shelf (MUIS) drain ice from a catchment which holds 128 cm of potential sea level rise within the ASB. Although recent observations have identified high rates of basal thinning at MUIS (Khazendar et al., 2013; Schodlok et al., 2016), the dynamics of both MUIS and MUG have largely been considered only as part of wider regional mass balance calculations (Velicogna et al., 2020; Mohajerani et al., 2018). Importantly, over 90% of MUIS is calculated to restrict inland flow (Fürst et al., 2016), and submarine melting is expected to increase through the next two centuries (Sun et al., 2016) as the Southern Ocean warms (Herraiz-Borreguero and Garrabato, 2022). As such, an improved understanding of the dynamics of MUIS and MUG is crucial in order to constrain predictions of their future stability.

1.2 Research aim and objectives

1.2.1 Research aim

This study aims to investigate the ice dynamics of Moscow University Glacier and Moscow University Ice Shelf over recent decades (1963 – 2022), and consider the drivers of observed behaviour. To meet this aim, five key objectives have been identified.

1.2.2 Objectives

1 Use satellite imagery to record a time series of changes in the MUIS ice front position, from 1963 to 2022.

2 Investigate interannual changes in ice surface velocity on MUG and MUIS between 2000 and 2021, using ENVEO and ITS_LIVE Antarctic regional velocity mosaics.

3 Use secondary datasets to derive a time series of surface elevation change over MUG (1993 – 2020) and asses the spatial pattern of total surface elevation change within grounded ice regions of the study area (2003 – 2019).

4 Assess recent grounding line change at MUG between 1996 and 2021 using a combination of existing grounding line datasets.

5 Record changes in sea ice distribution and the extent of the Dalton Iceberg Tongue between 1963 and 2022 from satellite imagery, to compare to observed changes in terminus position, velocity and elevation.

1.3 Study area

Moscow University Glacier (67°S 118°E) is located on the Sabrina Coast, Wilkes Land, 160 km east of Totten Glacier and 246 km west of Blair Glacier (Fig. 1.2). The main tributary initiates within the Sabrina Subglacial Basin and reaches speeds of 380 m yr^{-1} at the grounding line (Rignot et al., 2017). Here, the glacier detaches from its bed and flows into Moscow University Ice Shelf (67°S 121°E). Together, MUG and MUIS modulate ice flux from an inland catchment which is 221,595 km^2 and holds 128 cm of eustatic sea level potential (Rignot et al., 2019) within the larger Aurora Subglacial Basin.

MUIS is a large (~4250 km^2), long (~160 km) and relatively narrow ice shelf which increases from 13 to 36 km wide between the grounding line and the terminus. This geometry arises from the positioning of MUIS above the Reynolds Trough (Young et al., 2011), where it sits confined between the coastline and a narrow topographic peninsula extending along the seaward edge of the ice shelf to the Dalton Rise (Gwyther et al., 2014). The peninsula, which is not especially well resolved within existing topographic models (e.g. BedMachine), is raised above sea level and hosts ice independent from the main trunk of flow. Notably, MUIS differs from nearby outlet glaciers and ice shelves which are typically either unconfined (e.g. Voyeykov Ice Shelf (Arthur et al., 2021) and Holmes Glacier (Miles et al., 2017)) or have a higher width-to-length ratio (e.g. Totten Ice Shelf (TIS); Li et al., 2016). In this respect, MUIS more closely compares to the fjord-confined floating tongues of Greenlandic outlet glaciers

such as Petermann (Nick et al., 2012). A second, smaller (<1150 km^2) ice shelf (MUIS West in Fig. 1.2) with less buttressing capacity (>40% passive ice; Fürst et al., 2016) is grounded on several pinning points between MUIS and Totten.

A small tributary (Tributary A) feeds the middle section of MUIS, where ice flow velocity reaches ~590 m yr^{-1}. Velocity further increases along the length of the ice shelf, exceeding 1100 m yr^{-1} at the ice front where MUIS terminates in Paulding Bay. Two further outlets – herein referred to as Outlet East and Outlet West – drain into the Southern Ocean via breaches in the topography along MUIS' seaward margin.

MUIS has a shallow surface gradient; its elevation decreases by ~215 m over 160 km between the grounding line and terminus (Howat et al., 2019). Ice thickness generally increases with proximity to the grounding line (from ~250 to ~2400 m; Morlighem et al., 2020), but simulated basal melt rates (Gwyther et al., 2014) and surface elevation change estimates (Rignot et al., 2013; Khazendar et al., 2013; Smith et al., 2020) suggest regions of preferential thinning and thickening across the ice shelf. Between 2003 and 2019, these height-change measurements ranged spatially from -1.4 to 4.7 m yr^{-1} (Smith et al., 2020).

Previous work has related basal thinning rates at MUIS to the activity of the Dalton Polynya (DP; 66°S 121°E) (Khazendar et al., 2013; Gwyther et al., 2014; Silvano et al., 2017). The DP is a latent-heat polynya sustained by sea ice production within the Dalton Iceberg Tongue (DIT) (Massom et al., 1998; Orsi and Webb, 2022), which is a large (>9000 km^2 in December 2001), persistently recurring (Fraser et al., 2021) area of landfast sea ice abutting the MUIS terminus. A smaller polynya is located east of the DIT. Landfast sea ice is understood to influence ice shelf melt rates along the Sabrina Coast (Van Achter et al., 2022), and has been shown to exert a stabilising back-stress on Totten Glacier (Greene et al., 2018) and other Wilkes Land outlets (e.g. Miles et al., 2017). However, an observational record of the DIT and its relationship to MUIS dynamics has not yet been produced.

The bay between Totten and MUIS is approximately 245 km wide and features a deep (>500 m) trough (Nitsche et al., 2017) which facilitates poleward inflow of mCDW from the continental slope across the shelf break (Fig. 1.3) (Silvano et al., 2019; Bensi et al., 2021; Hirano et al., 2021). In turn, oceanographic surveys have recorded warm waters (>0.6°C) up to 900 m deep on the continental shelf close to the MUIS and Totten ice fronts (Williams et al., 2011; Rintoul et al., 2016; Silvano et al., 2017, 2019). MUG is grounded well below sea level; a retrograde slope in the underlying bed topography extends ~10 km inland of the grounding line and reaches -2290 ± 54 m deep (Morlighem et al., 2020). This means that

mCDW intrusions into the ice shelf cavity may cause unstable retreat of MUG in the near future (Schoof, 2007; Sun et al., 2016). Further, whilst the main flow unit occupies a prograde slope rising to -364 ± 45 m, inland-deepening troughs within the wider catchment (Roberts et al., 2011), also marine based, raise the possibility of marine ice sheet instability (MISI; Greenbaum et al., 2015).

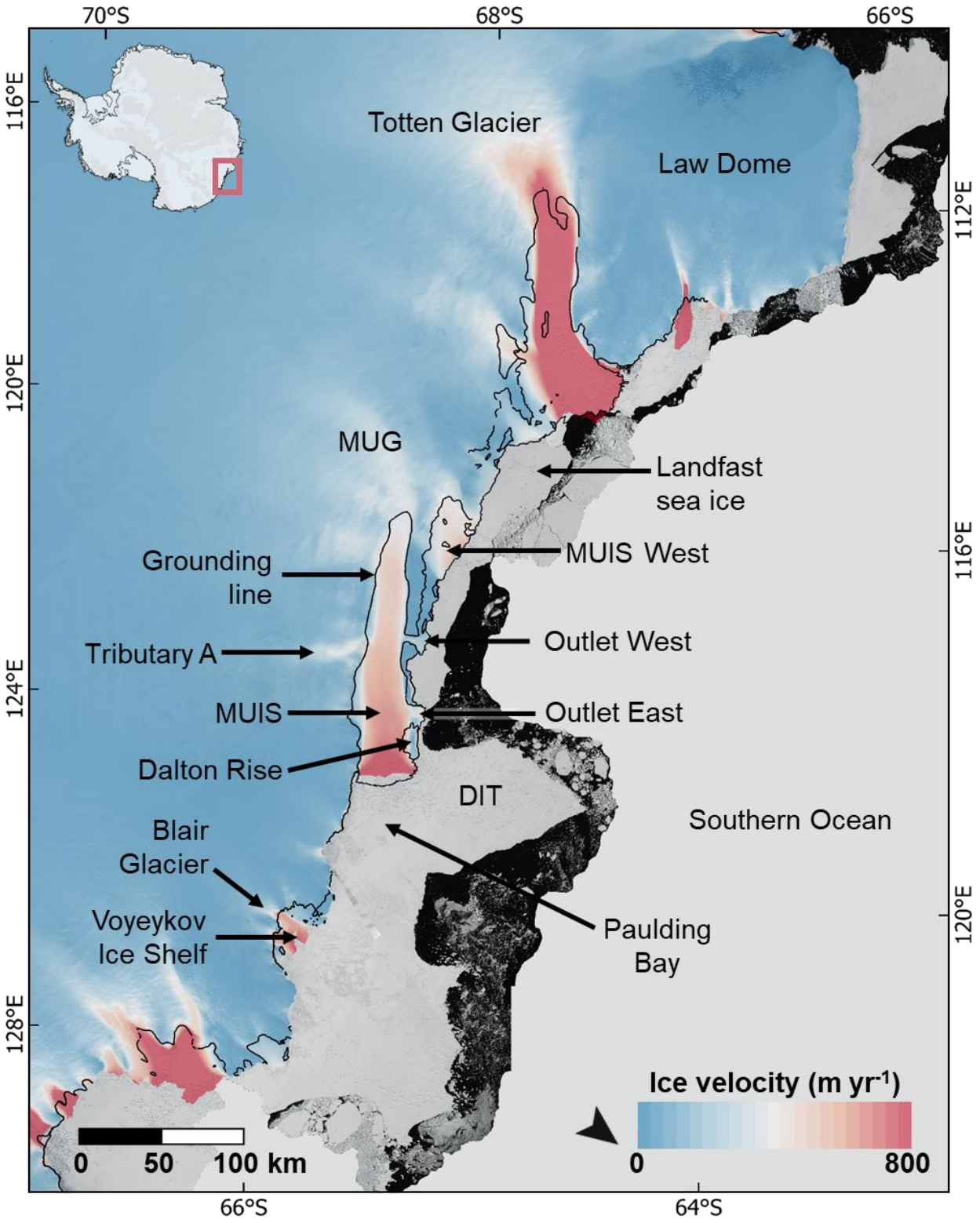

Figure 1.2: Location map of Moscow University Glacier (MUG) and Moscow University Ice Shelf (MUIS), Wilkes Land, East Antarctica. Background image is the Landsat Image Mosaic of Antarctica (LIMA; Bindschadler et al., 2008), comprising imagery acquired between 1999 and 2003, overlain with MEaSUREs ice flow velocity (Rignot et al., 2017). Grounding line is the MEaSUREs 1996 grounding line (Rignot et al., 2016). The ice front was manually delineated from underlying LIMA imagery.

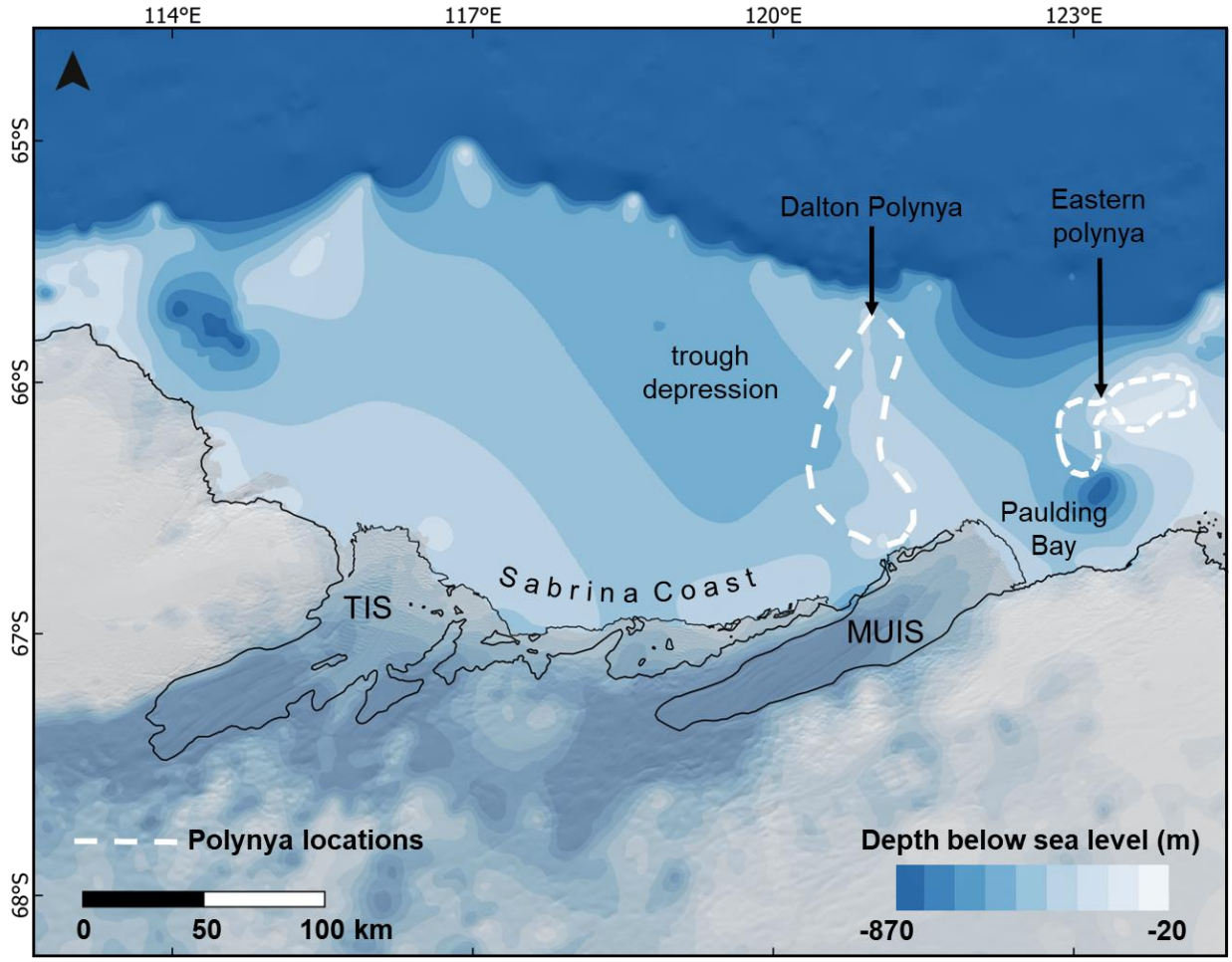

Figure 1.3: International Bathymetric Chart of the Southern Ocean V1 (IBSCO; Arndt et al., 2013) bathymetric map of the Sabrina Coast. Ice surface is the Reference Elevation Model of Antarctica (REMA; Howat et al., 2019). Approximate polynya locations are delineated from Figure 6 in Khazendar et al. (2013).

1.4 Thesis structure

Following the Introduction, this thesis consists of five chapters. **Chapter 2** presents a review of the key literature covering Antarctic ice sheet mass balance, including the mass balance of the AIS, WAIS, AP and EAIS (2.1). It then focusses on past and recent changes in the AP (2.2) and the WAIS (2.3). This is followed by a section on the East Antarctic Ice Sheet (2.4), including its past stability (2.4.1) and present-day ice dynamics (2.4.2), with a focus on recent outlet glacier behaviour in Wilkes Land (2.4.2.1). An appraisal of previous work on Moscow University Glacier and Moscow University Ice Shelf (2.4.2.2) and future projections of EAIS mass balance (2.4.2.3) follow.

Chapter 3 details the datasets and methods used in this study, chosen in accordance with

the objectives outlined above. The results are presented in **Chapter 4**. These include recorded changes in ice front position (1963 – 2022); ice surface velocity on MUIS (2000 – 2018) and MUG (2010 – 2018); the surface elevation of grounded ice areas (1993 – 2020); the grounding line location (1996 – 2020); and mapped sea ice distribution (1963 – 2022).

A discussion of these results is presented in **Chapter 5**, as well as a review of the study limitations and suggestions for future research at MUIS and MUG. Finally, **Chapter 6** presents a summary of the key findings. Additional figures and tables are provided within the **Appendix**.

2 A review of Antarctic Ice Sheet mass balance

2.1 Estimates of Antarctic Ice Sheet mass balance

With a sea level equivalent of 57.9 ± 0.9 m (Morlighem et al., 2020), the Antarctic Ice Sheet (AIS) is the greatest potential contributor to global sea level rise (Oppenheimer et al., 2019; Noble et al., 2020). Observations of ice sheet mass balance are critical to understanding the relationship between ice sheet change and contemporary sea level (Hanna et al., 2013; Ritz et al., 2017), as well as for forcing numerical simulations of ice sheet response to future climate scenarios (Aschwanden et al., 2021). Recent advances in satellite remote sensing and the modelling of surface mass balance (SMB; the difference between mass gained via accumulation and lost via processes of ablation on the ice sheet surface (Kittel et al., 2021)) and glacial isostatic adjustment (GIA; the solid Earth response to the loading and unloading of ice (Whitehouse, 2018)) mean that changes in the mass balance of the GrIS and the AIS can now be monitored with improved frequency and accuracy (Chen et al., 2009; Vaughan et al., 2013). To date, Antarctic mass balance has been estimated via three methods (Hanna et al., 2013; Briggs et al., 2016; The IMBIE Team, 2018). The volumetric approach uses laser or radar altimetry data to record changes in the surface elevation of the ice sheet, which are converted to overall mass change (e.g. Pritchard et al., 2009; McMillan et al., 2015; Shepherd et al., 2019; Smith et al., 2020). The input-output method – or mass budget method – finds the net difference between accumulated snowfall, derived from models of surface mass balance, and mass outputs at the ice sheet margin, which are inferred from observations of ice discharge across the grounding line (e.g. Joughin et al,. 1999; Rignot et al., 2011b; Rignot et al., 2019). Gravimetric techniques employ the Gravity Recovery and Climate Experiment (GRACE) satellites to directly measure monthly centimetre-scale changes in ice sheet mass as a function of variations in Earth's gravity field (e.g. Velicogna and Wahr, 2006; Pritchard et al., 2010; Harig and Simons, 2015; Zwally et al., 2015; Velicogna et al., 2020). Over the past three decades, these approaches have been used to produce over 150 estimates of Antarctic mass balance (Briggs et al., 2016; The IMBIE Team, 2018). Whilst published assessments often agree across common regions and time frames (The IMBIE Team, 2018), systematic differences between the results of different methods mean that some estimates show significant disparities at the ice sheet-wide scale (Hanna et al., 2013), frequently accompanied by high levels of uncertainty (Chen et al., 2009; Noble et al., 2020).

Despite this uncertainty, there is general agreement that the AIS has been losing mass since the 1970s, and that the rate of mass loss has recently accelerated (Rignot et al., 2011c;

Shepherd et al., 2012; Luthcke et al., 2013; Velicogna et al., 2014; Williams et al., 2014; Harig and Simons, 2015; Bamber et al., 2018; Gardner et al., 2018; The IMBIE Team, 2018; Rignot et al., 2019; Diener et al., 2021). Using the results of 24 independent studies, the latest reconciliation of mass balance estimates found a continent-wide mean mass loss of -109 ± 56 Gt yr^{-1} between 1992 and 2017, where the average rate of loss increased from -49 ± 67 to -219 ± 43 Gt yr^{-1} between the first and final five years of the dataset (Fig. 2.1; The IMBIE Team, 2018). Importantly, the rate at which mass losses are outpacing mass gains is spatially variable (Fig. 2.2; Shepherd et al., 2019; Smith et al., 2020). To date, the imbalance signal has been dominated by dynamic loss from the WAIS, with recent estimates suggesting average rates of -94 ± 27 Gt yr^{-1} for the 1992 – 2017 period (The IMBIE Team, 2018) and -214 ± 51 Gt yr^{-1} between 2008 and 2015 (Gardner et al., 2018). Losses from the Antarctic Peninsula (AP) accounted for almost 20% of total AIS mass loss between 1992 and 2017, accelerating at a rate of 15 Gt yr^{-2} since 2000 (The IMBIE Team, 2018). These changes have been linked to the ocean-driven basal melting of floating ice shelves and, in the AP, atmospheric forcing under a warming climate (e.g. Turner et al., 2017; Thompson et al., 2018; Holland et al., 2019; Smith et al., 2020).

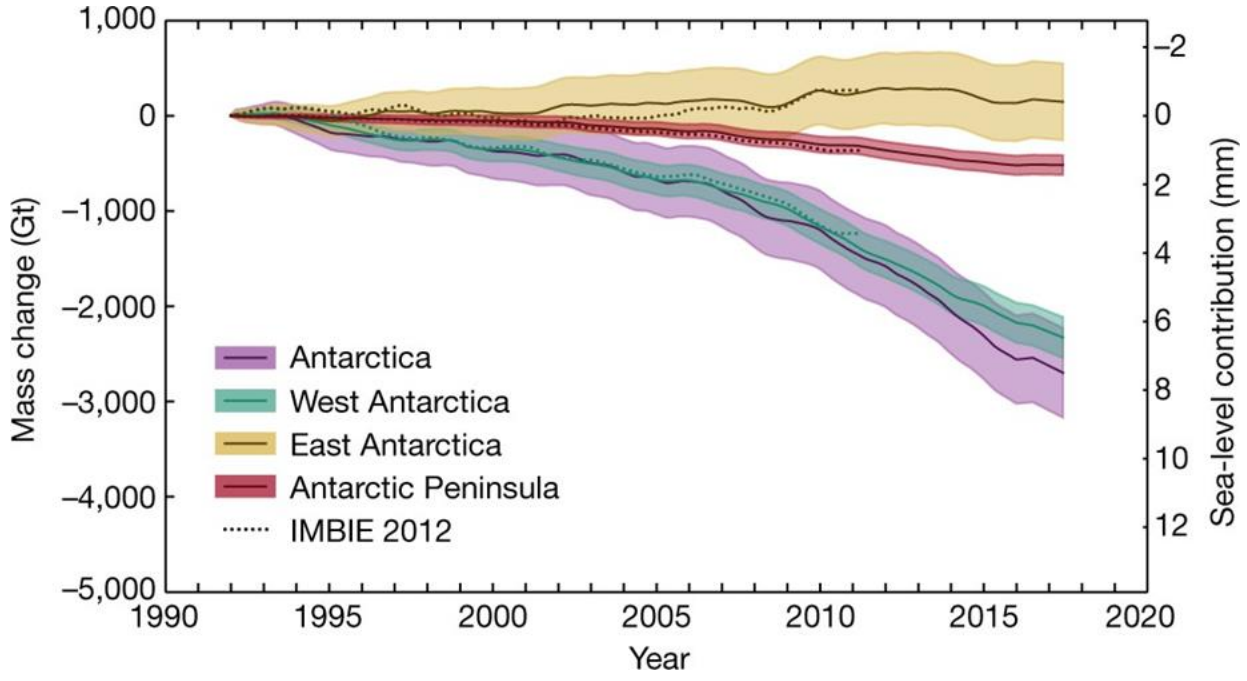

Figure 2.1: Estimated Antarctic Ice Sheet mass change between 1992 and 2017, reconciled from 24 previous studies (from The IMBIE Team, 2018).

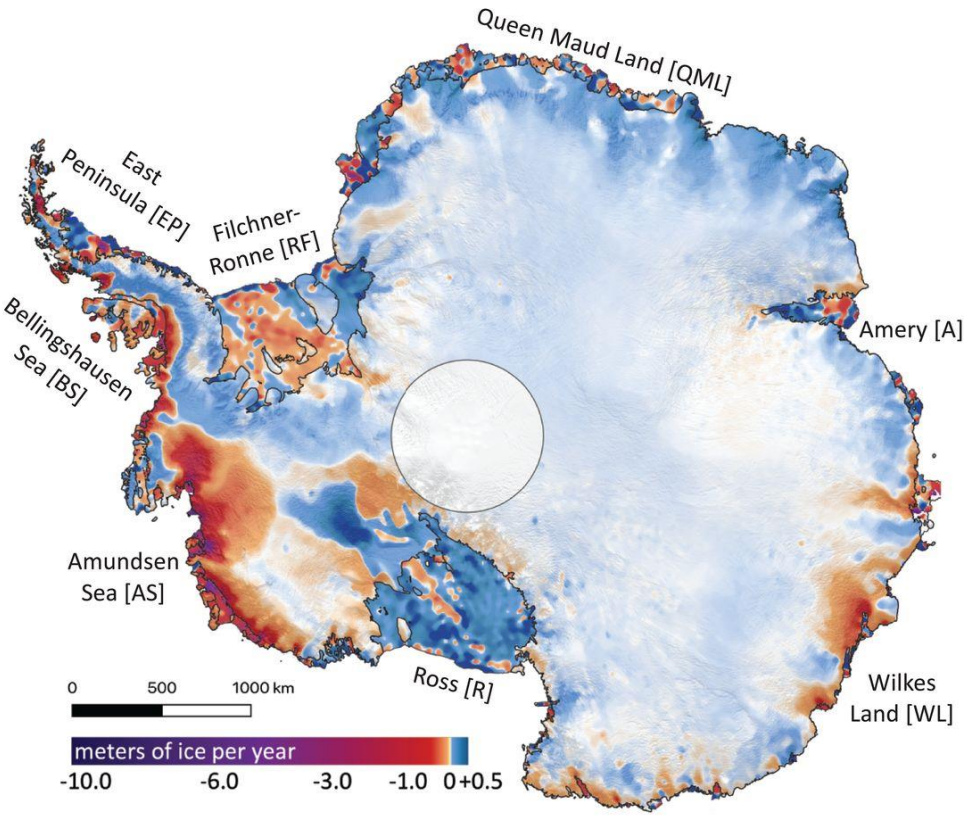

Figure 2.2: Spatial variations in mass loss from the Antarctic Ice Sheet between 2003 and 2019, from Smith et al. (2020).

Whilst independent estimates of ice sheet mass balance are in good agreement for the WAIS and AP (The IMBIE Team, 2018), the mass balance of the EAIS remains uncertain (Fig. 2.3; Noble et al., 2020; Stokes et al., 2022). Past observations have typically suggested either a state of positive mass balance (Davis et al., 2005; Zwally et al., 2005; Boening et al., 2012; King et al., 2012; McMillan et al., 2014; Zwally et al., 2015; Harig and Simons, 2015; Martin-Español et al., 2017; Gardner et al., 2018; Smith et al., 2020; Wang et al., 2021; Zwally et al., 2021) or near-equilibrium (Shepherd et al., 2019) due to enhanced snowfall at the interior. For the 25 years between 1992 and 2019, the IMBIE Team found small mass gains of 5 ± 46 Gt/ yr (The IMBIE Team, 2018). However, discrepancies of almost 100 Gt yr^{-1} exist between the latest mass balance estimates, which range from + 61 ± 73 Gt yr^{-1} for the 2008 – 2015 period (Gardner et al., 2018) to - 51 ± 13 Gt yr^{-1} between 1979 and 2017 (Rignot et al., 2019). Importantly, some assessments indicate that the EAIS could be less stable than previously thought (e.g. Chen et al., 2009; Rignot et al., 2019) and although long term trends are often obscured by large uncertainties, reconciled estimates point to overall mass loss in the past decade (Bamber et al., 2018; The IMBIE Team, 2018). Furthermore, consistent with recent observations of increased inland thinning (Pritchard et

al., 2009; Schröder et al., 2019; Smith et al., 2020), ice flow acceleration (Li et al., 2016; Shen et al., 2018; Miles et al., 2018, 2021) and grounding line retreat (Li et al., 2015; Konrad et al., 2018; Brancato et al., 2020; Pelle et al., 2021) at several major outlet glaciers, as well as instances of sustained terminus retreat (Miles et al., 2013, 2016) and ice shelf and ice tongue collapse (Miles et al., 2017, 2018; Arthur et al., 2021), many mass balance studies identify common regional mass loss trends in some marine-based catchments of the EAIS. In Wilkes Land, these changes have been related to intrusions of warm Circumpolar Deep Water (CDW) on the continental shelf (Greenbaum et al., 2015; Rintoul et al., 2016; Silvano et al., 2017; Roberts et al., 2018; Ribeiro et al., 2021), suggesting that the EAIS, like the WAIS, is responding sensitively to ocean forcing (Pritchard et al., 2012).

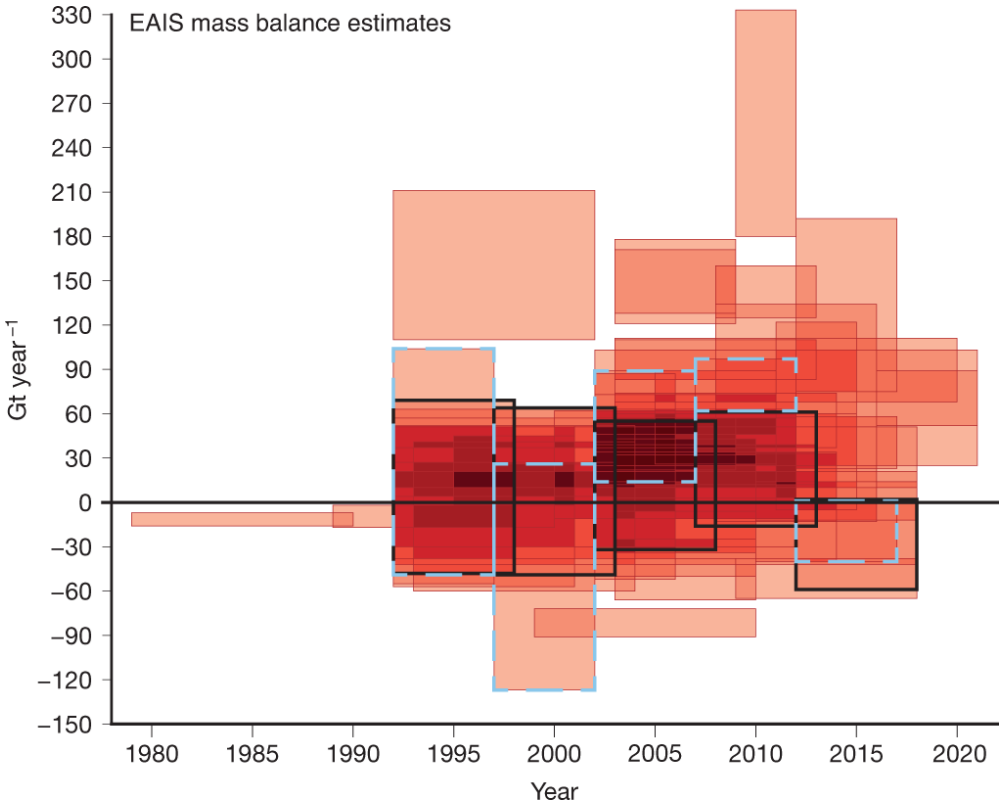

Figure 2.3: Published estimates of EAIS net mass balance, from Stokes et al. (2022). Each estimate is represented by a single box, where overlaps between estimates are shown by regions of dense shading. The boxes outlined in blue and black are the results of the Bamber et al. (2018) and IMBIE (The IMBIE Team, 2018) consensus estimates, respectively.

2.2 The Antarctic Peninsula

2.2.1 External forcing of mass loss from the Antarctic Peninsula

Despite holding a much smaller ice volume than the WAIS and the EAIS, the Antarctic Peninsula Ice Sheet (APIS; 0.28 m SLE (Fretwell et al., 2013)) has contributed significantly to Antarctic mass losses over the past 40 years (Rignot et al., 2019). The negative mass balance of the APIS, estimated as -20 ± 15 Gt/ yr between 1992 and 2017 (The IMBIE Team, 2018), has been associated with rising ocean temperatures (Wouters et al., 2015; Cook et al., 2016) and rapid regional atmospheric warming of ~2^{o}C during the latter half of the 20th century (Scambos et al., 2000; Vaughan et al., 2001; Davies et al., 2012; Mulvaney et al., 2012).

Indeed, numerous studies chart the widespread, climate-driven retreat of the floating tongues of marine terminating outlet glaciers (e.g. Cook et al., 2005, 2016; Pritchard and Vaughan, 2007) as well as the disaggregation of several ice shelves (e.g. Scambos et al., 2000; Cook and Vaughan, 2010; Glasser et al., 2011; Banwell et al., 2013; Etourneau et al., 2019) in the AP since the 1940s. Particular attention has been paid to the dramatic collapse of the Larsen B ice shelf in 2002, which was preceded by gradual basal thinning (Shepherd et al., 2003), record air temperatures, a prolonged melt season (Fahnestock et al., 2002; van den Broeke, 2005), and the extensive ponding and sudden drainage of more than 3000 supraglacial lakes (Scambos et al., 2003; Glasser and Scambos, 2008; Banwell et al., 2013; Leeson et al., 2020). Triggered by a chain reaction of hydrofracture events, the subsequent break up is often cited as an example of ice shelf vulnerability to enhanced surface melting (Banwell and Macayeal, 2015).

2.2.2 Ice shelf buttressing

Overall, rapid warming in the AP led to an 82% reduction in ice shelf area between 1950 and 2008 (Cook and Vaughan, 2010; Bell et al., 2018). Because ice shelves float in hydrostatic equilibrium, the direct sea level contribution of this loss is negligible (Bamber et al., 2018). However, ice shelves exert a critical backstress on adjacent grounded ice, so their significant thinning, retreat and collapse can induce a rapid acceleration of outlet glacier discharge into the ocean (Dupont and Alley, 2005; Pritchard et al., 2012; Gudmundsson, 2013; Fürst et al., 2016; Hughes et al., 2017; Gudmundsson et al., 2019). The speed-up of ice sheet flow in response to such de-buttressing typically leads to the drawdown of inland ice, which can, in turn, result in further grounding line retreat (Dupont and Alley, 2005; Reese et al., 2018) (Fig. 2.4). This process has been the dominant internal driver of recent dynamic

change in the APIS (Royston and Gudmundsson, 2016). For instance, several outlet glaciers formerly restrained by the Larsen B ice shelf have been observed to rapidly accelerate (Rignot et al., 2004; Scambos et al., 2004; Wuite et al., 2015), thin (Hulbe et al., 2008) and loose mass (Rott et al., 2011; Berthier et al., 2012) following its collapse.

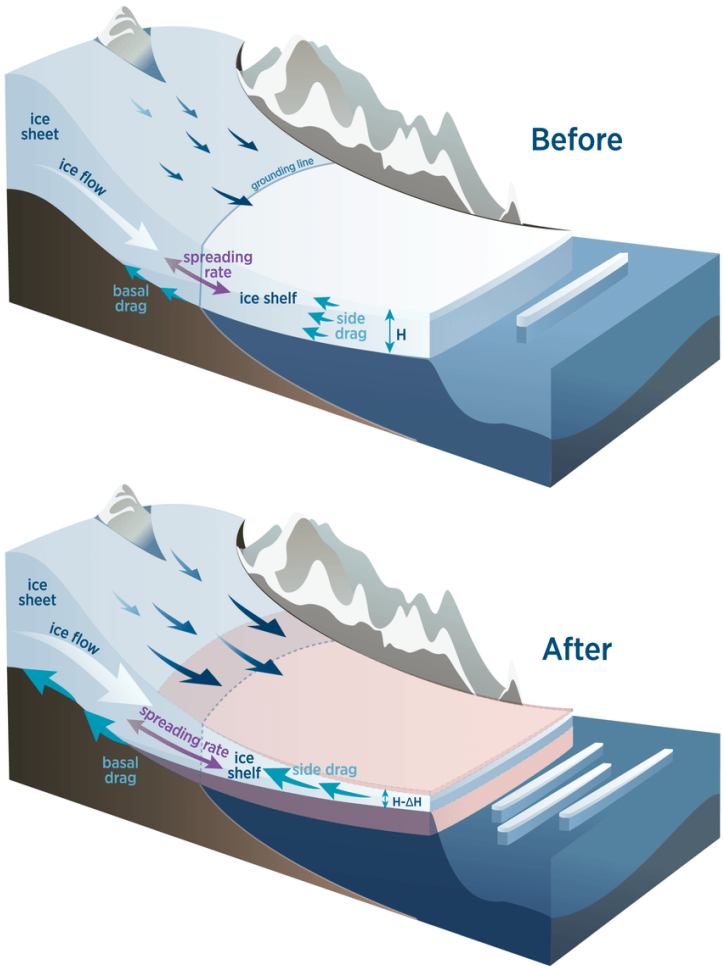

Figure 2.4: Schematic representation of the ice-shelf-sheet system, showing the dynamic ice sheet response to de-buttressing following ice shelf thinning and retreat, from Gudmundsson et al. (2019).

2.3 The West Antarctic Ice Sheet

2.3.1 Past instability of the WAIS

Recent observations of dynamic mass loss from the WAIS have heightened concerns over its vulnerability to future collapse (Oppenheimer et al., 1998; Joughin and Alley, 2011; Noble et al., 2020). The potential instability of the WAIS was initially recognised by Mercer (1978), who suggested that the ice sheet underwent a major retreat during the Last Interglacial

(Marine Isotope Stage 5e, MIS 5e). This theory was supported by (i) sedimentological records of large volumes of meltwater within the Transantarctic Mountains during MIS 5e, where current temperatures permit only limited seasonal melt, and (ii) the notion that recorded MIS 5e GMSL of at least 6 m higher than present would have required a significant contribution from the AIS (Kopp et al., 2009; Dutton et al., 2015). Mercer argued that this collapse was initiated by the loss of buttressing ice shelves.

The possibility of such ice shelf disintegration is further supported by paleoclimate estimates, which suggest global temperatures around 2^{o}C warmer than present during the Last Interglacial, as well as subsurface ocean temperatures of as little as 3^{o}C higher than the Holocene average (Jouzel et al., 2007; Kopp et al., 2009). However, similar conditions have been inferred for earlier Pliocene interglacial periods (Naish et al., 2009; Golledge et al., 2017), and although past retreat of the WAIS has been further evidenced in subsequent work (Scherer et al., 1998; Raymo and Mitrovica, 2012; O'Leary et al., 2013), the timing and rapidity of such mass loss remains uncertain (Joughin and Alley, 2011). Nonetheless, both the paleorecord and numerical simulations are indicative of an unstable ice sheet which, perhaps as recently as 130,000 years ago, has disintegrated under climate scenarios similar to those projected for the near future (Overpeck et al., 2006; Kopp et al., 2009; DeConto and Pollard, 2016; Turney et al., 2020; Wang et al., 2022).

2.3.2 Marine Ice Sheet Instability

The WAIS is marine based, with large areas of ice grounded on inland-sloping bedrock reaching as deep as 2.4 km below sea level (Morlighem et al., 2020). This topographic configuration is thought to render the WAIS inherently vulnerable to even small reductions in ice shelf buttressing, through a mechanism termed 'marine ice sheet instability' (MISI) (Weertman, 1974; Hughes, 1975; Mercer, 1978; Hughes, 1981; Schoof, 2007). When initial thinning causes the grounding line to retreat onto a reverse-bed slope, an increase in the thickness of ice entering flotation means greater ice flux into the ocean. This creates a self-sustained feedback of enhanced inland velocity, thinning and retreat, resulting in a non-linear ice discharge response disproportionate to the initial forcing (Fig. 2.5) (Ritz et al., 2015). MISI has been implicated as a key internal driver of past WAIS retreat (Pollard and DeConto, 2009), and coupled ice sheet-climate models have identified regions susceptible to runaway retreat under projected greenhouse gas emissions (Feldmann and Levermann, 2014; Ritz et al., 2015; DeConto and Pollard, 2016; Nias et al., 2016; Noble et al., 2020). Importantly, some studies suggest that MISI may already be underway in the Amundsen

Sea embayment (ASE; Favier et al., 2014; Joughin et al., 2014; Rignot et al., 2014; Seroussi et al., 2017), which holds more than a metre of potential sea level rise (Mouginot et al., 2014).

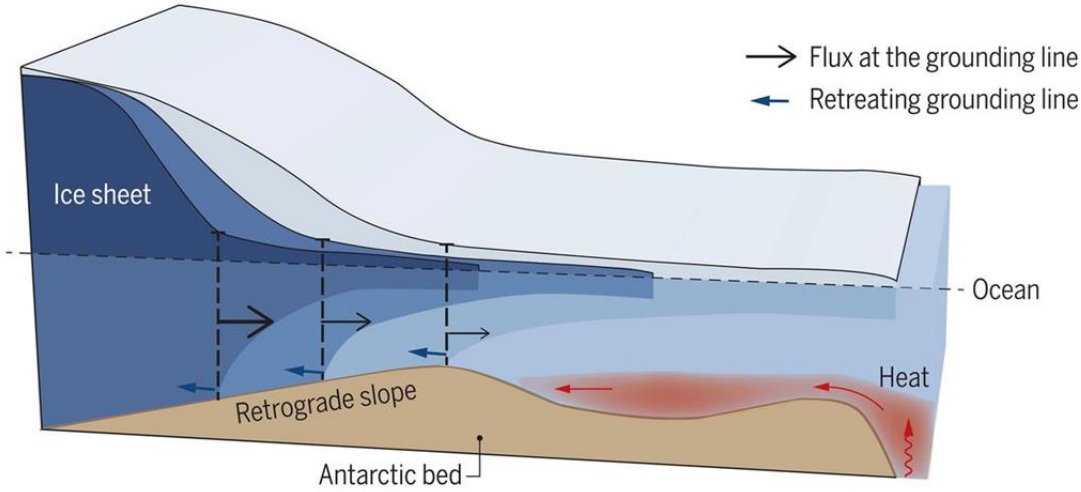

Figure 2.5: Schematic of marine ice sheet instability, from Pattyn and Morlighem (2020).

2.3.2 Ocean forcing of the WAIS

Recent mass loss from the WAIS has largely been attributed to ocean-forced changes in ice shelf configuration (Gagliardini et al., 2010; Pritchard et al., 2012). The majority (~67%) of Antarctic ice shelf mass loss is driven by basal melting (Depoorter et al., 2013; Rignot et al., 2013), which has caused some ice shelves to thin extensively in the past two decades (Pritchard et al., 2012; Jenkins et al., 2018). The highest rates of thinning are concentrated within the Amundsen Sea embayment (Pritchard et al., 2012; Schodlok et al., 2016; Smith et al., 2020; Hogg et al., 2021), where ice flux from the major Thwaites and Pine Island Glaciers has been accelerating since the 1970s (Mouginot et al., 2014; Rignot et al., 2014; Sutterly et al., 2014; Paolo et al., 2015) and constitutes the dominant source of the WAIS imbalance (The IMBIE Team, 2018; Shepherd et al., 2019; Smith et al., 2020). Specifically, enhanced melting of the underside of buttressing ice shelves in the ASE has been associated with intrusions of relatively warm, saline and dense Circumpolar Deep Water (CDW; Shepherd et al., 2004; Jacobs et al., 2011; Pritchard et al., 2012; Rignot et al., 2014; Turner et al., 2017). CDW originates within the Antarctic Circumpolar Current and can breach the continental shelf break when strong westerly winds drive upwelling and mixing within the water column (Thoma et al., 2008). In some places, bathymetric troughs in the sea floor guide deep currents of CDW across the continental shelf and into the sub-ice shelf

cavity. Such intrusions, which can be 4°C above freezing, are known to drive rapid rates of basal melting (Jacobs et al., 2011; Paolo et al., 2015).

The highest basal melt rates (5.9 m yr^{-1}, 2003 – 2008) have been observed at Pine Island Glacier (PIG; Rignot et al., 2014), where rapid grounding line retreat of 31 km between 1992 and 2011 (1.6 km yr^{-1}; Rignot et al., 2014) was accompanied by a 75% increase in ice flow velocity from ~2300 m yr^{-1} in 1974 to ~4000 m yr^{-1} in 2008 (Mouginot et al., 2014). These changes have caused dynamic thinning far inland (Smith et al., 2020) and a ~66% increase in ice discharge from the PIG catchment since the 1980s (Rignot et al., 2019). Because PIG sits on a reverse-bed slope and has exhibited a susceptibility to rapid grounding line retreat, there is that concern that substantial mass loss will continue into the future (Favier et al., 2014; Turner et al., 2017).

2.4 The East Antarctic Ice Sheet

2.4.1 Stability of the EAIS during past warm periods

2.4.1.1 The Miocene

Since the inception of the AIS during the early Ogliocene (33.6 million years ago (Ma); Kennett, 1977; Zachos et al., 1996; Wilson et al., 1998), climate variability has driven major growth and retreat of the EAIS (Gulick et al., 2017; Liebrand et al., 2017). Benthic foraminiferal oxygen isotope ($\delta^{18}O$) records (Shevenell, 2008; Liebrand et al., 2011) and indicators of sea level change (Miller et al., 2005; John et al., 2011) provide indirect evidence of orbitally paced glacial – interglacial cycles throughout the Ogliocene and early to mid-Miocene (24 – 14 Ma; Naish et al., 2001). These fluctuations involved high-magnitude changes in ice mass, whereby the EAIS advanced beyond its present extent (Gasson et al., 2016; Anderson et al., 2019) and left areas of ice-free terrain during periods of decay (Lewis et al., 2008).

The most extensive retreat, directly evidenced by multiproxy sediment records from the Ross Sea, occurred during the mid-Miocene Climatic Optimum (17 -14 Ma; Levy et al., 2016). Numerical models have replicated this mass loss and subsequent sea level rise with ice discharge primarily concentrated within the Aurora, Wilkes and Recovery Subglacial Basins (Gasson et al., 2016). Although these simulations require air temperatures more than 7°C warmer than today (Steinthorsdottir et al., 2021), mid-Miocene global atmospheric CO_2 concentrations of around 500 ppm (Badger et al., 2013) are consistent with those projected

for the coming century (Steinthorsdottir et al., 2021).

2.4.1.2 The Pliocene

Characterised by CO_2 concentrations of 400 ppm and air temperatures 2 – 4ºC higher than present, Pliocene (5.33 – 2.58 Ma) warm periods are thought to be suitable analogues for future climate (Haywood et al., 2013). Records of GMSL at least 10 m above present during the mid-Pliocene implicate substantial mass loss from the EAIS (Rovere et al., 2010; Grant et al. 2019) alongside evidenced retreat of the WAIS (Gohl et al., 2021), and, as such, the EAIS response to Pliocene warming is a topic of particular scientific interest.

Pliocene EAIS stability has been a contentious issue, with early work dominated by conflicting theories based on the origin of marine diatoms within tillites of the Sirius Group in the Transantarctic Mountains (Webb et al., 1984; Harwood et al., 1998; Sugden et al., 1993; Denton et al., 1993). Reported by Webb et al. (1984), the diatoms were initially inferred to have accumulated within marine sediment deposits in the deep subglacial basins of East Antarctica, before being transported to the Transantarctic Mountains during subsequent ice sheet advance. This suggested marine conditions within the continental interior and, by inference, major retreat of the Wilkes (WSB), Aurora (ASB) and Pensacola basins during a Pliocene warm period. However, the discovery of similar high-altitude diatomaceous sediment elsewhere (Stroeven et al., 1998) led to the suggestion that the diatoms had instead been deposited via aeolian processes (Kellog and Kellog, 1996), long emplacement of the Sirius Group units which likely occurred during the Ogliocene or Miocene. The implication was a stable, cold-based EAIS which persisted throughout the Pliocene (Sugden et al., 1993; Denton et al., 1993). This theory was also supported by early ice sheet models, which were unable to force EAIS retreat under estimated Pliocene climate conditions (Pollard and et al., 2005).

Despite this consensus, and the refutation of Webb et al.'s (1984) early hypothesis, more recent work has evidenced partial Pliocene EAIS retreat featuring mass loss from the ASB and WSB (Scherer et al., 2016). Williams et al. (2010) suggest that records of ice-rafted debris on the continental shelf adjacent to Wilkes Land and Adélie Land reflect extensive calving and instability in the ASB during the Pliocene. At the WSB, offshore detrital material has been associated with continental bedrock erosion during ice margin retreat extending several hundred kilometres inland (Cook et al., 2013). In addition, erosional patterns in the Totten Glacier catchment (2 m SLE) indicate that the major outlet has retreated significantly in the past (Aitken et al., 2016), and a fjord landscape within the ASB is suggestive of

multiple large-scale switches in flow regime (Young et al., 2011). Further, updated numerical models which solve for processes of ice shelf buttressing, MISI and marine ice cliff instability have simulated major Pliocene retreat within the marine basins of the EAIS (Fig. 2.6; DeConto and Pollard, 2016). Importantly, modelled mass loss (11.26 m SLE) is consistent with reconstructed sea level, and, in combination with recent geological observations, this supports the idea of a regional dynamic EAIS response to Pliocene warmth.

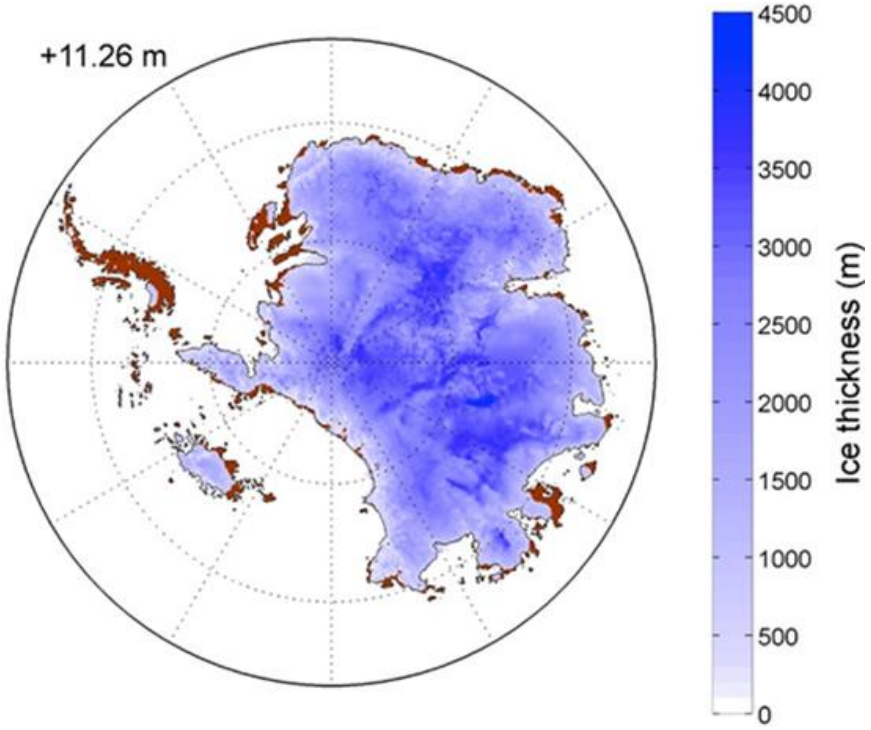

Figure 2.6: Simulated AIS configuration during the mid-Pliocene, from DeConto and Pollard (2016).

2.4.1.3 The Pleistocene

The WSB has also been recognised as a centre of mass loss during interglacial periods of the Pleistocene (2.58–0.017 Ma). Chemical precipitates record the formation of subglacial reservoirs and open seaways within the WSB during MIS 11, which imply that the ice front sat 700 km inland from its present position at a time when air temperatures were only 1 to 2^{o}C warmer than today (Blackburn et al., 2020).

During the Last Interglacial (MIS 5, 130,000 – 115,000 years ago), CO_2 concentrations were around 280 ppm (Lüthi et al., 2008) and surface air temperatures were less than 2^{o}C warmer than present (McKay et al., 2011), yet GMSL was 6 – 9.3 m higher (Kopp et al., 2009; Dutton

et al., 2015). Although this highstand requires mass loss from Antarctica, the magnitude of EAIS retreat is ambiguous (Noble et al., 2020). Sediment, geochemical and ice core records (Bradley et al., 2013; Wilson et al., 2018) evidence retreat within the ASB and WSB, suggested to have been forced by prolonged atmospheric (Wilson et al., 2018) and Southern Ocean warming (Crotti et al., 2022). However, this behaviour is unresolved by numerical models which, without preconditioning for retreat (e.g. DeConto and Pollard, 2016), simulate grounding line stability within the WSB and thus a limited contribution to sea level (0.4 – 0.8 m; Sutter et al., 2020).

2.4.2 Contemporary mass balance of the EAIS

Although there is still uncertainty around the timing and magnitude of EAIS retreat during past warm periods, existing evidence clearly highlights vulnerability to both atmospheric and ocean forcing within the marine basins (Stokes et al., 2022). Indeed, the sensitivity of marine-based sectors compared to terrestrial regions of the ice sheet is reflected in spatially variable patterns of contemporary mass balance (The IMBIE Team, 2018). In Dronning Maud and Enderby Land, enhanced snowfall accumulation (e.g. 200 Gt yr^{-1} in 2009; Shepherd et al., 2012) has led to substantial mass gains (The IMBIE Team, 2018; Rignot et al., 2019). In contrast, Wilkes Land has been losing mass at a rate of 53 ± 47 Gt yr^{-1} (2008 to 2015; Shen et al., 2018), comparable to loss in regions of the WAIS (The IMBIE Team 2018; Shepherd et al., 2019).

2.4.2.1 Wilkes Land

The recent increase in Wilkes Land mass loss is consistent with observations of ice shelf thinning (Fig. 2.7; Pritchard et al., 2012; Rintoul et al., 2016), grounding line retreat (Li et al., 2015; Konrad et al., 2018; Adusumilli et al., 2020; Brancato et al., 2020; Miles et al., 2021), flow acceleration (Li et al., 2016; Greene et al., 2017; Miles et al., 2021) and drawdown (Li et al., 2015; Smith et al., 2020) at some major outlet glaciers. Miles et al. (2016) found consistencies between mean austral summer air temperatures and terminus retreat between 1974 and 2012, and observed dynamic thinning at Totten Glacier (1.9 m yr^{-1}; Pritchard et al., 2009) has been related in part to surface mass losses (Velicogna et al., 2014). However, these trends are attributed more so to Southern Ocean warming (Shen et al., 2018; Gwyther et al., 2018) and fluctuating intrusions of warm modified Circumpolar Deep Water (mCDW) close to ice margin (Greenbaum et al., 2015; Li et al., 2016; Miles et al., 2016; Silvano et al., 2017). Wilkes Land is subject to a ‘warm shelf’ regime (Silvano et

al., 2016), which increases the vulnerability of buttressing ice shelves to ocean forcing (Rintoul et al., 2016).

Totten Glacier, which has the highest ice discharge rate in the EAIS (~70 Gt yr^{-1}; Rignot et al., 2019), has responded dynamically to mCDW observed along the Sabrina Coast (Williams et al., 2010; Silvano et al., 2017, 2019). Rapid basal melting has caused Totten's ice shelf to thin at high rates (10.5 ± 0.7 m yr^{-1}; Rignot et al., 2013; Gwyther et al., 2014; Greenbaum et al., 2015; Rintoul et al., 2016; Silvano et al., 2016; Gwyther et al., 2018), leading to persistent grounding line retreat (176 m yr^{-1}, 1996 – 2013; Li et al., 2015; Konrad et al., 2018) and periods of flow acceleration and inland thinning since the 1970s (Li et al., 2016; Greene et al., 2018). Greene et al. (2018) also recorded seasonal velocity changes in response to fluctuating concentrations of landfast sea ice at the ice front. This demonstrates a mechanical coupling between sea ice and ice shelf stability, as seen elsewhere in Wilkes Land (Miles et al., 2016; Arthur et al., 2021). Although there has been an overall increase in ice discharge from Totten in the past three decades (Rignot et al., 2019), ice flux has remained roughly constant since 2007 (Li et al., 2016; Miles et al., 2022), perhaps due to intrinsic ocean processes regulating cross-shelf heat exchange (Gwyther et al., 2018).

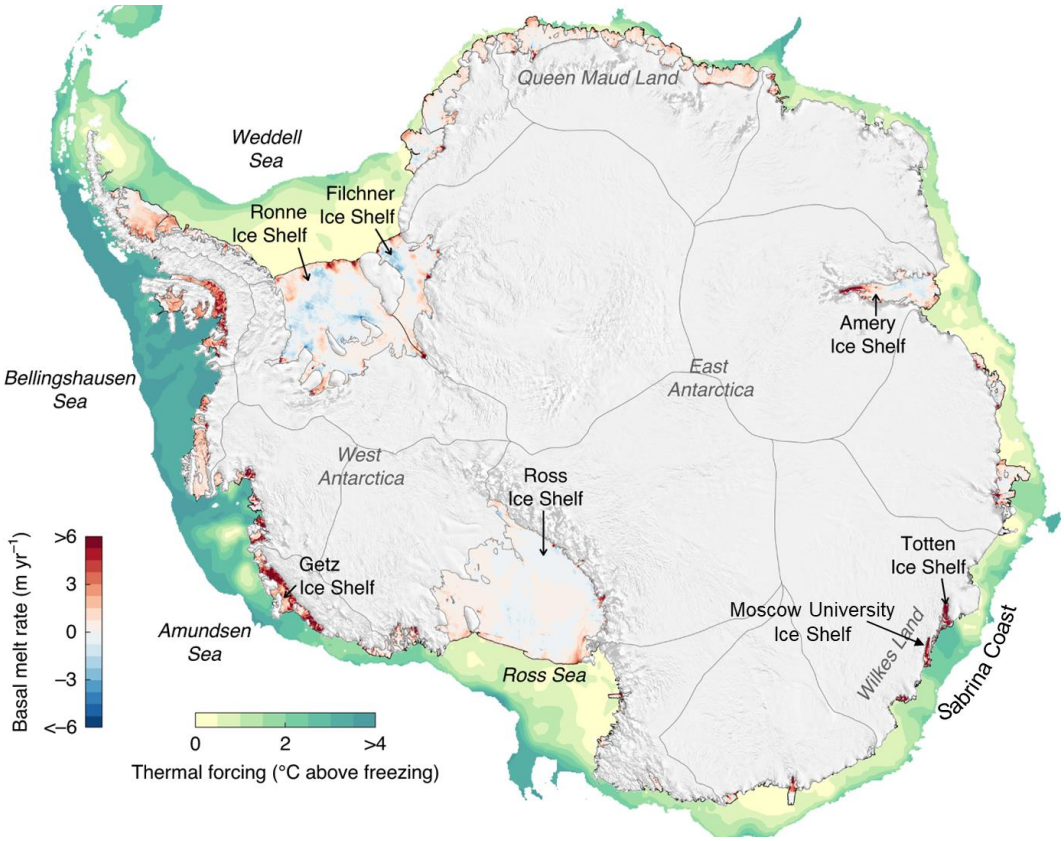

Figure 2.7: Antarctic ice shelf basal melt rates (1994 – 2018) and thermal forcing, from Adusumilli et al. (2020). Note the high melt rates at Totten Ice Shelf and MUIS.

2.4.2.2 Moscow University Ice Shelf and Moscow University Glacier

Located adjacent to Totten, MUIS and MUG have received comparatively little scientific attention. Previous studies have identified strong thinning signals on MUIS during the past two decades (Pritchard et al., 2009; Rignot et al., 2013; Schodlok et al., 2016; Hogg et al., 2021) which suggest enhanced basal melting of 7.4 ± 2.1 m yr^{-1} (1994 – 2018; Adusumilli et al., 2020). Under realistic conditions, simulated area-averaged melt rates reach 10.1 m yr^{-1} (Gwyther et al., 2014). Like Totten, this thinning has been associated with the inflow of warm (0 – 1ºC) mCDW across the continental shelf and into the sub-ice shelf cavity at depths between 400 and 500 m (Khazendar et al., 2013; Gwyther et al., 2014; Silvano et al., 2017, 2019). Heat flux beneath MUIS is thought to be modulated by the Dalton Polynya (Khazendar et al., 2013; Gwyther et al., 2014; Silvano et al., 2017), which, during periods of intense sea ice formation, acts to de-stratify the water column at the ice front, cool the mCDW through mixing, and limit further poleward inflow (Silvano et al., 2017). Whilst the volume and reach of such intrusions is unquantified, Dow et al. (2018) suggest that transverse fracturing at the ice shelf surface reflects the presence of a basal channel extending the length of MUIS, indicative of mCDW routing towards the grounding line.

Despite previously high rates of snowfall in the region drained by the Totten and Moscow University glaciers (van Ommen and Morgan, 2010), recent regional mass balance estimates suggest that discharge from MUG has outpaced catchment gains in recent decades (Velicogna et al., 2014; Mohajerani et al., 2018). Most recently, Rignot et al. (2019) calculated an overall loss of 93 Gt from the Moscow University drainage basin between 1979 and 2017 (-2.5 Gt yr^{-1}). Although MUIS and MUG moderate ice flux from a large inland catchment (1.3 m SLE), and recent observations of mCDW proximal to the ice front suggest a vulnerability to ocean forcing, little is known about their recent dynamic behaviour. It is noted here that a recent study (Li et al., 2022a) featuring observations of ice dynamics at MUIS and MUG, which entered peer review after the data analysis for this thesis had been completed, is discussed in Chapter 5.

2.4.3 Future projections

The EAIS response to projected climate warming represents the greatest uncertainty within predictions of future AIS sea level contributions (The IMBIE Team, 2018; Noble et al., 2020). Recent modelling efforts (Golledge et al., 2015; Edwards et al., 2021; Lowry et al., 2021) have produced a range of projections which involve both significantly positive (e.g. +15 cm;

Golledge et al., 2015) or negative contributions from the EAIS by 2100. Based on the reconciliation of existing models, the latest Ice Sheet Model Intercomparisons Project (ISMIP6) presents the most thorough assessment of AIS mass change under both high and low emission scenarios (Seroussi et al., 2020). For the EAIS, these ensemble estimates range from -6.1 to +8.3 cm of sea level contribution between 2015 and 2100 under the IPCC's high emission scenario, defined by Representative Carbon Pathway 8.5 (RCP8.5) (Payne et al., 2021; Seroussi et al., 2020). Much of these discrepancies arise from differences in the simulated balance between SMB and dynamic mass loss, as well as the pre-conditioned sensitivity of ice shelf basal melt rates to ocean forcing (Edwards et al., 2021; Stokes et al., 2022).

Despite this uncertainty, many models consistently simulate instability within the marine based sectors of the EAIS (Golledge et al., 2015; Ritz et al., 2015; DeConto and Pollard, 2016; Sun et al., 2016; DeConto et al., 2021). Pervasive grounding line retreat and mass loss within the ASB, WSB and Recovery Subglacial Basin (RSB) typically unfolds over multi-century timescales, even without the inclusion of recently surveyed topographic overdeepenings with the potential to enhance MISI (Stokes et al., 2022). Under RCP8.5, Golledge et al. (2015) simulate substantial retreat within the ASB by 2300 (Fig. 2.8). Further, the addition of polar amplification (rapidly warming air temperatures at the high latitudes) prompted ice sheet retreat in the WSB under even the lowest (RCP2.6) emissions scenario (Golledge et al., 2015).

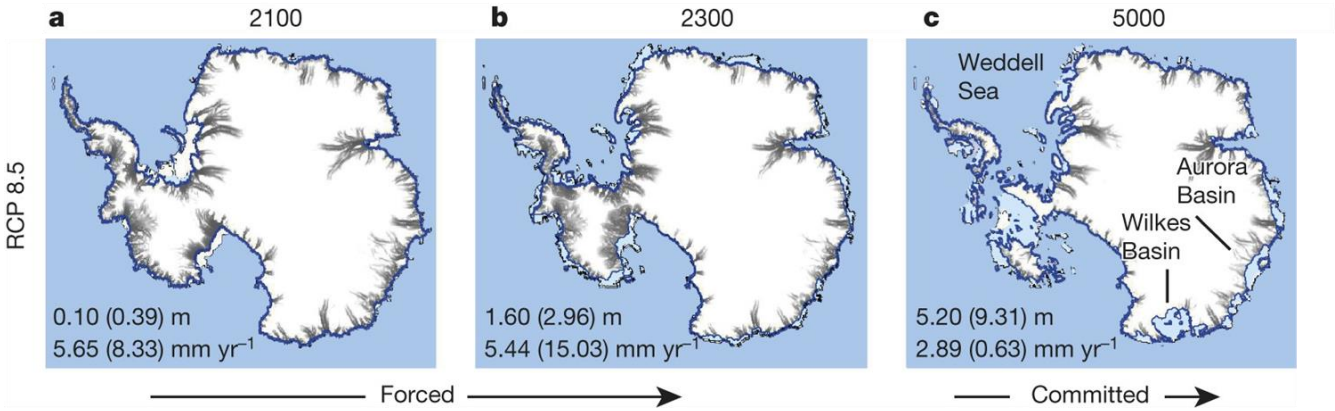

Figure 2.8: AIS evolution under RCP8.5, simulated by Golledge et al. (2015). The magnitude (m) and rate (mm yr^{-1}) of sea level contribution under 'high' (leading value) and 'low' (in parenthesis) emission scenarios are shown for each panel.

With the inclusion of additional feedback mechanisms, subsequent work has simulated

greater mass loss from the EAIS by 2100. DeConto and Pollard (2016) use a model calibrated against Pliocene and Last Interglacial sea level estimates. These highstands are only replicated through incorporating processes of hydrofracturing and marine ice cliff instability (MICI), which is theorised to trigger the collapse of tall ice cliffs at the grounding line and initiate runaway retreat (Pollard et al., 2015). When applied to the same RCP scenarios, this model forces a highly sensitive response to climate warming under medium emissions (RCP4.5) resulting in substantial retreat within the WSB and the Law Dome region (Fig. 2.9). AIS mass loss is observed to accelerate under unabated emissions (RCP8.5), contributing ~15 m of sea level by 2500. Applying an updated version of the earlier model, featuring improved representation of processes of stress propagation within buttressing ice shelves, DeConto et al. (2021) further demonstrate the important role of MISI and MICI in driving widespread EAIS retreat. RCP8.5 conditions result in ice shelf thinning, hydrofracture and collapse, triggering MISI within the ASB, WSB and RSB. The potential effects of ice shelf removal have also been assessed through the Antarctic Buttressing Model Intercomparison Project (ABUMIP) (Sun et al., 2020). Although an unrealistic scenario, with high levels of standard deviation between results, five of the 15 ice sheet models used by Sun et al. (2020) simulate destabilisation and mass loss within the WSB and ASB under a total loss of buttressing.

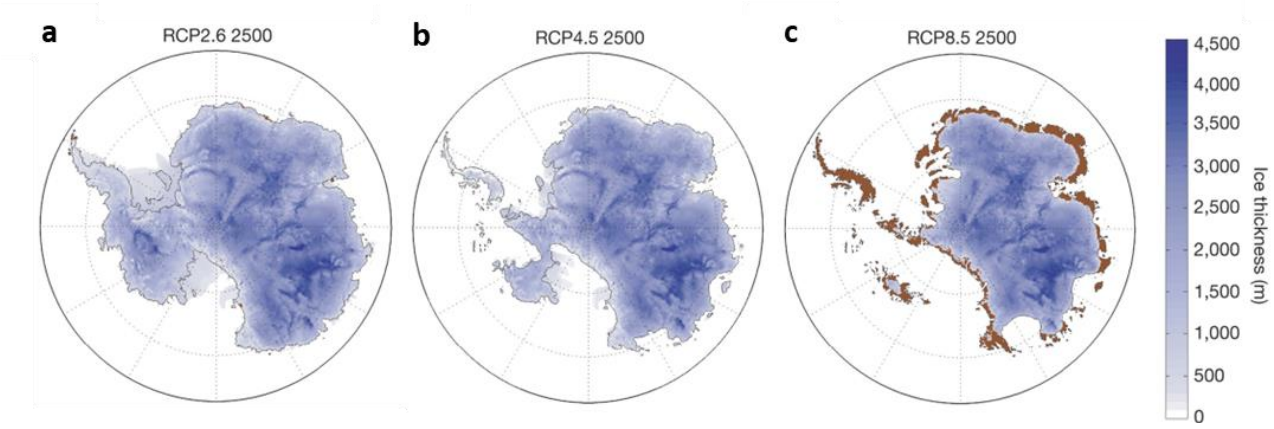

Figure 2.9: AIS evolution under 3ºC warming, simulated by DeConto and Pollard (2016). Note substantial mass loss within the ASB, WSB and RSB of East Antarctica.

Despite remaining uncertainty around the AIS response to both past and future climate warming, paleo-proxy records and numerical simulations clearly point to instability within the marine based sectors of the EAIS (Noble et al., 2020; Stokes et al., 2022). Considering existing predictions, Stokes et al. (2022) suggest that a critical threshold may be averted if

warming is kept to less than 2^{o}C above pre-industrial levels. Further warming, for instance of +3^{o}C, is expected to initiate substantial mass loss from the EAIS (Golledge et al., 2016; McKay et al., 2022), with regional models suggesting that the WSB and ASB are particularly vulnerable to ocean forcing (Mengel and Levermann, 2014; Sun et al., 2016; DeConto et al., 2016, 2021). Indeed, recent observations demonstrate that some major outlets have been responding dynamically to ocean heat flux (e.g. Totten Glacier; Li et al., 2015; Roberts et al., 2018) which is expected to increase in Wilkes Land in the near future as the Southern Ocean warms (Timmermann and Hellmer, 2013; Spence et al., 2014; Herraiz-Borreguero et al., 2022; Jordan et al., in review). Stokes et al. (2022) highlight the importance of assessing contemporary ice dynamics in the EAIS, in order to improve current understanding of sensitivities to observed forcing as well as monitor for the early indicators of dynamic change. Given recent observations of mCDW on the inner continental shelf (Silvano et al., 2017), this is particularly relevant to the ice sheet sector abutting the Sabrina Coast, including Moscow University Ice Shelf and Moscow University Glacier.

2 Data and methods

3.1 Introduction

Advances in satellite remote sensing technologies since the 1970s have seen a step-change in the quantity, coverage and resolution of data available for glaciological research (Pope et al., 2014). Following previous work (e.g. Glasser et al., 2011; Lovell et al., 2016; Chuter et al., 2017; Seehaus et al., 2018; Baumhoer et al., 2018; Miles et al., 2021), this study uses a combination of satellite imagery and pre-existing datasets derived via remote sensing techniques to quantify recent dynamic change at MUG and MUIS. The boxes and flowlines used for data extraction are shown in Fig. 3.1.

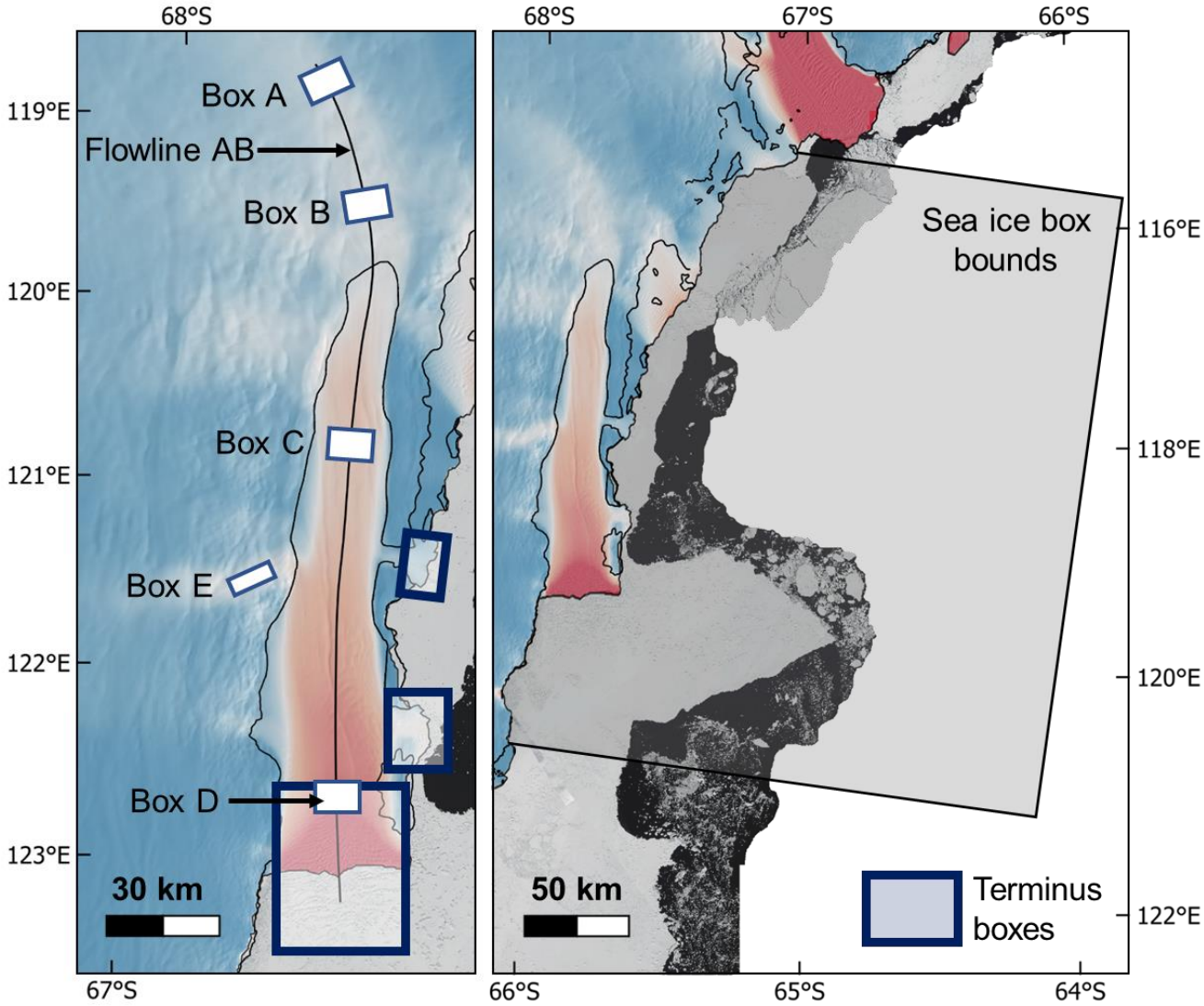

Figure 3.1: Locations of the boxes and flowline used to calculate ice front position change, extract velocity and elevation values and map sea ice distribution. Background images are REMA (grounded ice; Howat et al., 2019) and LIMA (sea ice; Bindschadler et al., 2008), overlaid with ITS_LIVE 2018 grounded ice flow velocity (Nilsson et al., 2021).

3.2 Acquisition and processing of satellite imagery

To facilitate the delineation of ice front positions and sea ice distribution between 1963 and 2022, satellite imagery from the orthorectified Argon (1963; Kim et al., 2007) and RAMP AMM-1 SAR (1997; Jezek et al., 2013) image mosaics of Antarctica, Sentinel-2B (2020), Landsat 1 MSS (1972), Landsat 7 ETM+ (2000 – 2012) and Landsat 8-9 OLI/TIRS (2013 – 2022) were used (Table 3.1, Tables S1 – S5). Landsat 1 Level-1GS imagery was checked for geolocation accuracy against a Landsat 7 scene from 2000 using a number of ground control points placed on ice rises in the area surrounding MUG. Since the Landsat 7-8-9 Level-1GT imagery is radiometrically calibrated and geometrically corrected at point of access, no further pre-processing was required. Imagery from January to February during the austral summer was chosen when available, with additional scenes from November, December and March to create a near-annual time series. A lack of suitably cloud-free imagery for years 1973 – 1996, 2004 and 2005 prevented data collection at these timestamps.

3.3 Terminus position (1963 – 2022)

The MUIS terminus and Outlet East and Outlet West ice fronts were digitised from satellite imagery within GIS at a 1:25,000 scale. Sea ice and calved ice blocks directly adjacent to MUIS meant that the ice front was often difficult to identify. Therefore, to ensure consistency between timestamps, the terminus position was defined as the first clear and continuous path between rumpled glacier ice and detached ice blocks, with movement down-ice (Table 3.2). Changes in ice front position between 1963 and 2022 were calculated using the box method (Moon and Joughin, 2008), which accounts for variable change across the ice front by using the width-averaged change in the area of a reference box placed between the lateral ice margins (Fig. 3.1).

In line with previous studies (Miles et al., 2013, 2016, 2021; Lovell et al., 2017), errors in the digitised terminus position were calculated as ± 1.5 image pixels, accounting for misalignment in the co-registration of satellite imagery (one pixel) and error in manual delineation (0.5 pixels) (Table 3.1). Following the method used by DeBeer and Sharp (2007) to estimate error associated with change in glacier surface area based on manual mapping, the uncertainty associated with terminus change between two timestamps was calculated as the root sum square of the individual error related to each terminus position:

$$\sqrt{(E_1)^2 + (E_2)^2}$$

Where E_1 and E_2 represent the error values associated with two terminus positions.

Table 3.1: Overview of satellite imagery sources used in this study and associated error in digitised terminus position. Level-1GT Tier 2 Landsat imagery is used since Level-1TP or Level-1GT Tier 1 products are not available for the required area.

Source	Period	Pixel resolution (m)	Digitised terminus error (m)
Orthorectified Argon Image Mosaic of Antarctica	October 1963	140	±210
RAMP AMM-1 SAR Image Mosaic of Antarctica	September 1997	200	±300
Landsat 1 Multispectral Scanner (MSS) C2 L1GS	1972	60	±90
Landsat 7 Enhanced Thematic Mapper (ETM+) C2 L1GT	2000 – 2012	30	±45
Landsat 8 Operational Land Imager and Thermal Infrared Sensor (OLI/TIRS) C2 L1GT	2013 – 2022	30	±45
Landsat 9 Operational Land Imager and Thermal Infrared Sensor (OLI/TIRS) C2 L1GT	2022	30	±45
Sentinel-2B	2020	10	±15

3.4 Ice surface velocity (2000 – 2021)

Measurements of average annual ice surface velocity at MUG and MUIS between 2000 and 2021 were extracted from the MEaSUREs ITS_LIVE (Gardner et al., 2018, 2019a) and ESA Antarctic Ice Sheet Climate Change Initiative (AIS CCI) ENVEO (Nagler et al., 2015, 2021; ENVEO, 2022) velocity magnitude datasets. ITS_LIVE surface velocities are obtained using auto-RIFT feature tracking applied to Landsat 4, 5, 7 and 8 optical imagery processed at a spatial resolution of 240 m (Gardner et al., 2018). Annual velocity composites for the years 2000 – 2018 represent the error-weighted average of all image-pair velocity scenes with centre dates from within the same calendar year (Gardner et al., 2019b). To extend the velocity time series beyond 2018, the ENVEO mean monthly velocity magnitude mosaics were used, annually averaged for 2019, 2020 and 2021. Monthly velocity mosaics are composites of all ice velocity fields acquired within a given month. Velocity fields are derived from 6- or 12-day repeat pass Sentinel-1A/B synthetic aperture radar (SAR) data using offset tracking, and are available at a 200 m pixel resolution (Nagler et al., 2015; 2021).

A down-ice velocity profile was created by extracting velocity values at 240 m intervals along Flowline AB in Fig. 3.1. The 228 km flowline is placed at the mid-point between the lateral

shear margins, guided by the main velocity field. To compare velocity changes across the glacier and ice shelf, a time series of average annual velocities was extracted as the mean velocity values from all pixels within each of boxes A – E (Fig. 3.1). Box locations were chosen to maximise data coverage across the time series, although limited pixel counts on MUG prevented data collection from boxes A – C for years 2000 – 2012. Error was assessed using the mean pixel-based annual velocity error value within each box, extracted from the ITS_LIVE error mosaics and the annual average of the ENVEO monthly error datasets (Tables S6 – S10). Since error was spatially variable within each box, and the maximum per-pixel error value was anomalously high in some cases, the mean error was chosen as a more representative metric of uncertainty. Velocity averages based on pixel counts equal to less than 25% of the box area are identified in Tables S6 – S10.

3.5 Ice surface elevation (1993 – 2020)

The Schröder et al. (2019), NASA MEaSUREs ITS_LIVE (Nilsson et al., 2021; 2022) and Smith et al. (2020) ice surface elevation datasets were used to assess surface elevation change (SEC) at MUG. The dataset produced by Schröder et al. (2019) provides monthly measurements of elevation change in grounded ice regions of the Antarctic Ice Sheet between 1978 and 2017. Schröder et al. (2019) cross-calibrate surface height data from the Geosat, ERS-1, ERS-2, Envisat, CryoSat and ICESat laser and radar altimeters to form an integrated dataset of total elevation change (m) relative to surface height during the 2009 – 2010 epoch, at a spatial resolution of 10 km. Nilsson et al. (2022) use the same suite of altimetry datasets, with the addition of ICESat-2 data to extend the ITS_LIVE record to 2020. The ITS_LIVE dataset comprises monthly grids of surface elevation change relative to surface height on Dec 16th 2013, at a resolution of 1920 m.

Monthly surface elevation change values were extracted from both datasets as the mean values within Box A and Box B. SEC was then re-calculated relative to January 1993, the first month from which both datasets had consistent data coverage across MUG. To allow comparisons between the ITS_LIVE and Schröder et al. (2019) results, SEC anomalies were calculated by differencing each monthly SEC value from the mean SEC observed across the 1993 – 2017 epoch within the respective dataset.

The Smith et al. (2020) ice sheet thickness change dataset shows the mean rate of surface elevation change between 2003 and 2019 (m yr^{-1}) at a spatial resolution of 5 km. Surface height measurements are derived from ICESat and ICESat-2 laser altimetry data. This study used the *dhdt* dataset, which is uncorrected for changes in firn air content and therefore

comparable to the rate of SEC calculated from the ITS_LIVE dataset over the same time period. To assess error associated with each rate of SEC value, average uncertainty estimates within Box A and Box B were extracted from the error grid provided with the dataset.

3.6 Grounding line position (1996 – 2020)

To assess grounding line (GL) change at the main trunk of MUG, this study compiles published grounding line positions from the MEaSUREs (Rignot et al., 2011; 2016), AIS CCI (DLR, 2021), Antarctic Surface Accumulation and Ice Discharge (ASAID; Bindschadler and Choi, 2011) and Mosaic of Antarctica (MOA; Scambos et al., 2007) Antarctic grounding line datasets.

The grounding line, which is the point at which grounded ice begins to float, is located within a wider region described as the grounding zone. This zone defines the transition between grounded and floating ice, where short term grounding line migration is driven by ocean tides (Fricker and Padman, 2006). Differential synthetic aperture radar interferometry (DInSAR) techniques or analysis of repeat-track laser altimetry data are used to derive grounding zone features from tidally induced flexure of the ice sheet margin. These dynamic approaches are generally acknowledged as the most accurate methods of grounding zone detection (Brunt et al., 2010). The MEaSUREs 1996 grounding line is derived from DInSAR applied to ERS-1/2 imagery and represents the true grounding line location (Rignot et al., 2011). The AIS CCI October 2017 grounding line position was acquired using a similar method applied to Sentinel-1A/B Level-1 SLC images with a temporal baseline of six days (DLR, 2021).

Alternatively, static methods use the most seaward break in slope on the ice surface as a proxy for grounding line location. In areas of slow-moving ice, an inflection point commonly occurs close to the true grounding line as a result of the sudden change in basal stress where ice detaches from its bed (Fricker et al., 2009). Using this approach, the ASAID and MOA grounding line locations were manually delineated from optical satellite imagery. The ASAID grounding line position was derived from imagery acquired between 1999 and 2003 (Bindschadler et al., 2011), and the MOA grounding line represents three different observations dated to 2004, 2009 and 2014 (Scambos et al., 2007).

Due to the complex geometry of the MUG grounding line, and to account for variable rates of change across the grounding line width, the box method (Moon and Joughin, 2008) was used to measure grounding line migration relative to the MEaSUREs 1996 position. Errors in grounding line change were calculated as the root sum square of the error associated

with the respective grounding line positions.

3.7 Ice surface topography and bed elevation

Profiles of ice surface topography and bed elevation along Flowline AB (Fig. 3.1) were extracted from BedMachine Version 2 (Morlighem et al., 2020). Values were taken at 500 m intervals, corresponding to the spatial resolution of the dataset. In the study region, BedMachine V2 data is derived from mass conservation in grounded ice areas, where the error in estimated bed elevation has a mean of 64 m and ranges between 10 and 142 m. Over floating ice, data is derived from interpolation. Here, error ranges between 64 and 171 m, and has a mean of 71 m.

3.8 Sea ice distribution (1963 – 2022)

Because glacier dynamics in Wilkes Land have previously been correlated with the production (Miles et al., 2016) and presence (Miles et al., 2017) of sea ice, including at Totten Glacier (Khazendar et al., 2013; Gwyther et al., 2014; Greene et al., 2018; Van Achter et al., 2022), sea ice distribution adjacent to MUIS over the 1963 – 2022 period was analysed. Sea ice was mapped within a 76,400 km^2 bounding box (Fig. 3.1) at 27 timestamps, using mosaics of satellite imagery obtained within the same month and separated on average by a maximum of 14 days (Table S5). Following Holt et al. (2013) and Arthur et al. (2021), features were classed as one of six categories, identified according to the criteria defined in Table 3.2. These include: landfast sea ice; fractured sea ice; open or dense sea ice mélange; discrete sea ice pieces; and calved ice blocks. Variations in the extent of available imagery and cloud cover prevented mapping of a consistent region at every timestamp. The maps therefore provide a qualitative assessment of sea ice coverage, rather than a complete classification across the entire box area.

At the Dalton Iceberg Tongue (DIT), full image coverage at all timestamps allowed mapping and quantification of changes in the iceberg tongue extent throughout the observational period. In order to assess spatial variability, a frequency density map was created by summing the occurrence of the DIT at each timestamp within a grid of 30 m^2 cells.

Table 3.2: Sea ice classes and criteria for identification in satellite imagery, adapted from Arthur et al. (2021) and Holt et al. (2013).

Feature	Example	Description for identification in satellite imagery	Significance
Terminus		Transition from the calving ice front to landfast sea ice or sea ice mélange. Change from a rumpled surface to a flat surface with rafted ice blocks.	Defines the ice shelf extent. Changes in terminus position relate to ice dynamics (Benn et al., 2007).
Landfast sea ice		Sea ice directly adjacent and attached to the ice shelf front or coastline (Fraser et al., 2020).	Can exert a buttressing force on adjacent ice fronts (Massom et al., 2010). Production impacts ocean stratification and ice-ocean interactions (Gwyther et al., 2014).
Calved ice (Iceberg)		Blocks of ice detached from the ice shelf front or terminus and held within sea ice or open ocean.	Indicative of recent calving from the ice front.
Sea ice piece		Large flat area of sea ice detached from main sea ice area.	Records the presence and disaggregation of sea ice.
Open mélange	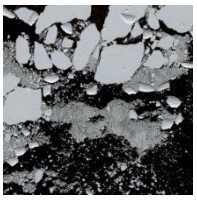	Area of disaggregated sea ice, marine ice, firn, icebergs and open ocean.	Records the presence of unconsolidated mélange, which has no buttressing effect on the ice front (Moon et al., 2015).
Dense sea ice mélange	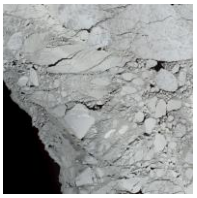	A combination of sea ice, marine ice, firn and icebergs (Moon et al., 2015; Arthur et al., 2021).	Can have a stabilising effect on adjacent ice fronts (Massom et al., 2010; Arthur et al., 2021).
Fractured sea ice		Area of fractured/ broken sea ice.	Records sea ice production.

4 Results

4.1 Terminus change

The MUIS terminus retreated by 3.9 ± 0.215 km overall between October 1963 and January 2021 (Figs. 4.1a, 4.1b). Ice loss from the landward side of the ice front between 1963 and 1972 caused an initial retreat and change in terminus configuration. Since 1997, an increase in the frequency of observations reveals a cyclical pattern of advance and retreat. This signal is characterised by a sustained period of gradual advance over three to five years, followed by the detachment of multiple ice blocks between 1 and 7 km^2 from across the terminus within one summer season. Calved blocks are held within multi-year landfast sea ice abutting the ice front. Oscillations in terminus position occur within a ~6.5 km range, where the maximum retreat position aligns with a topographic rise on the seaward ice margin (Fig. 4.2). Notably, there is no evidence of significant or sustained retreat since the late 1990s.

Outlet East retreated by ~2.6 ± 0.215 km between 1963 and 2000, whereas Outlet West advanced during this period (Fig. 4.1c, 4.1d, 4.1e). Since then, both outlets display a similar pattern of change in ice front position, and, whilst the amplitude of change is greater at Outlet East, both undergo a very slight overall advance relative to their 2000 positions (Fig. 4.3).

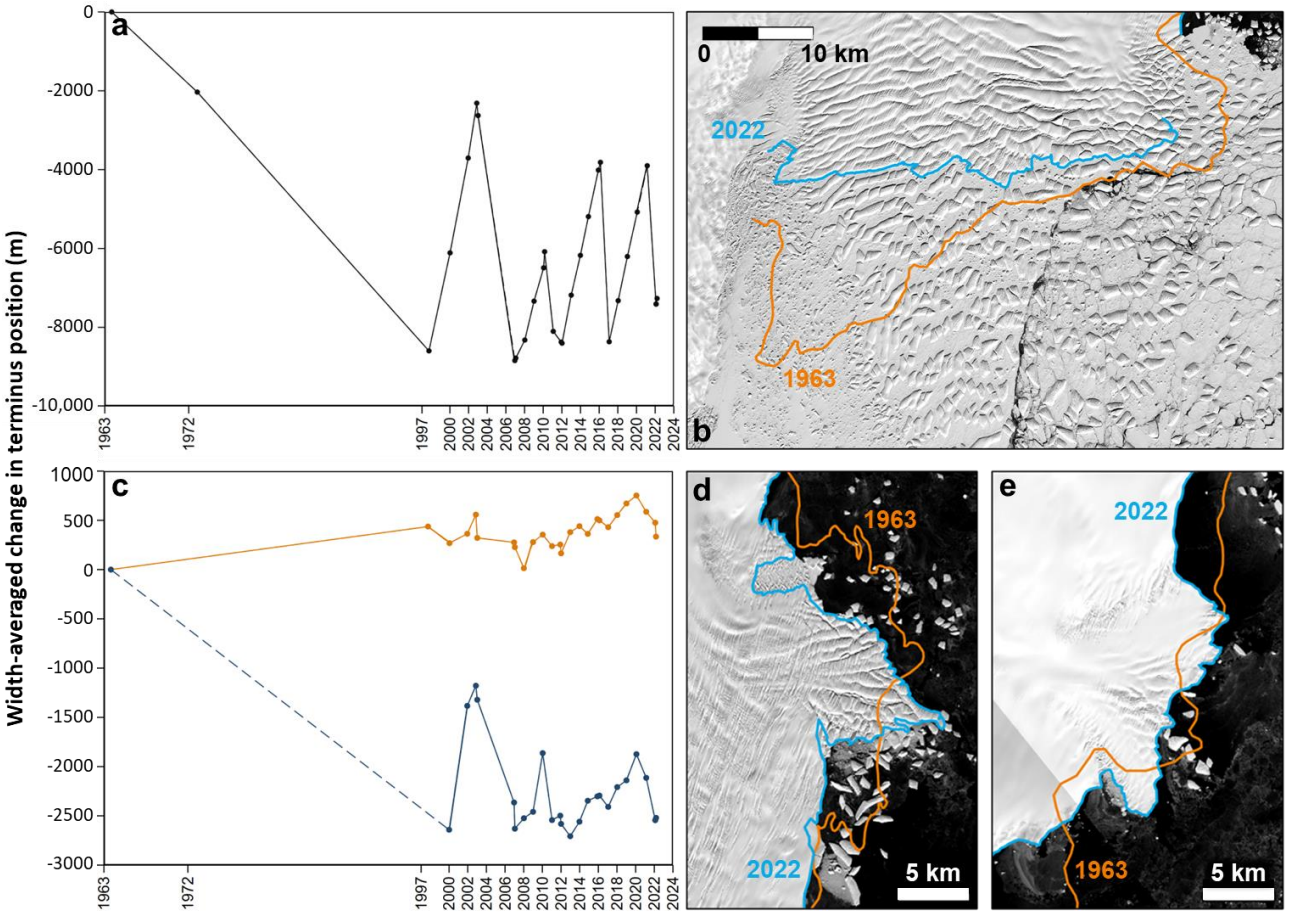

Figure 4.1: (a) Width-averaged change in terminus position at the MUIS ice front, 1963 – 2022. Dashed lines in both 1a and 1b show periods where the gap between observations is greater than five years. (b) MUIS terminus positions in October 1963 and March 2022. Image date: 12/03/22. (c) Width-averaged change in ice front position at Outlet West and Outlet East, 1963 – 2022. (d) Outlet East ice front positions, Oct. 1963 and March 2022. Image date: 12/03/22. (e) Outlet West ice front position, Oct. 1963 and March 2022. Image date: 09/03/22.

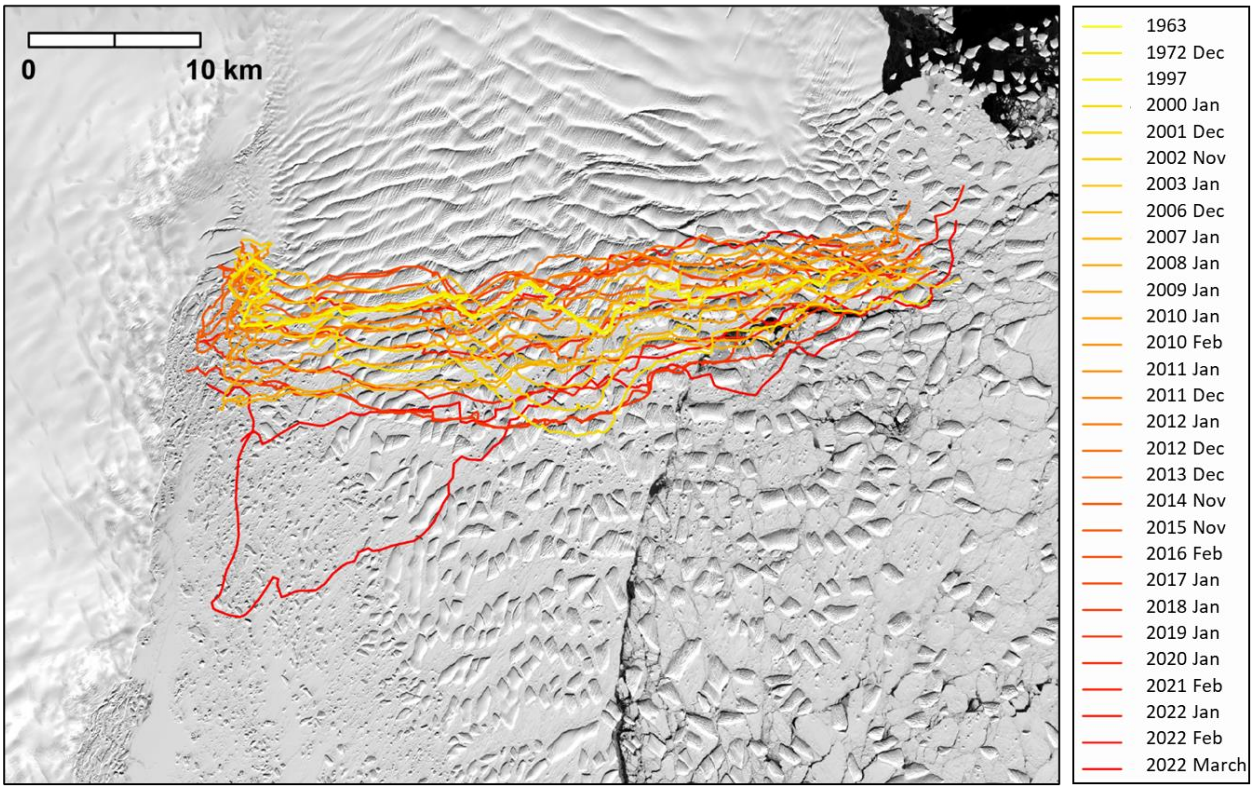

Figure 4.2: MUIS terminus positions at all timestamps between October 1963 and March 2022. Landsat image date: 12/03/22.

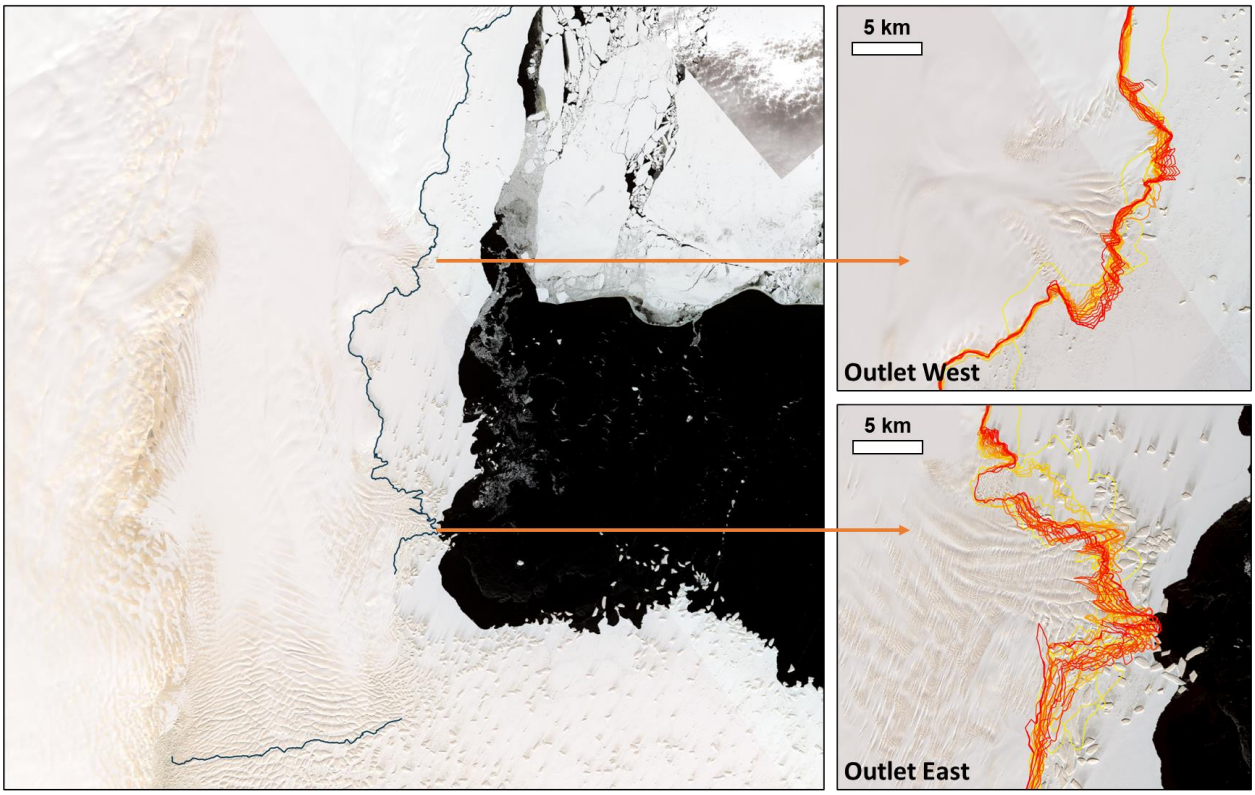

Figure 4.3: Locations of Outlet West and Outlet East and ice front positions at all timestamps 1963 – 2022. Landsat image dates: 01/11/2014 and 15/11/2014.

4.2 Ice surface velocity

Figure 4.4a shows the ice surface velocity of MUG and MUIS in 2018. Ice flow first exceeds 50 m yr^{-1} around 220 km from the MEaSUREs 1996 grounding line position within the Aurora Subglacial Basin. The main tributary of MUG carries ice towards the MUIS grounding line at ~350 m yr^{-1}, where flow is channeled through a topographically confined ice shelf. Ice surface velocity extracted along Flowline AB shows a down-ice acceleration following the transition from grounded to floating ice, in line with an increase in bed elevation (Figs. 4.4b and 4.4d). Ice speed remains stable until halfway down the length of MUIS (130 km along Flowline AB), where a tributary initiating 120 km from the coast merges with the main trunk of flow at a speed of ~400 m yr^{-1}. A further acceleration occurs where the bed width increases and MUIS becomes unconstrained by topography on its seaward margin (Figs. 4.4b and 4.4c).

No significant (i.e., outside of the error margin) overall change in ice surface velocity between 2000 and 2021 was observed (Fig. 4.5, see Table S6 – S10 for error values). A lack of complete spatial data coverage across the ITS_LIVE mosaics prevented data collection within Boxes A – C between 2000 and 2010. However, comparison between all boxes shows a near-uniform pattern of minimal changes across the study site, suggesting that ice surface velocity on MUG remained stable during this period. It is noted that the mean velocity magnitude value extracted from Box D for the 2000 timestamp has high associated uncertainty of ± 250 m yr^{-1}. However, velocity extracted within Box E shows a comparable pattern of change and has a lower error margin of ± 23 m yr^{-1} for the 2000 value, indicating that the low magnitude of change observed between 2000 and 2010 is reliable. Ice speed decreased by 85.6 ± 124 m yr^{-1} or 20% close to the grounding line between 2010 and 2014, followed by a 7% acceleration between 2014 and 2006; a 7% deceleration between 2016 and 2017; and a 6% acceleration between 2016 and 2020. Changes in up-ice velocity extracted from Box A align closely with changes near to the grounding line, but up-ice speed is 19% slower on average. Ice flow velocity on MUIS increased by 25% from 399 ± 29 m yr^{-1} to 500 ± 8 m yr^{-1} between 2013 and 2014, followed by a further 6% increase between 2014 and 2017. A 4% deceleration was observed between 2017 and 2019, after which MUIS velocity followed observed changes at the grounding line. Following a synchronous acceleration between 2000 and 2002, ice flow velocity extracted within Box D and Box E show opposing patterns of change, whereby an increase in flow speed at the terminus correlates with a decrease on the tributary. In summary, the results reveal a pattern of minor changes in ice surface velocity averaging at ± 4% and not exceeding ± 25% per year, leading

to no significant overall decrease or increase in flow speed throughout the observational period.

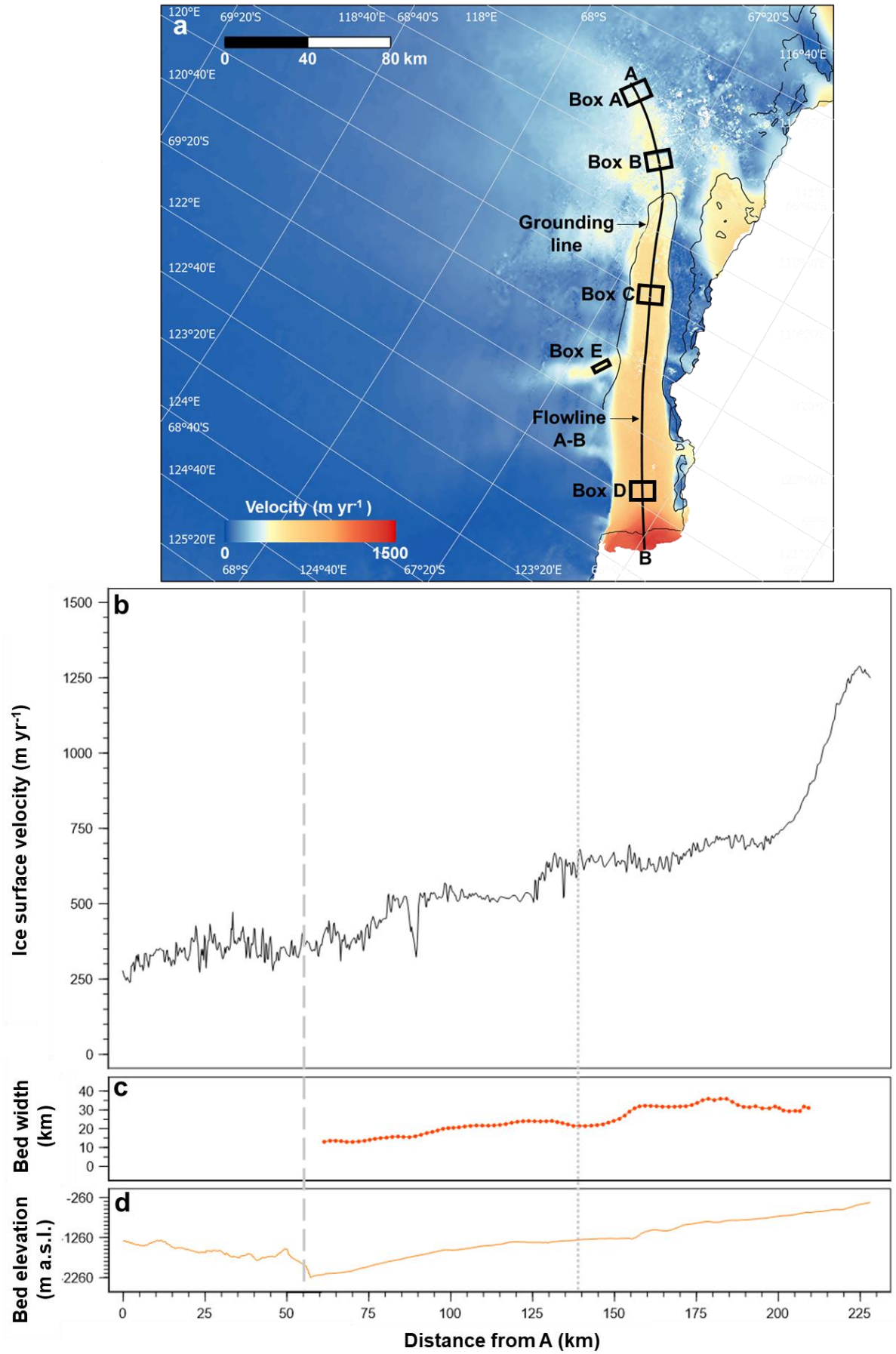

Figure 4.4: (a) Placement of Flowline AB and Boxes A – E, displayed over the 2018 ITS_LIVE velocity magnitude. (b) Mean annual ice surface velocity between 2000 and 2021 extracted along Flowline AB, as shown in Fig. 4.2d. The dashed grey line marks the MEaSUREs 1996 grounding line position. (c) Bed width extracted from BedMachine V2 at 1.75 km intervals along the length of MUIS. (d) Bed elevation along Flowline AB extracted from BedMachine V2.

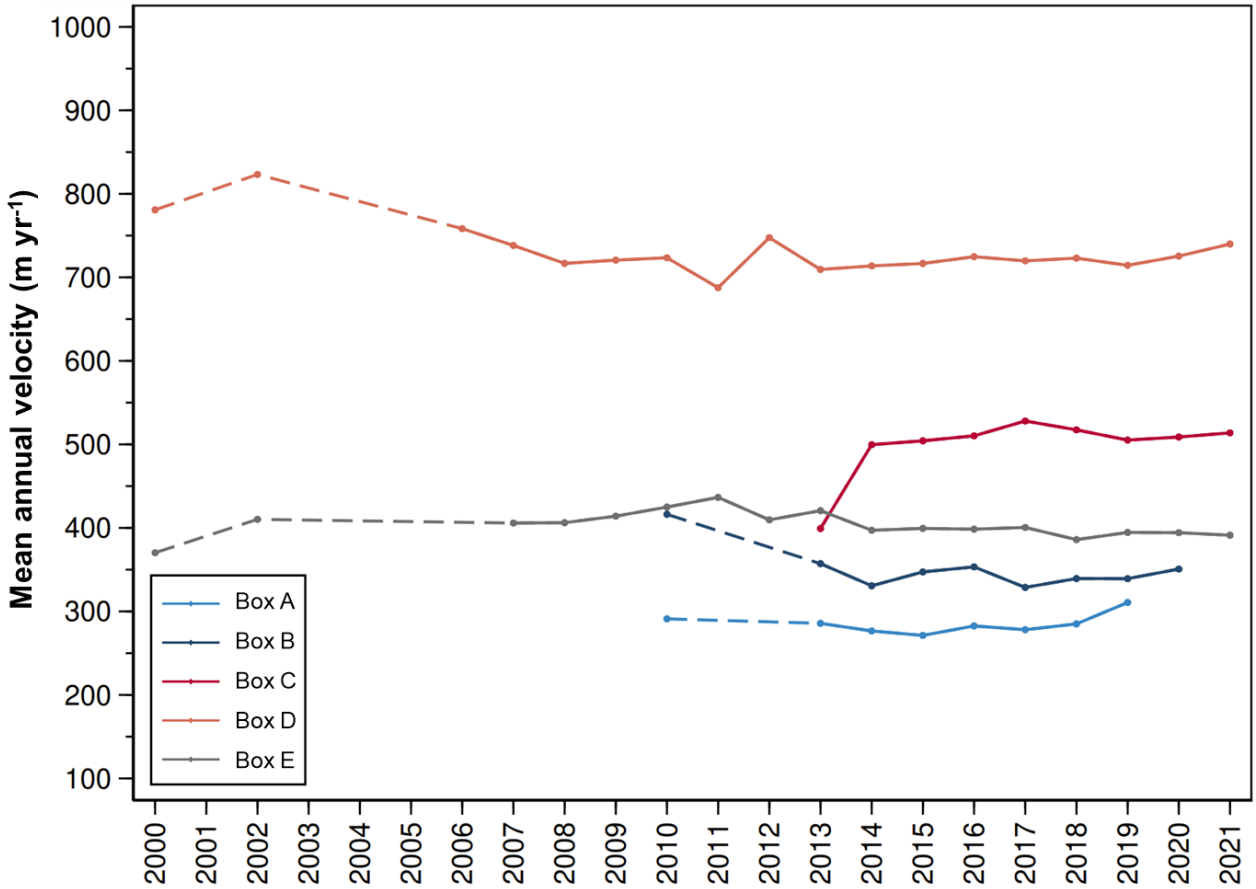

Figure 4.5: Annual ice surface velocity magnitude 2000 – 2021, extracted as the average within Boxes A - E from the ITS_LIVE (2000 – 2018) and ENVEO (2019 – 2021) datasets. Velocity error values are displayed in Tables S6 – S10. Dashed lines show periods where the gap between observations is greater than one year.

4.3 Ice surface elevation change

Figure 4.6a shows the spatial pattern of overall surface elevation change (SEC) between 2003 and 2019 on grounded ice regions around MUG, visualised from the Smith et al. (2020) dataset. Surface lowering appears to occur at the highest rates within areas of faster ice flow, such that total elevation change is greatest close to Box B on the MUIS grounding line

(-0.57 ± 0.01 m yr^{-1} from 2003 to 2009). Following the main trunk of flow upstream, the rate of surface lowering decreases to -0.30 ± 0.008 m yr^{-1} (Table 4.1). In the areas of slow-moving ice surrounding MUG, SEC varies from -0.18 to +0.05 m yr^{-1} but averages at -0.10 ± 0.009 m yr^{-1}. Increased surface lowering is also found close to the grounding line of the tributary marked in Fig. 6a, where the rate of change is -0.22 ± 0.009 m yr^{-1}. These observations of comparatively little decrease in elevation where surface velocity is slower suggest that glacier thinning is a response to changes in ice dynamics, rather than local surface mass balance.

Ice surface elevation change anomalies (i.e., deviations from the long-term monthly average) calculated within Box A and Box B show an overall thinning signal on MUG between 1993 and 2020 (Fig. 4.6). This study found a general agreement between average SEC extracted from the ITS_LIVE and Schröder et al. (2019) datasets within Box B. The following values are derived from the ITS_LIVE results, which have considerably less associated error compared to the Schröder et al. results (the average extracted error is ± 0.84 m yr^{-1} and ± 2.23 m yr^{-1} for the ITS_LIVE and Schröder et al. data, respectively). Close to the grounding line, surface elevation change oscillated within a 1.6 m margin between 1993 and 2003, after which it remained stable until 2010. Since then, the mean annual rate of SEC increased significantly to -0.86 ± 0.16 m yr^{-1} during the 2011 to 2016 period in line with a pattern of consistent thinning, accounting for 4.3 ± 0.79 m or 79% of overall thinning observed throughout the timeseries. SEC was observed to slow by 89% between the 2010 – 2015 and 2015 – 2020 epochs, with a further 0.46 ± 0.74 m of elevation lowering between 2015 and 2020. In summary, the surface elevation of MUG exhibited some variability between 1993 and 2010, and an overall thinning trend thereafter.

By comparison, less total surface elevation change was observed within the upstream region of Box A between 1993 and 2020. However, SEC values extracted from Box A also exhibit greater disagreement between the ITS_LIVE and Schröder datasets, whereby the ITS_LIVE results suggest less overall surface lowering but a higher amplitude of change during this period. MUG was observed to thin at a mean annual rate of -0.57 ± 0.17 m yr^{-1} from 2010 to 2015, before switching to a period of negligible (+0.46 ± 0.74 m yr^{-1}) overall elevation change between 2015 and 2020.

Table 4.1: Mean annual rate of surface elevation change, 2003 – 2019 extracted from the Smith et al. (2020) and ITS_LIVE datasets. It is noted that the higher rate of SEC found

within Box A than Box B using the ITS_LIVE dataset is skewed by the anomalously high elevation increase observed between 2002 and 2003.

	Box A mean rate of SEC (m yr^{-1}) 2003 – 2019	Box B mean rate of SEC (m yr^{-1}) 2003 – 2019
Smith et al. (2020)	-0.30 ± 0.008	-0.41 ± 0.045
ITS_LIVE	-0.36 ± 0.049	-0.29 ± 0.044

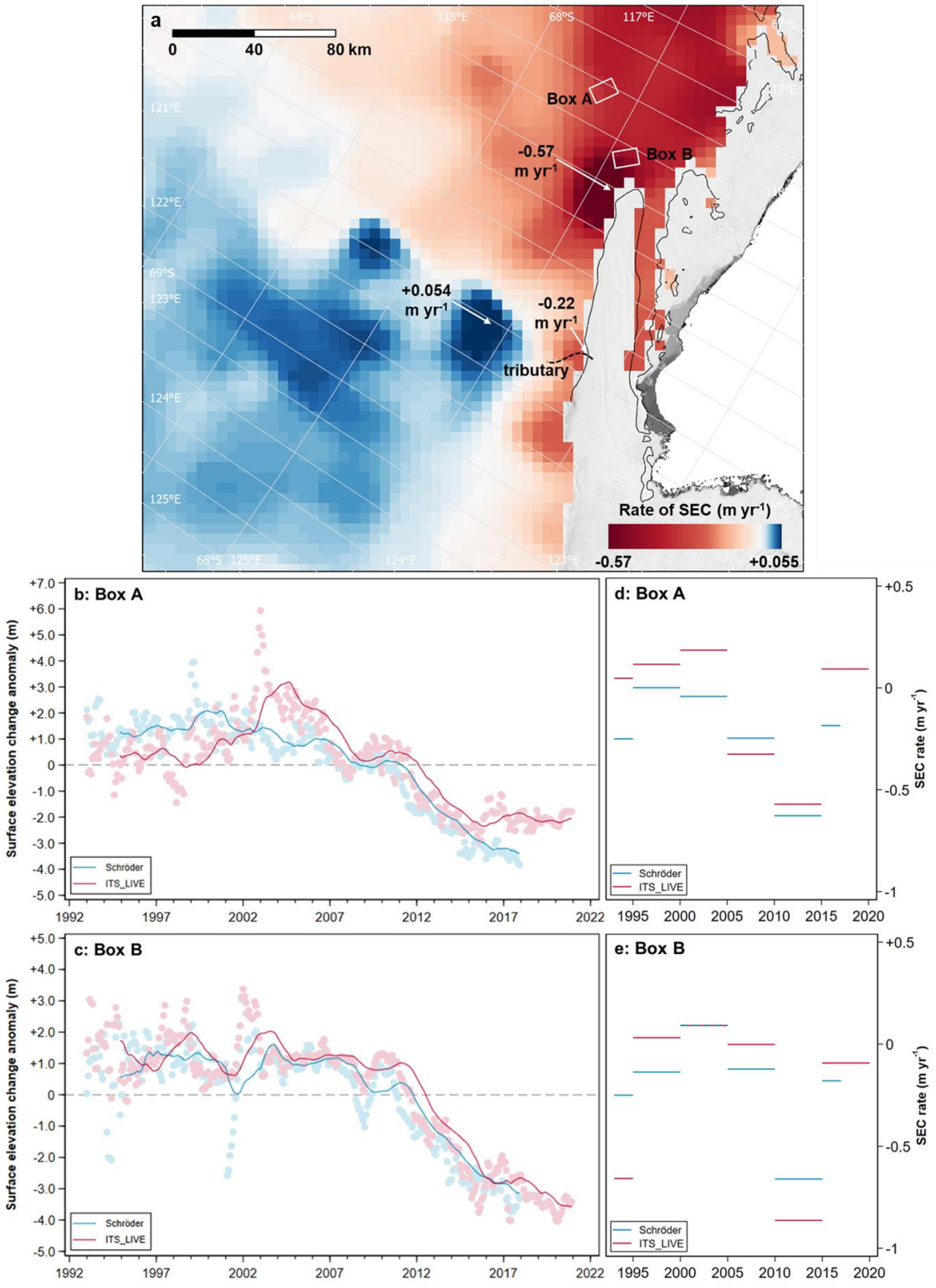

Figure 4.6: (a) Mean rate of annual surface elevation change between 2003 and 2019 across grounded ice regions near to MUG, visualized from the Smith et al. (2020) *dhdt* dataset at a 5 km^2 resolution. Background image is the MODIS mosaic of Antarctica (Haran et al., 2018). (b, c) Scattered points are monthly ice surface elevation change anomalies averaged within Box A and Box B, extracted from the ITS_LIVE and Schröder et al. (2019) SEC datasets. Overlaid lines show the 24-month running mean for each timeseries. (d, e) Rate of surface elevation change averaged within Box A and Box B for both datasets.

4.4 Grounding line change at MUG

The MUG grounding line at its most recent measured position (October 2017) features two main curves extending inland across the core ~20 km wide trunk of fast flow (Fig. 4.7a). Comparison between the 1996 and 2017 positions suggests overall width-averaged grounding line retreat of 1.4 ± 0.1 km during the 21-year period (Fig. 4.7b). This rate of retreat (~67 m yr^{-1}) is relatively small compared to GL migration observed at the neighbouring Totten Glacier (Li et al., 2015) and across Wilkes Land more generally (Konrad et al., 2018). The extent of retreat is varied across the GL; the eastern and western lobes retreated by 1.8 km and 2.4 km respectively, but the GL remained static within the central region.

The ASAID and MOA datasets suggest a more complex pattern of grounding line migration. This involves retreat of 5.65 ± 0.36 km between 1996 and 2003 and a further 0.77 ± 0.40 km between 2003 and 2014, followed by a 5.02 ± 0.25 km re-advance between 2014 and 2017. However, it is noted that grounding line positions located using a similar method are generally in good agreement, such that the positions delineated manually based on the identification of a break in slope on the ice surface (MOA and ASAID) are significantly different to those extracted using DInSAR (MEaSUREs and AIS CII, see Fig. 4.8 and Table 4.2). By inspecting annual satellite imagery and bed elevation, it was found that the break in slope observed beneath the MOA and ASAID GLs, which remained static between 1963 and 2022, coincides with a step in bed topography (Fig. 4.8). Ice surface velocity was also observed to undergo limited change across the MOA and ASAID GLs but increase in line with the AIS CCI GL. It is therefore tentatively proposed that the break in slope used to define the MOA and ASAID GL positions actually reflects a topographic step in bed elevation, rather than a transition from grounded to floating ice. Therefore, a conservative estimate of limited grounding line retreat (-1.4 km) at MUG between 1996 and 2017 is

suggested.

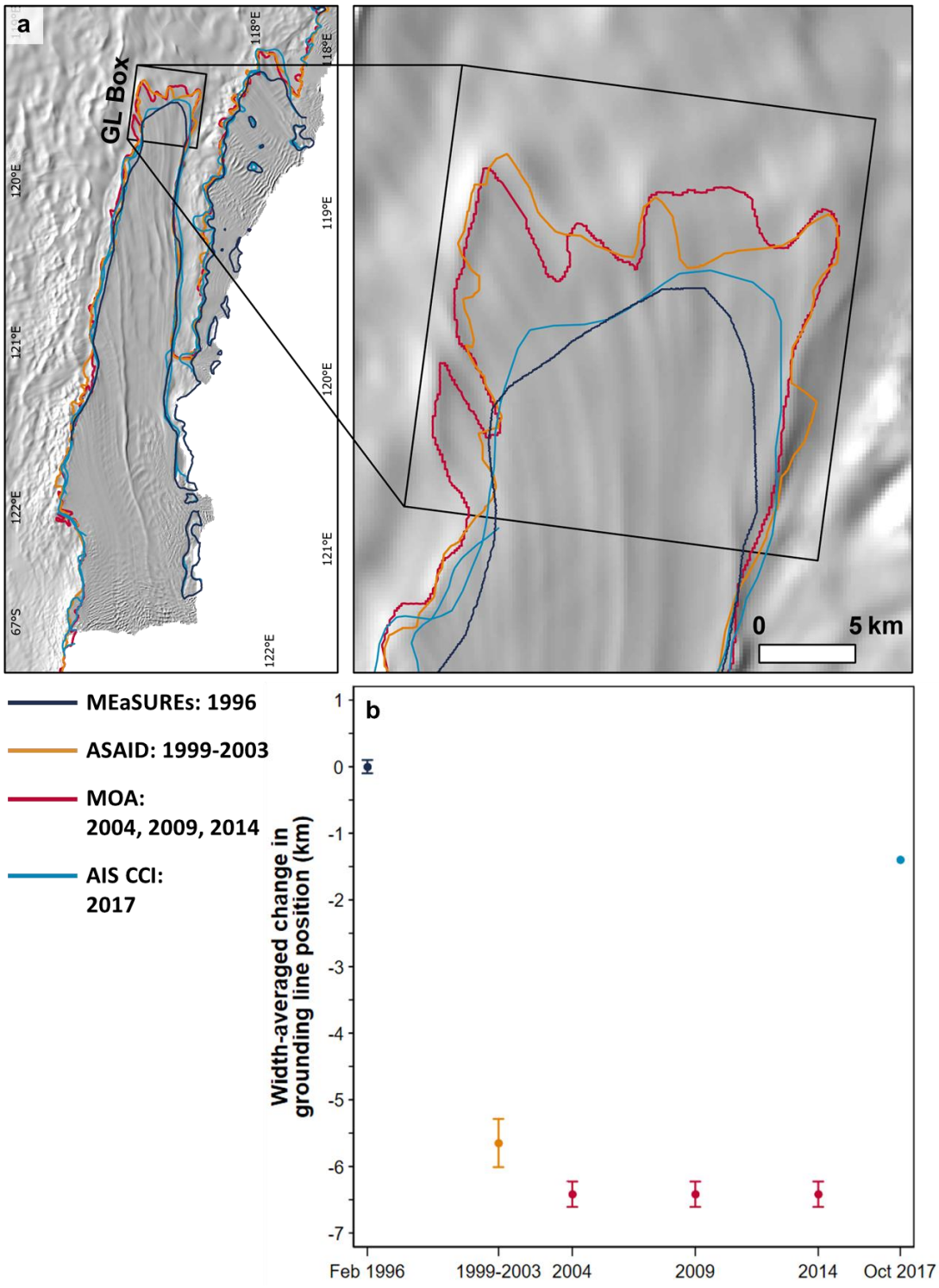

Figure 4.7: (a) Grounding line positions at MUG from the MEaSUREs, ASAID, MOA and AIS CCI datasets, overlaid on a hill-shaded version of the Reference Elevation Model of Antarctica (Howat et al., 2019). (b) Width-averaged change in grounding line position within the GL box, relative to February 1996.

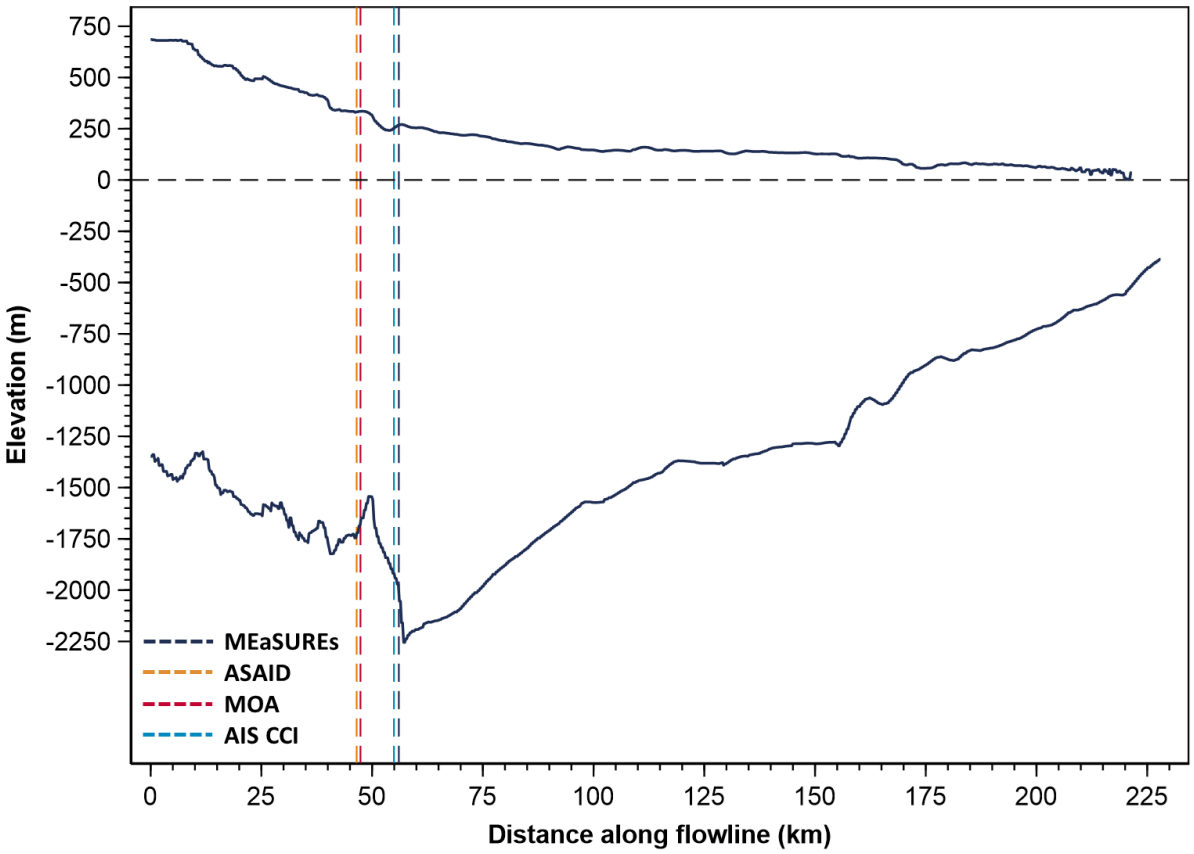

Figure 4.8: Ice surface and bed topography elevation extracted along Flowline AB from BedMachine v2. Dashed lines are the grounding line positions as defined by the MEaSUREs (1996), ASAID 1999 – 2003), MOA (2004, 2009, 2014) and AIS CCI (2017) datasets. Note the alignment between the ASAID (orange) and MOA (red) GLs and a rise in both bed and ice surface elevation.

Table 4.2: Details of the grounding line change results and associated datasets.

Timestamp	Method	Dataset	Width-averaged change in GL position since 1996 (km)	RMSS Error (m)
Feb 1996	DInSAR	MEaSUREs	0	±100
1999-2003	Static	ASAID	-5.66	±362
2004	Static	MOA	-6.42	±190
2009	Static	MOA	-6.42	±190
2014	Static	MOA	-6.42	±190
Oct 2017	DInSAR	AIS CCI	-1.40	NA

4.5 Variability in sea-ice conditions adjacent to MUIS

Mapping of sea ice conditions between October 1963 and March 2022 shows a large summer sea ice presence adjacent to MUIS in most years (Fig. 4.9). This is broadly characterised by the presence of the Dalton Iceberg Tongue (DIT) buttressing the MUIS terminus; an area of landfast sea ice occupying the coastline between MUIS and Totten Glacier; an area of open ocean or sea ice mélange to the west of the DIT; and either fractured sea ice or open ocean further from the coastline. This is illustrated in Fig. 4.10, which shows sea ice during two contrasting years featuring the DIT at limited (2007) and full (2018) extents. Unfortunately, variable cloud and image coverage beyond the DIT led to an inconsistency in the mappable region, therefore preventing a quantitative assessment of changes in sea ice conditions between each timestamp. Generally, no clear trends or obvious temporal changes in the distribution and occurrence of sea ice mélange and fractured sea ice were observed.

Figure 4.11a shows the spatial distribution of the DIT as a density map of the DIT extent at each timestamp. The western margin of the DIT is defined by the Dalton Polynya, which occupies the area adjacent to Outlet East, whilst a smaller polynya at roughly 66°S, 123°E allows greater migration of the eastern DIT margin. Two notches are observed to occur near-consistently within the western edge of the DIT, suggestive of increased polynya intensity in these regions.

The DIT is recorded to vary in extent through time, including a significant reduction in size following several disaggregation events. Between 1997 and December 2013, the DIT underwent three cycles of retreat and expansion between its minimum and maximum extents. Since then, however, the DIT has never fully recovered to its pre-2013 average maximum, instead occupying an area reduced by around 35%. Of particular note are its limited extent observed in January 2000 and 2007, February 2010 and 2016, and at each timestamp between Feb 2020 and March 2022 (Fig. 4.9). The ~45 km-long band of landfast sea ice also diminishes during these months, leading to an expansion of open-ocean area towards to coast.

These changes in DIT extent display a complex relationship with the MUIS terminus position (Fig. 4.11b). At the start of the time series, a correlation between the extent of the DIT and the terminus position suggests that a period of terminus advance coincides with expansion of the DIT. The inverse is seen when a significant reduction in DIT extent between December 2006 and the 20th of January 2007 correlates closely with iceberg calving across the ice front, causing the terminus to retreat rapidly to its position of minimum extent. However, the

observations suggest a temporal decoupling over time, such that an increase or decrease in the DIT area is not immediately followed by an advance or retreat of the terminus. Instead, since 2006, the time delay before a terminus response appears to depend on the magnitude of change in DIT extent. Under this principle, a larger change in DIT extent prompts a more rapid, but not necessarily greater, change in terminus position. In summary, this study observes significant variations in the DIT extent which may influence terminus behaviour within its ~6.5 km margin of change.

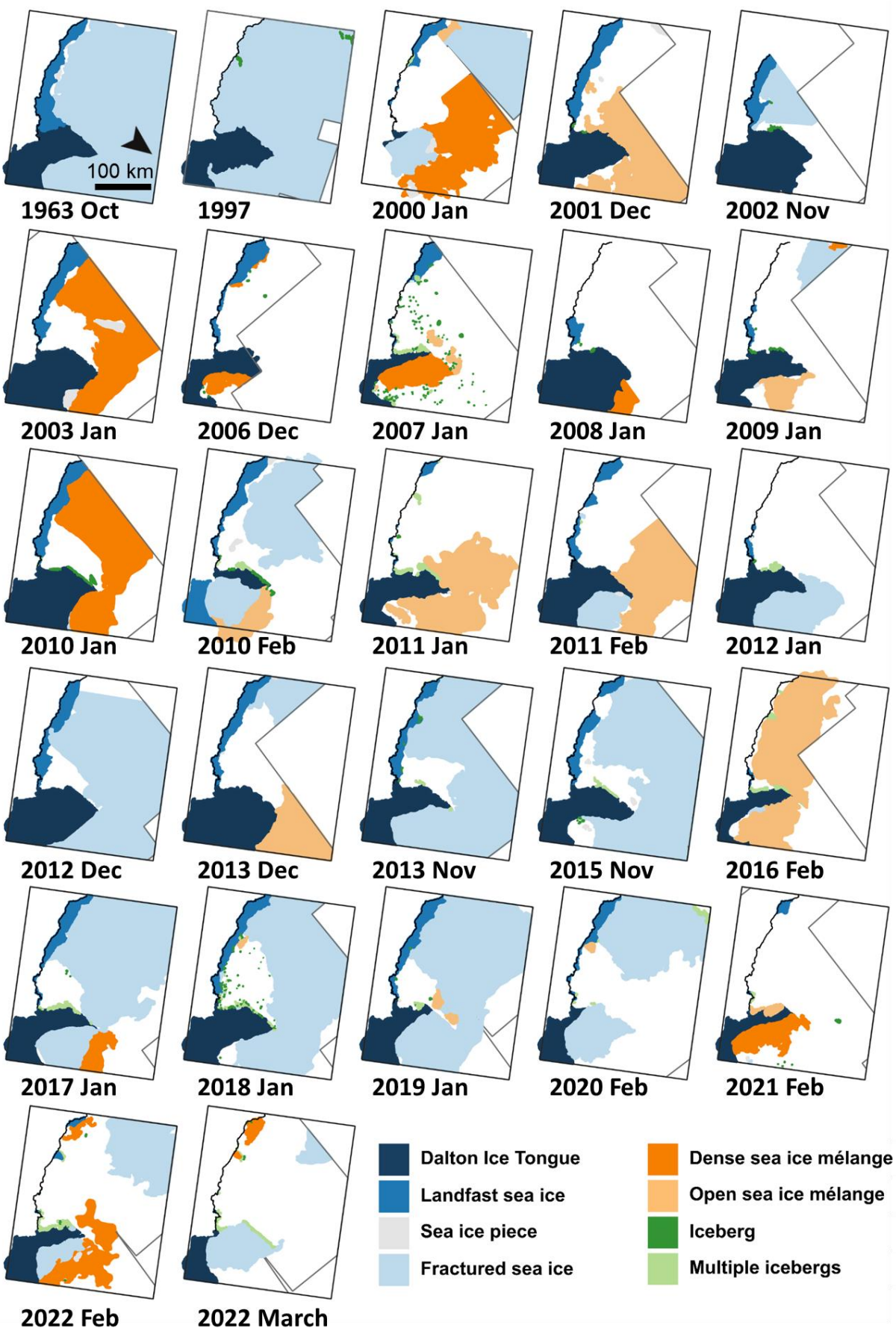

Figure 4.9: Sea ice conditions adjacent to MUIS at 27 timestamps between October 1963 and March 2022. Grey outlines define the extent of available satellite imagery.

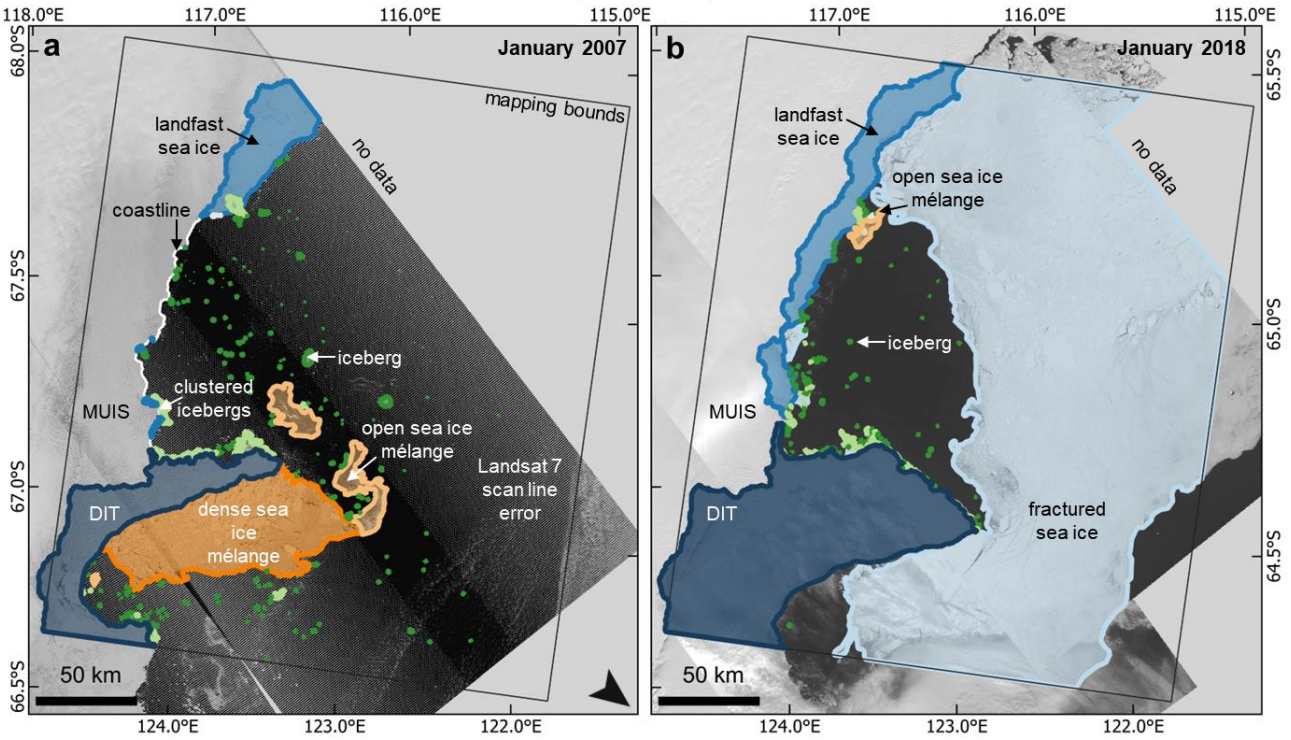

Figure 4.10: Sea ice distribution adjacent to MUIS during (a) 2007 and (b) 2018, mapped from Landsat 7 and Landsat 8 imagery, respectively.

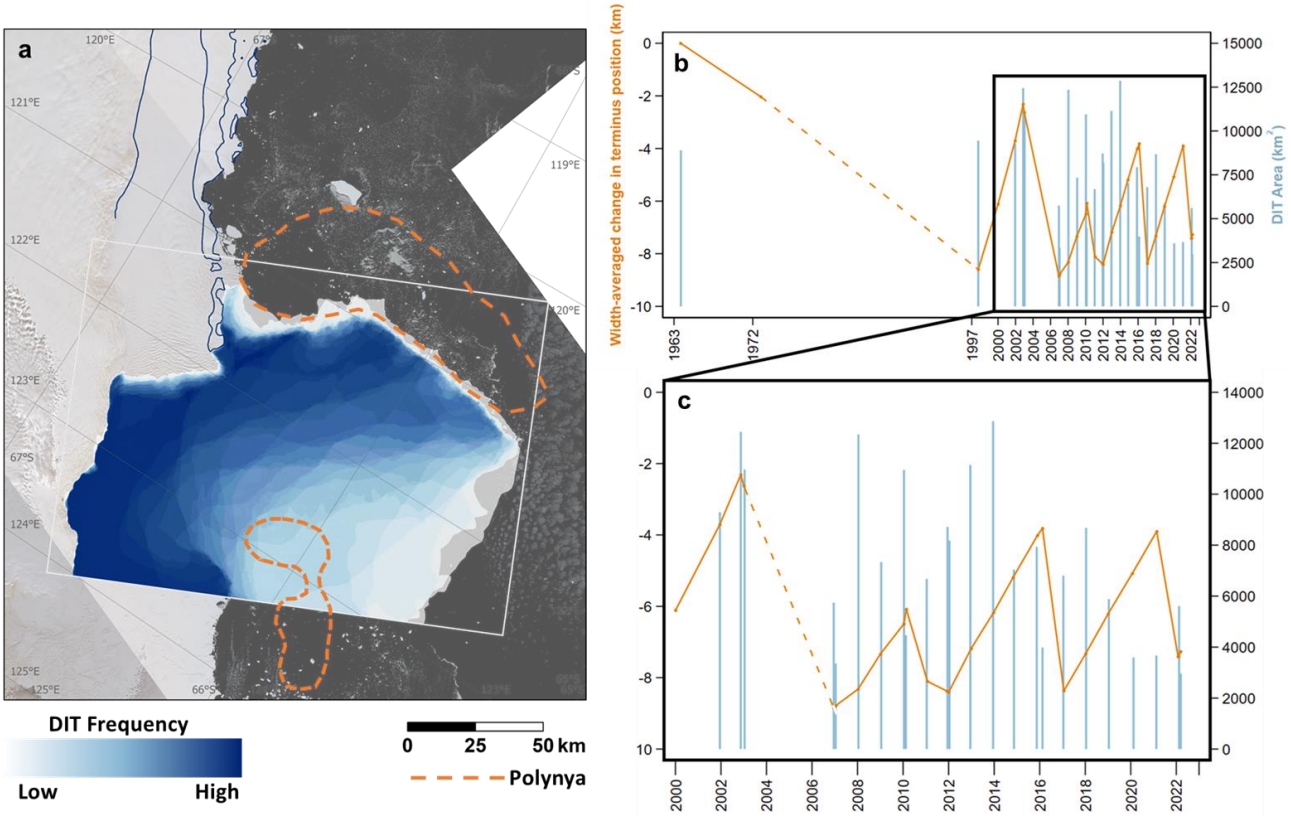

Figure 4.11: (a) Spatial frequency of the DIT across 27 timestamps from 1963 to 2022. The darkest blue represents the region most frequently occupied by DIT ice, or its minimum extent, and the lightest colour represents the region least frequently occupied by DIT ice, coinciding with its maximum extent. Dashed orange lines show the approximate positions of the Dalton Polynya (west) and a smaller polynya (east), from a map of polynya frequency presented by Khazendar et al. (2013). (b) Bars show the areal extent (km^2) of the DIT at each timestamp between October 1963 and March 2022. The navy line represents width-averaged change in terminus position (km) over the same period. (c) Subset of the data displayed in (b), showing DIT area and terminus change between January 2000 and March 2022.

5 Discussion

5.1 The recent stability of Moscow University Ice Shelf and Moscow University Glacier

5.1.1 Summary of observed changes at MUIS and MUG

The results presented here build on previous estimates of regional (Mohajerani et al., 2018) and local (Rignot et al., 2019; Miles et al., 2022) mass balance to imply a largely stable rate of ice discharge from the Moscow University catchment over recent decades. A natural calving cycle was upheld at MUIS throughout the observational period, and both the grounded and floating regions exhibited negligible overall change in ice surface velocity between 2000 and 2021. However, whilst total surface lowering on MUG has been moderate (about -4.8 m overall between 1993 and 2020, or 0.17 m yr^{-1} for the same period), this study also observed a period of accelerated thinning (~0.86 m yr^{-1}) between 2011 and 2016. Alongside the observed grounding line retreat of 1.4 km (1996 – 2017), this suggests that MUG may be starting to show the early indicators of dynamic change.

5.1.2 Recent thinning of Moscow University Glacier

The spatial pattern of surface elevation change (2003 – 2019; Fig. 4.6a) shows that surface lowering is concentrated in regions of faster ice flow, whereby MUG and Tributary A have been thinning at significantly higher rates than surrounding areas of the grounded ice sheet. Whilst the average rate of thinning is moderate (-0.57 m yr^{-1} close to the grounding line, 2003 – 2019), this coincidence between height change and ice flow velocity is consistent with observations of dynamic thinning elsewhere, for instance within the Amundsen Sea Sector (McMillan et al., 2014) and at Totten Glacier (Khazendar et al., 2013; Li et al., 2015; Roberts et al., 2018). Further, elevation changes related to SMB processes such as reduced accumulation are typically less spatially variable (Sole et al., 2008; Bevan et al., 2015); as such, it is implied that the recorded thinning is predominately dynamic.

Much of the observed surface lowering occurred during the 2011 – 2016 period, when the rate of thinning upstream of the grounding line accelerated to -0.86 m yr^{-1} following negligible change between 2005 and 2010. However, whilst an increased rate in dynamic thinning is typically accompanied by enhanced ice flow velocity, no corresponding velocity signal was observed in this study. This lack of dynamic coupling differs to the recent behaviour of Totten Glacier, where an ice flow acceleration of 120 ± 27 m yr^{-1} between 2000 and 2007 coincided with increased thinning on the main glacier trunk (Li et al., 2016; Roberts et al., 2018), indicative of a system-wide change in flow regime. Due to the scope of this study, a regional

change in surface mass balance cannot be ruled out as the cause of accelerated thinning at MUG; therefore, it is possible that long term thinning was exacerbated by reduced snowfall during the 2011 – 2016 period. Nonetheless, such a significant increase in the rate of thinning would require a considerable reduction in mass input, and modelled SMB suggests that no such changes have occurred in East Antarctica over recent years (Kittel et al., 2021). In addition, dynamic thinning at a similar rate of 0.7 m yr^{-1} on Totten Glacier (1996 – 2013, Li et al., 2015) indicates that the amount of surface lowering observed here exceeds that which could be attributed to regional mass input changes. It should also be noted that although many of the velocity values used in this study have relatively low degrees of uncertainty (Table S6 – S10), these uncertainty estimates may not fully reflect the true error within the ITS_LIVE dataset. The autoRIFT feature tracking technique used to produce the ITS_LIVE mosaics relies on stable surfaces in order to calibrate between image pairs (Gardner et al., 2018). A lack of suitable reference points near to MUG means that the data is likely based on calibration points located hundreds of kilometers from the main trunk of flow. This drawback may leave small fluctuations in ice flow velocity undetected, as well as lead to miscalculated levels of uncertainty. Therefore, whilst the accelerated thinning observed here plausibly reflects the initial stages of dynamic thinning, further observations of both ice flow velocity and SMB are required in order to validate this interpretation.

5.1.3 Uncertainty in observed grounding line change

Long term grounding line migration is a critical indicator of ice sheet stability (Joughin et al., 2012). To date, Antarctic grounding line locations have been identified using various techniques which detect a number of distinct features within the wider grounding zone. These features can be located several kilometers apart (Fricker and Padman, 2006), and the ambiguous use of the term ‘grounding line’ makes it difficult to accurately compare between datasets (Friedl et al., 2020). At MUG, the grounding line positions derived via ‘static’ methods of break-in-slope detection (MOA and ASAID) clearly deviate from those based on the landward limit of tidal flexure at the ice sheet margin (Fig. 4.8). Static methods are known to have higher levels of associated uncertainty (Fricker and Padman, 2006) and in areas of fast ice flow, such as MUG, negligible change in basal resistance across the transition from grounded to floating ice can prohibit the development of a visible inflection on the ice surface (Fricker et al., 2009). Additionally, surface inflections may result from undulations in the bed topography. The MOA and ASAID grounding line positions are closely aligned at MUG, and whilst this could represent initial retreat from the MEaSUREs 1996 location and subsequent stability between 1999 and 2014, it is possible that these

observations actually reflect a surface expression of the underlying bed. Indeed, the DInSAR-derived grounding line positions imply a more limited retreat signal between 1996 and 2017, and minimal change in both inland velocity and ice discharge (Miles et al., 2022) suggests that recent retreat is yet to induce a dynamic velocity response beyond the grounding zone. Considering the bed elevation profile (Morlighem, 2020), further retreat could reasonably extend to the mapped MOA location. However, beyond that, MUG lies on a prograde slope extending into the catchment basin; this suggests that persistent retreat along the main trunk of flow is unlikely in the near future (Schoof et al., 2007).

5.1.4 Comparison to Totten Glacier: evidence of variability between East Antarctic outlet glaciers

The results reflect a broad pattern of ice discharge variability between East Antarctic outlet glaciers (Miles et al., 2022). Compared to the magnitude of terminus retreat (Miles et al., 2013, 2016, 2017), ice flow acceleration (Li et al., 2016; Gardner et al., 2018; Greene et al., 2018; Miles et al., 2021) and grounding line migration (Li et al., 2015; Konrad et al., 2019; Rignot et al., 2019; Brancato et al., 2020; Pelle et al., 2021) observed elsewhere, MUG has exhibited a relatively stable dynamic regime, particularly prior to 2011. This observation aligns with previous studies which emphasise contrasting rates of mass loss between MUG and neighbouring Totten Glacier, which instead underwent substantial and sustained dynamic change between the 1970s and mid-2010s (Mohajerani et al., 2018; Rignot et al., 2019). Observations show that Totten's grounding line has been retreating (Li et al., 2015), the glacier has sped up (e.g. by 18 ± 3% between 2000 and 2007; Li et al., 2016) and surface lowering has occurred at rates of up to 1.7 m ± 0.2 m per year (2003 – 2008; Khazendar et al., 2013). These changes have been related to reduced buttressing due to prolonged thinning of Totten's floating ice shelf, understood to be driven by incursions of warm mCDW into the sub-ice shelf cavity (Rintoul et al., 2016; Li et al., 2016; Greene et al., 2017). However, ice discharge from Totten has slowed more recently (Greene et al., 2017; Rignot et al., 2019; Miles et al., 2022). Multiple studies have attributed this variability to fluctuations in the rate of basal melting, which is modulated by the volume of mCDW adjacent to the ice front (Greene et al., 2017; Roberts et al., 2018; Silvano et al., 2019), as well as polynya activity (Khazendar et al., 2013) and intrinsic ocean processes (Gwyther et al., 2018). Although warm mCDW has been observed along the Sabrina Coast (Silvano et al., 2017), and is known to drive thinning of MUIS (Khazendar et al., 2013), MUG has not exhibited the same magnitude of dynamic variability as seen at Totten Glacier. This suggests that, to date, the Moscow University catchment has responded less sensitively to ocean forcing.

5.2 Topographic confinement of MUIS limits dynamic change

Through observations and modelling of ice sheet change, previous studies (e.g. Nick et al., 2012; Jamieson et al., 2014; Stokes et al., 2014; De Rydt et al., 2015; Pegler, 2018; Hill et al., 2021) have identified the control of channel width and topographic pinning on ice shelf stability. Ice shelves which occupy narrow, fjord-like embayments are typically subject to high resistive shear stresses, increasing their capacity to buttress grounded ice (Kowal et al., 2016; Pegler, 2016; Minchew et al., 2016; Hill et al., 2021). MUIS is well confined within the Reynolds Trough and, as such, over 93% of the ice shelf is estimated to buttress the flow of MUG (Fürst et al., 2016). This configuration contrasts with the floating extensions of other Wilkes Land outlet glaciers, which are generally unconstrained (e.g. Frost Glacier) and exert comparatively little buttressing force (Miles et al., 2013). Here, it is suggested that lateral buttressing from the embayment plays a critical role in stabilising MUIS, and thus in limiting dynamic change at MUG.

Changes in terminus position are observed only across the unconfined region of MUIS, potentially indicating that upstream pinning between the coast and peninsula prevents extensive retreat into the buttressing shelf area. Further, ice flow velocity appears dynamically insensitive to episodic calving and sea ice loss at the ice front. Landfast sea ice has previously been shown to stabilise Antarctic ice shelves and floating ice tongues (Massom et al., 2010, 2018), including those in Wilkes Land (Miles et al., 2016, 2017; Greene et al., 2018; Wearing et al., 2020; Arthur et al., 2021). Whilst the results presented here suggest a similar mechanical coupling between the DIT and the MUIS terminus, this effect does not appear to propagate beyond the passive ice shelf region. For instance, the MUIS ice front retreated in 2007 following a collapse of the DIT. This was consistent with the disaggregation of the neighbouring Voyeykov Ice Shelf (VIS) (Arthur et al., 2021) and calving of Porpoise Bay outlet glaciers (Miles et al., 2017) during the same summer season, with such terminus destabilisation events being attributed to wind- and ocean-driven sea ice break-up (Stammerjohn et al., 2011; Miles et al., 2017; Arthur et al., 2021). Because the associated air flow anomaly and warm sea surface temperatures extended across the Sabrina Coast (Miles et al., 2017), the DIT retreat possibly resulted from the same set of atmospheric and oceanic conditions. However, whilst VIS underwent a period of flow acceleration between 2007 and 2008 (Arthur et al., 2021), this study found no coincident velocity increase at MUIS. Topography is therefore inferred to play a critical role in maintaining the buttressing capacity of MUIS by exerting high lateral stresses across the

shelf, thus ensuring stability during periods of DIT disintegration and terminus retreat.

Petermann Glacier in northwest Greenland (Fig. 5.1), which has an ice tongue with a topographic setting comparable to MUIS, has exhibited similar dynamic stability in the past (Bevan et al., 2012). Here, significant calving of the freely floating ice tongue in 2010 had a negligible effect on grounded ice speed, implying that buttressing is dominated by the remaining laterally confined shelf area (Nick et al., 2012; Hill et al., 2018). This is demonstrated in modelled simulations which predict an acceleration in ice discharge following ice tongue thinning and collapse near to the grounding line (Hill et al., 2021; Åkesson et al., 2022). Importantly, modelling of the Antarctic ice flux response to perturbations within buttressing shelves suggests that MUG, like Petermann, is most sensitive to thinning at the grounding zone (Reese et al., 2018). Despite this, the modest grounding line retreat reported here does not appear to have initiated a dynamic velocity response inland. This implies that the buttressing capacity of MUIS has, to date, remained sufficient to inhibit an ocean-driven increase in ice discharge from the Moscow catchment.

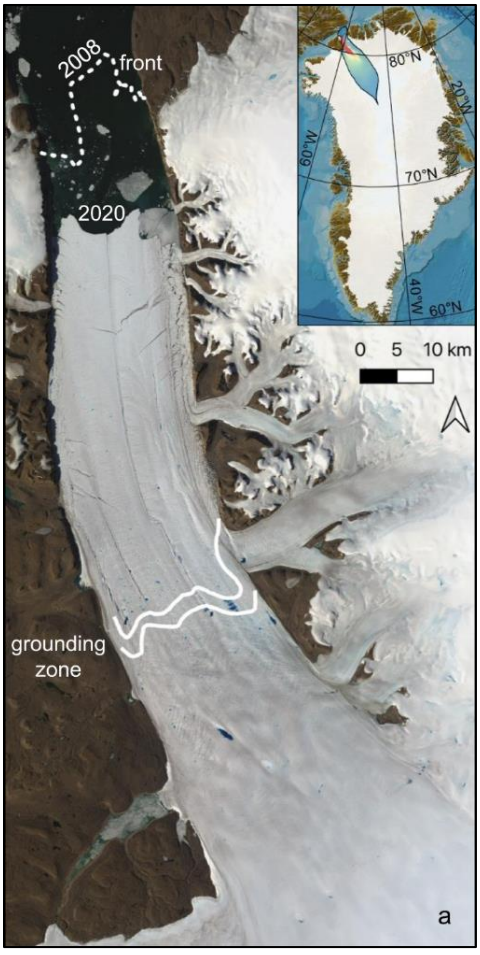

Figure 5.1: Petermann Glacier, northwest Greenland, from Åkesson et al. (2022).

5.3 The stability and significance of the Dalton Iceberg Tongue

Section 5.2 suggests that although DIT disaggregation events can de-stabilise the immediate MUIS ice front, such de-buttressing has no observable impact on inland flow. Nonetheless, by influencing ocean circulation close to the ice front, the DIT may be an important determinant of basal melt rates at MUIS. Strong katabatic winds offshore of the Sabrina Coast frequently remove newly formed sea ice, facilitating high rates of sea ice production and associated brine rejection. Cool, dense waters form as a result, sustaining the Dalton and eastern polynyas which are known to influence basal melt rates at both Totten and MUIS (Fig. 5.2; Tamura et al., 2008; Khazendar et al., 2013; Gwther et al., 2014). Here, mapping of the DIT reveals a reduction in extent along its eastern margin since 2013. It is speculated that this change may have been forced by an intensification of the eastern polynya, with an associated migration towards the MUIS terminus (Fig. 5.2a). Ocean stratification is thus likely to have been reduced, restricting warm water access to the ice shelf cavity and limiting rates of basal melt (Gwyther et al., 2015). Khazender et al. (2013) also emphasise that the intrusion of cold polynya waters can reduce rates of thinning. Whilst the precise mechanism of forcing remains uncertain, further reduction in the extent of the DIT may be accompanied by a decreased rate of ice shelf thinning in the near future.

However, if the DIT extent was to reduce indefinitely, basal thinning rates may increase. Van Achter et al. (2022) found that higher simulated basal melt rates at MUIS were coincident with reduced sea ice production. This implies that a total disaggregation of the DIT - and no recovery thereafter - would limit polynya activity and ocean destratification, favouring inflow to the sub-ice shelf cavity. Warm mCDW has been observed on the continental shelf close to MUIS (Silvano et al., 2017), and the ~1.4 km of grounding line retreat recorded in this study suggests that warm water is able to access the MUG grounding zone. Such intrusions enhance ocean-driven thinning of Antarctic ice shelves (Pritchard et al., 2012; Silvano et al., 2017), which reduces their capacity to suppress inland flow (Gagliardini et al., 2010; Fürst et al., 2016). At Totten Glacier, this has caused periods of flow acceleration and dynamic thinning in recent years (Greene et al., 2017; Pritchard et al., 2012; Flament and Remy, 2012; Khazendar et al., 2013; McMillan et al., 2014; Rintoul et al., 2016; Mohajerani et al., 2018). The limited evidence of dynamic change at MUG implies that, to date, basal melting of MUIS has been insufficient to initiate a velocity response up-ice. However, since the buttressing capacity of MUIS is unlikely to be reduced by extensive calving, ocean-driven ice shelf thinning is likely the greatest potential cause of increased ice discharge from the Moscow catchment in the future.

Recent observations show that greater volumes of increasingly warm CDW have been intruding onto the continental shelf in the Indian Ocean Sector of East Antarctica (80 – 160^{o} E) since the 1990s (Silvano et al,. 2017; Herraiz-Borreguero & Garabato, 2022), driving rapid rates of ice shelf basal melting (Rintoul et al., 2016; Ribeiro et al., 2021). This warming has been associated with the poleward migration of the Antarctic Circumpolar Current, driven by a southerly shift and strengthening of the westerlies under an increasingly positive trend in the Southern Annular Mode (Abram et al., 2014; Spence et al., 2014; Yamazaki et al., 2021; Herraiz-Borreguero & Garabato, 2022). Since this trend is predicted to continue as the climate warms (Downes and Hogg, 2013; Zheng et al., 2013; Spence et al., 2014), it is likely that intensified on-shelf delivery of warm CDW, and, therefore, enhanced ice shelf melting, will persist throughout the 21st century (Herraiz-Borreguero & Garabato, 2022). Indeed, modelling by Jordan et al. (in review) suggests that enhanced basal melt rates at MUIS will likely contribute to increased mass loss from Wilkes Land in the next 200 years. In addition, meltwater influxes are thought to partially stratify the upper ocean and inhibit Dense Shelf Water (DSW) formation within polynyas along the Sabrina Coast, allowing the increased delivery of mCDW towards TIS and MUIS (Khazendar et al., 2013; Silvano et al., 2018; Nakayama et al., 2021). If basal melt rates continue to rise, the subsequent freshwater input can be expected to further impede convection within the Dalton Polynya, thereby contributing to a positive feedback loop of enhanced ice shelf melting (Bronselaer et al., 2018; Silvano et al., 2018). This study therefore recommends continued monitoring landfast sea ice production, polynya activity and subsurface ocean temperatures along the Sabrina Coast.

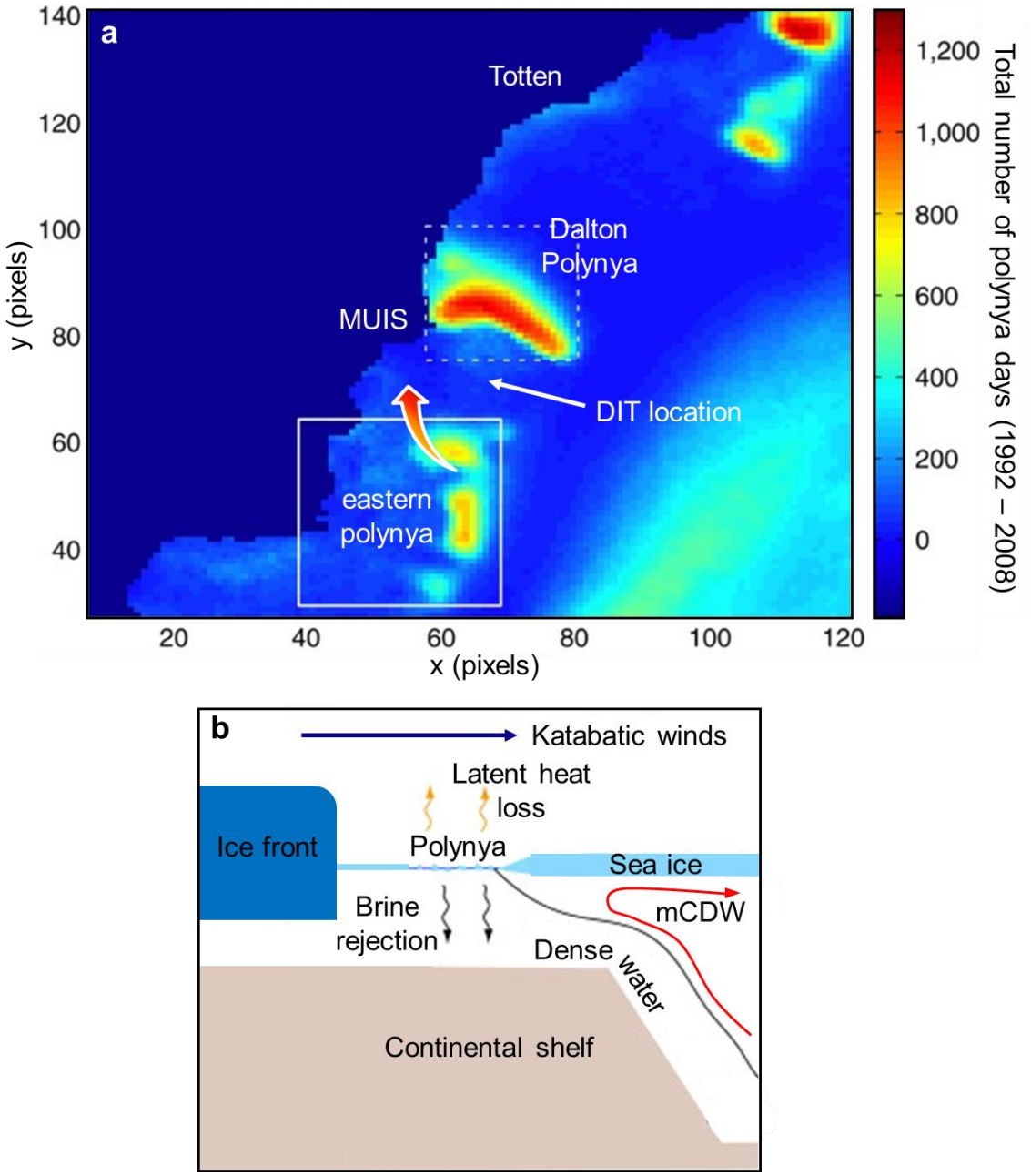

Figure 5.2: (a) Frequency of polynya occurrence during June to September for the years 1992 to 2008 within 5 x 5 km pixels, adapted from Khazendar et al. (2013). The graded arrow represents the suggested change in polynya intensity and location. (b) Schematic of latent heat polynya formation and associated diversion of mCDW, adapted from Talley et al. (2012).

5.4 Comparison to results from Li et al. (2022a)

A new study by Li et al. (2022a) suggests that MUG has recently accelerated and thinned following significant retreat of the grounding line. The paper presents new remote sensing observations of ice dynamics at MUG, MUIS and Totten Glacier, and entered peer review

after the data analysis for this thesis had been completed. However, whilst both studies include analysis of grounding line migration, ice surface velocity, surface elevation change and calving at MUG and MUIS, there are some discrepancies between the findings. This section briefly reviews these differences, which are outlined in Table 5.1.

5.4.1 Grounding line change

Li et al. (2022a) derive a number of grounding zone observations along the Sabrina Coast using DInSAR Sentinel-1AB interferograms and ICESat and ICESat-2 laser altimetry data. These are assessed relative to the MEaSUREs 1996 grounding line position (Rignot et al., 2011) to reveal both short term, tide-modulated change and a long term trend of grounding line retreat at MUG. Using the landward limit of tidal flexure (Point F) identified from ICESat-2 data, the study reports an overall retreat of 9.37 ± 1.04 km at the eastern flank and 13.85 ± 0.08 km at the western flank of the MUG grounding zone between 1996 and 2020, equivalent to average retreat rates of 0.39 and 0.58 km yr^{-1}, respectively. These values were derived from Point F locations along two ICESat-2 tracks, as shown in Fig. 5.3a. The largest retreat value is measured using a single flowline connecting two ICESat-2 points. The first point sits on the lateral margin of the MEaSUREs 1996 grounding line, and the second point, dated to 2020, is located further inland. However, it is unclear how the position of each flowline was determined, and it is noted here that the two points may not be placed at corresponding positions along the curvature of the grounding line, such that they cannot be connected along one line which accurately represents the flow trajectory. This results in a larger retreat signal being observed than would be found if change had been assessed along an alternative flowline. For instance, if the flowline was positioned as illustrated by the white dashed line in Fig. 5.3a, a reduced grounding line retreat signal of approximately 7 km is observed. To this effect, the 13.85 km of retreat is significantly greater than any other change measured along other ICESat-2 tracks in the area.

When compared to the ICESat-2 observations, the DInSAR-derived grounding line positions indicate less extensive retreat along the eastern flank. This includes both the Li et al. (2022a) 2017 – 2021 and AIS CCI 2017 observations, which are similarly dated and in good agreement (Fig. 5.3b). It is possible that the ~6 km discrepancy between the DInSAR grounding line positions and those derived from ICESat-2 altimetry data is due to short-term migration induced by ocean tides (Milillo et al., 2017; Li et al., 2022a). However, whilst Li et al. (2022a) record such tidally-induced migration over short (6-day) timescales, this is less than 6 km in extent. Additional observations of changes at the MUG grounding zone,

especially in relation to tidal amplitude, may help to better explain the observations made to date.

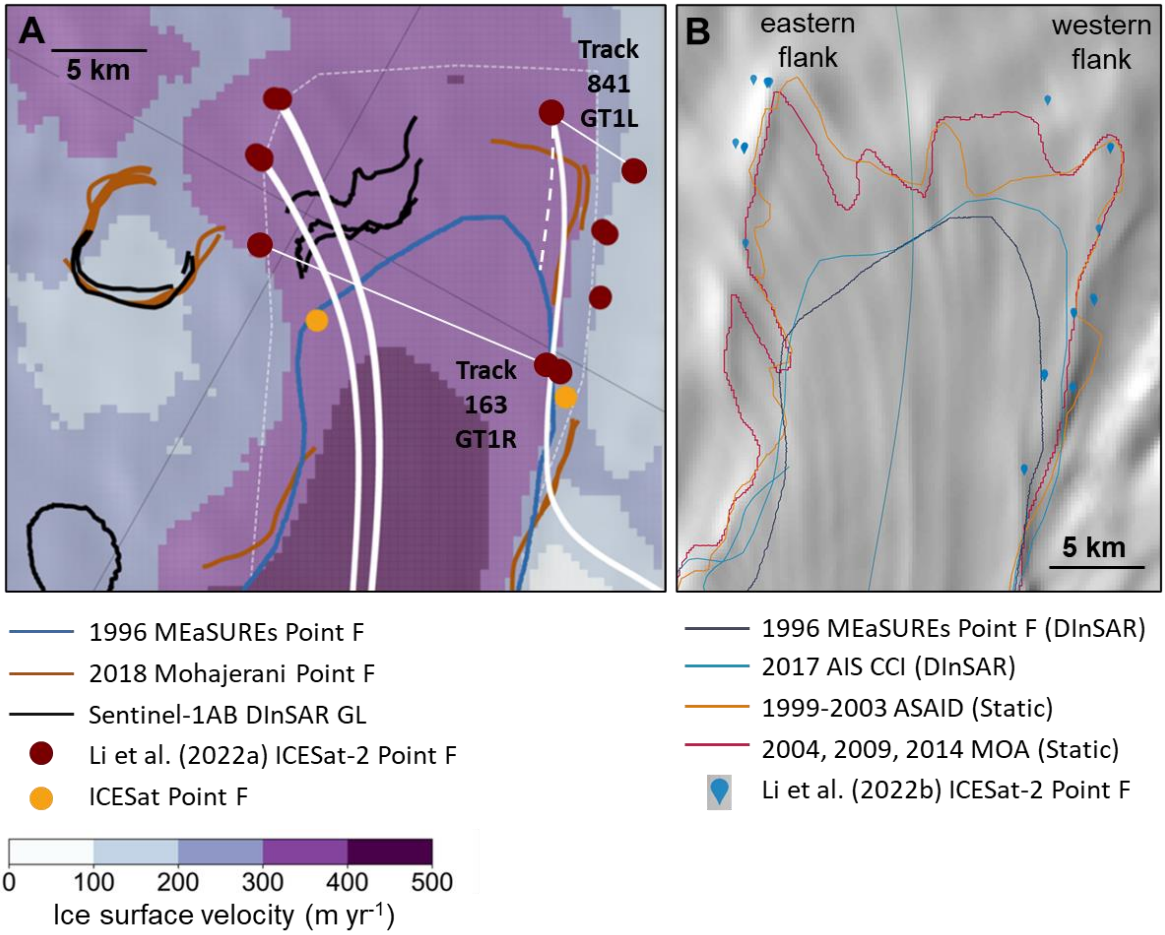

Figure 5.3: (a) Adapted from Figure 2a in Li et al. (2022a), showing recently recorded grounding line positions at MUG overlaid on MEaSUREs ice flow velocity (Rignot et al., 2017). Large white lines are the flowlines used by Li et al. (2022a) to interpret grounding line retreat between ICESat-2 tracks, and the dashed white line represents an alternative flowline position. (b) Location of grounding line positions used in this thesis, with ICESat-2 Point F positions from Li et al. (2022b). The background image is REMA (Howat et al., 2019).

5.4.2 Ice surface velocity

To investigate the sensitivity of MUG to observed grounding line retreat, Li et al. (2022a) assessed changes in ice surface velocity between 2005 and 2018. Similar to the method employed here, annual velocity measurements are extracted from the MEaSUREs (2005 – 2016; Mouginot et al., 2017) and ITS_LIVE (2016 – 2018; Gardner et al., 2018) ice surface velocity datasets as the average value within a sample box (Fig. 5.4). Both studies report

negligible overall change in ice surface velocity; however, Li et al. (2022a) observe a 50 m yr^{-1} flow acceleration between 2007 and 2010 which is not represented in the ITS_LIVE data used in this thesis. Observations elsewhere, such as at Totten Glacier (Greene et al., 2018), have shown that ice surface velocity can be spatially variable on large outlet glaciers and ice shelves. Thus, this difference may relate to the positioning of the sample boxes used in each study. Li et al. (2022a) sample velocity within the region of the grounding zone, whilst the 2007 – 2010 data presented here is extracted from locations on MUIS due to low data coverage on MUG. This implies that the 2007 – 2010 velocity signal observed by Li et al. (2022a), which is suggested to be a dynamic response to grounding line retreat, was limited to the grounding zone and did not propagate down-ice.

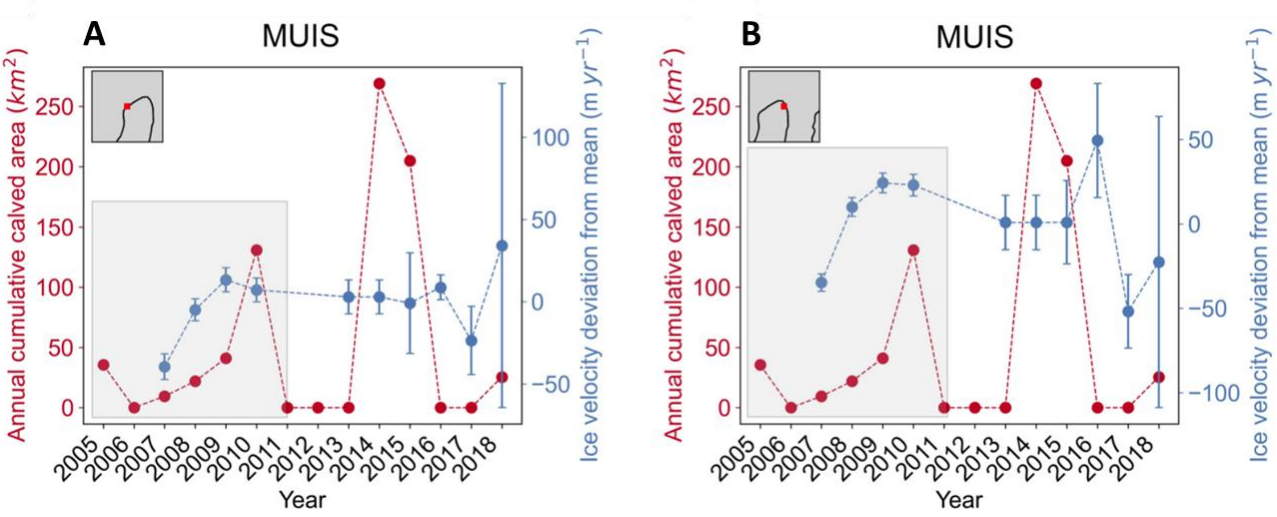

Fig. 5.4: Figure 13 from Li et al. (2022a). Time series of average ice surface velocity within each sample box in the MUIS grounding zone, extracted from the MEaSUREs (2005 – 2016; Mouginot et al., 2017) and ITS_LIVE (2017 – 2018; Gardner et al., 2018) datasets. The red plot shows the annual cumulative calved area from the MUIS terminus (Qi et al., 2021).

5.4.3 Ice surface elevation change

Both studies observed a spatial correlation between areas of surface lowering and faster ice flow on MUG. Li et al. (2022a) found a maximum thinning signal of -0.9 ± 0.01 m yr^{-1}, which occurs close to the MUG grounding zone and is in near agreement with the maximum thinning rate recorded in this thesis (-0.86 m yr^{-1}). Using RACMO 2.3 modelled surface mass balance estimates, Li et al. (2022a) find that surface mass balance processes likely accounted for less than 0.16 m of thinning per year at MUG between 2010 and 2016. Therefore, the observed thinning is interpreted as dynamic; alongside the recorded

fluctuations in ice surface velocity, the observations made by Li et al. (2022a) suggest that MUG has responded dynamically to recorded grounding line retreat in the past two decades.

5.4.4 Summary

Table 5.1 summarises the findings for each parameter common to both studies. Clear discrepancies exist between observed grounding line changes, which may be due to differences in the methods employed and the sample locations. Whilst Li et al. (2022) record significant grounding line retreat at both the ice shelf area between MUIS and Totten and the western flank of MUIS, this study observed a limited retreat signal across the main trunk of flow. Similarly, Li et al. observe a flow acceleration within the MUG grounding zone which is not represented in the ITS_LIVE data sampled here, either close to the grounding line or further down-ice. However, observed patterns of surface elevation change were consistent across the two studies, which both suggest that MUG has been dynamically thinning in recent decades. In the context of the additional observations made by Li et al., this thinning signal implies that pervasive, ocean-driven dynamic change at MUG is already underway. By comparison, the results presented here indicate relatively little change at MUIS and MUG since the 1990s, and that - despite a period of accelerated, potentially dynamic, thinning - a coupled velocity-elevation response to ocean forcing is yet to be initiated.

Table 5.1: Overview of methods, temporal resolution (TR) and results for each parameter analysed in both Li et al. (2022a) and this thesis (continued overleaf).

		Li et al. (2022a)	Thesis
Terminus change	**Method**	Annual cumulative calved iceberg area at the MUIS ice front extracted from the circum-Antarctic iceberg calving dataset (Qi et al., 2021).	Change in terminus position derived from satellite imagery and calculated via the box method.
	TR	2005 – 2018, data presented when total calved area is larger than 1 km^2.	1963, 1972, 1997, 2000 – 2022, annually 2000 – 2003, 2006 – 2022.
	Results	No change in mean annual cumulative calved area 2005 – 2018.	Overall retreat of 7.3 km at the MUIS terminus, 1963 – 2022. Cyclical pattern of advance and retreat within a ~6.5 km margin since 2000. Slight advance of Outlet West and Outlet East.
Ice surface velocity	**Method**	a. MEaSUREs V1 (Mouginot et al., 2017a, 2017b) b. ITS_LIVE image-pair velocities (Gardner et al., 2018, 2019b)	a. ITS_LIVE regional velocity mosaics (Gardner et al., 2018, 2019a) b. ENVEO velocity mosaics (ENVEO, 2022)
	TR	a. Annual, 2005 – 2016 b. Annual, 2017 – 2018	a. Annual, 2000 – 2018 b. Annual, 2019 – 2021
	Results	Zero mean annual velocity change at the MUIS grounding zone 2005 – 2018. Ice flow was 50 m yr^{-1} faster in 2010 than 2007.	Negligible overall change 2010 – 2018 with no significant fluctuations.
Ice surface elevation	**Method**	Surface elevation derived from the CryoSat-2 Swath mode thematic point product.	a. Schröder et al. (2019) SEC dataset b. ITS_LIVE SEC dataset (Nilsson et al., 2021) c. Smith et al. (2020) SEC dataset
	TR	Total SEC, 2010 – 2019.	a. Monthly, 1993 – 2017 b. Monthly, 1993 – 2020 c. Total SEC, 2003 – 2019
	Results	Mean SEC of -0.9 ± 0.01 m yr^{-1} at the MUIS grounding zone, 2010 – 2019. Thinning focused in regions of fast ice flow.	Change from negligible SEC (1993 – 2010) to thinning trend, with an average SEC of -0.86 m yr^{-1} 2011-2016. Thinning focused in regions of fast ice flow.
Grounding line position	**Method**	a. MEaSUREs 1996 ERS 1-2 GL dataset (DInSAR-derived; Rignot et al., 2016) b. Manual delineation of GLs from DInSAR interferograms using Sentinel 1A/B c. Grounding zone mapping from ICESat and ICESat-2 (Li et al., 2022a)	a. MEaSUREs 1996 ERS 1-2 GL dataset (DInSAR-derived; Rignot et al., 2016). b. ASAID GL product (manually delineated from break-in-slope) c. MOA GL product (manually delineated from break-in-slope) d. AIS CCI GL dataset (DInSAR-derived)
	TR	a. 1996 b. 6-day repeat cycle 2017 – 2021. c. 91-day repeat cycle 2003 – 2009. (ICESat) and 2019 - 2021 (ICESat-2).	a. 1996 b. 1999 – 2003. c. 2004, 2009 and 2014 d. October 2017
	Results	Grounding line retreat of 13.85 ± 0.1 km (0.58 km yr^{-1}) at the western flank and 9.37	1.84 ± 0.23 km (0.08 km yr^{-1}) overall grounding line retreat at the western

	± 0.1 km (0.39 km yr^{-1}) at the eastern flank of the main MUIS trunk between 1996 and 2020. 6-day repeat cycles reveal short term, tidally-driven grounding line fluctuations.	flank between 1996 and 2017. Significant difference in grounding line locations derived from DInSAR vs static break-in-slope method.

5.5 Limitations and recommendations for further work

5.5.1 Limitations

5.5.1.1 Ice surface velocity

The ice surface velocity data presented here was derived from the MEaSUREs ITS_LIVE (Gardner et al., 2019) and ENVEO (ENVEO, 2022) datasets, which span the years 2000 – 2021 at MUG and MUIS. In order to extend the timeseries to include dates prior to 2000, the feature tracking software COSI-Corr (Co-registration of Optically Sensed Images and Correlation; Leprince et al., 2007) was trialed on Landsat 1 image pairs from 1989. COSI-Corr has previously proved effective in producing pixel-based maps of velocity and flow orientation on Antarctic outlet glaciers from differential optical imagery (e.g. Chen et al., 2016; Miles et al., 2018; 2021). However, owing to the homogenous spectral signature and lack of potential ground control points across the study area, COSI-Corr was found to produce inaccurate velocity estimates at MUG after multiple iterations. As a result, the velocity timeseries is limited to the past two decades, and lacks observations from the grounded ice region prior to 2010.

5.5.1.2 Grounding line data

Improved consistency between grounding line datasets would help to constrain estimates of grounding line migration at MUG. In particular, greater consensus on the definition of Point F (landward limit of tidal flexure) and Point G (true grounding line position) across datasets would reduce uncertainty when constructing a record of grounding line change from various sources. An improved understanding of tidal variability in the study region, as well as tidal amplitude at the time of observation for a given grounding line position, could also help to explain discrepancies between datasets (Milillo et al., 2017).

5.5.1.3 Regional precipitation rates

Precipitation rates within the Moscow catchment are generally inferred from observations at Casey Station, Law Dome, which is located over 250 km from MUG (Roberts et al., 2015). However, firn density anomalies from Cryosat-2 imply greater variability in snowfall at MUG

compared to Totten (Khazendar et al., 2013), suggesting that the Casey Station record may not be representative of accumulation rates within the Moscow catchment. Whilst previous work has derived such rates from regional climate models (e.g. Khazendar et al., 2013), Agosta et al. (2019) found that neither MAR nor RACMO2 could fully solve for local variability caused by drifting snow transport. Observations of precipitation rates in the region closer to MUG would therefore help to quantify the surface elevation change which can be attributed to surface mass balance processes, rather than ice dynamics.

5.5.1.4 Sea ice

This study presents changes in the position and extent of the Dalton Iceberg Tongue at a high spatial resolution of up to 10 m. However, variations in the quality and coverage of available satellite imagery prevented consistent mapping of sea ice conditions beyond the DIT. The use of a gridded sea ice concentration dataset, such as the AMSR-E and AMSR2 ASI Version 5.4 Sea Ice Concentration 6.25 km product (Melsheimer and Spreen, 2019), would allow a quantitative (but lower spatial resolution) interannual comparison of sea ice distribution adjacent to MUIS. Improved observations of sea ice occurrence further from the ice front would be particularly beneficial, since the location of sea production is suggested to influence ocean circulation and ice shelf melt rates along the Sabrina Coast (Van Achter et al., 2022).

5.5.1.5 Polynya frequency

Analysis of a sea ice concentration dataset, such as the AMSR2 ASI Version 5.4 Sea Ice Concentration product (Melsheimer et al., 2019), could be performed in order to extend the timeseries of Dalton Polynya frequency and location (e.g. Nihashi et al., 2017) since pre-existing observations between 1992 and 2008 (Khazendar et al., 2013). Such a record could be used to provide insight into the relationships between polynya activity, DIT stability and ice shelf thinning.

5.5.2 Recommendations for further work

5.5.2.1 Bed topography and bathymetry

The bed topography beneath MUG remains uncertain (Morlighem et al., 2020). Improvements to the resolution and quality of topographic data would aid identification of potential pinning points within the grounding zone and resolve uncertainties around the origin of inflections on the ice surface. In turn, this would help in assessing the accuracy of

recorded grounding line positions derived via static methods of grounding line detection. Secondly, although high resolution bathymetric surveys exist on the continental shelf close to MUIS (Nitsche et al., 2017), observations adjacent to the ice front would provide further insight into the potential for warm water intrusions into the sub-ice shelf cavity (Silvano et al., 2017).

5.5.2.2 Oceanographic data

Enhanced basal melt rates at MUIS and TIS have been attributed to incursions of warm mCDW from a large reservoir on the continental shelf. This reservoir is expected to expand in the next two centuries, and, in turn, facilitate further ice shelf melting (Rintoul et al., 2016; Silvano et al., 2017, 2019; Jordan et al., in review). Additional oceanographic surveys on the Sabrina Coast would help to quantify the ocean heat flux to the cavity beneath MUIS, as well as assess the processes which control local ocean heat transport in a region affected by complex bathymetry and polynya activity (Silvano et al., 2017).

5.5.2.3 Numerical ice flow modelling

Section 5.2 discusses the stability of MUIS and its capacity to buttress inland flow, suggesting that, to date, topographic features have limited the extent of calving and dynamic change up-ice. However, since warm water intrusions and ice shelf basal melt rates are expected to increase along the Sabrina Coast over the coming century (Sun et al., 2016), it would be beneficial to test the sensitivity of MUG to changes in both MUIS thickness and extent. This analysis could be performed using an ice flow model such as Úa, which has previously been used to estimate the velocity response of outlet glaciers to simulated ice shelf calving and thinning (e.g. Hill et al., 2018, 2021; Miles et al., 2021). Such modelling could help to refine estimates of future sea level contributions from the Moscow catchment (Levermann et al., 2020).

6 Conclusions

This study presents a novel assessment of the recent ice dynamics of Moscow University Glacier and Moscow University Ice Shelf. The Moscow University catchment is located within an area of regional mass loss (Mohajerani et al., 2018) and, due to the presence of warm mCDW proximal to the Sabrina Coast, has been recognised as potentially vulnerable to an ocean-driven increase in ice discharge (Khazendar et al., 2013; Silvano et al., 2017; Stokes et al., 2022). Overall, the results of this thesis indicate that MUG and MUIS remained dynamically stable between the 1990s and 2010, but may have started to exhibit the early indicators of dynamic change during the past decade. This relates specifically to a period of accelerated surface lowering on MUG between 2011 and 2016, which occurred at an average rate of 0.86 ± 0.16 m yr^{-1}. A spatial correlation between regions of faster ice flow and higher rates of surface lowering on MUG implies that the observed thinning is dynamic in origin, and thus plausibly represents a response to the 1.4 ± 0.1 km of width-averaged grounding line retreat recorded for the period 1996 to 2017. However, ice surface velocity on both MUIS and MUG exhibited negligible overall change and underwent only limited fluctuations (average of ± 4%) throughout the observational periods of 2000 – 2021 and 2010 – 2021, respectively. As such, a coupling between the observed accelerated thinning and ice surface velocity remains undetected. For this reason, the recent thinning trend is interpreted as an initial indicator of a potential emerging dynamic instability at MUG, rather than evidence of pervasive dynamic change.

Indeed, when compared to the recent grounding line retreat, acceleration and thinning of neighbouring Totten Glacier (Khazendar et al., 2013; Li et al., 2015, 2016; Greene et al., 2017, 2018; Roberts et al., 2018), the changes observed at MUG are relatively moderate. This thesis suggests that the lower magnitude of change exhibited by MUG and MUIS can be attributed, at least in part, to the topographic confinement of MUIS within a fjord-like embayment. Lateral pinning is suggested to exert critical stresses across the ice shelf, enhancing its stability and thus its capacity to buttress the flow of MUG. This topographic setting is unusual amongst East Antarctic ice shelves. Whilst other Wilkes Land outlet glaciers and ice shelves have calved extensively and accelerated following the removal of landfast sea ice abutting the ice front (Miles et al., 2016, 2017; Greene et al., 2018; Arthur et al., 2021), terminus retreat at MUIS is limited to a ~6.5 km margin within the unconfined shelf region, and ice surface velocity is observed to remain stable during periods of DIT disaggregation and calving. This includes during the austral summer of 2007, when the Porpoise Bay outlet glaciers and Voyeykov Ice Shelf partially disintegrated in coincidence

with a major negative landfast sea ice anomaly (Miles et al., 2017; Arthur et al., 2021). This study therefore emphasises the influence of local topography on ice shelf stability and buttressing capacity. In turn, it is suggested that the response of individual East Antarctic outlet glaciers to ocean forcing can be modulated by their specific topographic setting. Topographically-constrained ice flow modelling consequently presents an important next-step in understanding the vulnerability of the Moscow University catchment to ocean-driven mass loss.

The apparent structural integrity of MUIS implies that melt-induced ice shelf thinning, rather than extensive calving, is the most probable driver of a potential future acceleration in ice discharge from MUG. The rate of basal melt at MUIS is modulated by the activity of the Dalton Polynya, which is associated with sea ice production within the DIT (Khazendar et al., 2013; Silvano et al., 2017; Gwyther et al., 2018). This study observed a sustained reduction in the DIT extent, indicative of a change in local ocean conditions adjacent to the MUIS ice front. By influencing the warmth and volume of mCDW intrusions into the ice shelf cavity (Khazendar et al., 2013; Silvano et al., 2017, 2019; Gwyther et al., 2018), such ocean variability has implications for the rate of ice shelf thinning. It is recommended that future glaciological observations of MUIS and MUG are considered alongside oceanographic conditions.

In combination, these findings highlight the need for the continued monitoring of ice dynamics at MUIS and MUG. Accurate additional measurements of ice surface velocity and grounding line retreat at MUG are particularly important in the context of observed thinning, and would help to resolve differences between the findings of this thesis and those of Li et al. (2022a). To date, the Moscow University catchment appears less sensitive to ocean forcing than neighbouring Wilkes Land outlet glaciers. However, a period of accelerated thinning may represent the precursor to dynamic change at MUG in the near future, with implications for mass loss from the Aurora Subglacial Basin.

References

Abram, N.J., Mulvaney, R., Vimeux, F., Phipps, S.J., Turner, J. and England, M.H. (2014) 'Evolution of the Southern Annular Mode during the past millennium', *Nature Climate Change*, 4(7), pp. 564–569.

Adusumilli, S., Fricker, H.A., Medley, B., Padman, L. and Siegfried, M.R. (2020) 'Interannual variations in meltwater input to the Southern Ocean from Antarctic ice shelves', *Nature Geoscience*, 13(9), pp. 616–620.

Agosta, C., Amory, C., Kittel, C., Orsi, A., Favier, V., Gallée, H., van den Broeke, M.R., Lenaerts, J.T.M., van Wessem, J.M., van de Berg, W.J. and Fettweis, X. (2019) 'Estimation of the Antarctic surface mass balance using the regional climate model MAR (1979–2015) and identification of dominant processes', *The Cryosphere*, 13(1), pp. 281–296.

Aitken, A.R.A., Roberts, J.L., Ommen, T.D. van, Young, D.A., Golledge, N.R., Greenbaum, J.S., Blankenship, D.D. and Siegert, M.J. (2016) 'Repeated large-scale retreat and advance of Totten Glacier indicated by inland bed erosion', *Nature*, 533(7603), pp. 385–389.

Åkesson, H., Nisancioglu, K.H. and Nick, F.M. (2018) 'Impact of Fjord Geometry on Grounding Line Stability', *Frontiers in Earth Science*, 6, pp. 16.

Anderson, J.B., Simkins, L.M., Bart, P.J., De Santis, L., Halberstadt, A.R.W., Olivo, E. and Greenwood, S.L. (2019) 'Seismic and geomorphic records of Antarctic Ice Sheet evolution in the Ross Sea and controlling factors in its behaviour', *Geological Society, London, Special Publications*, 475(1), pp. 223–240.

Armstrong McKay, D.I., Staal, A., Abrams, J.F., Winkelmann, R., Sakschewski, B., Loriani, S., Fetzer, I., Cornell, S.E., Rockström, J. and Lenton, T.M. (2022) 'Exceeding 1.5°C global warming could trigger multiple climate tipping points', *Science*, 377(6611), pp. eabn7950.

Arndt, J.E., Schenke, H.W., Jakobsson, M., Nitsche, F.O., Buys, G., Goleby, B., Rebesco, M., Bohoyo, F., Hong, J., Black, J., Greku, R., Udintsev, G., Barrios, F., Reynoso-Peralta, W., Taisei, M. and Wigley, R. (2013) 'The International Bathymetric Chart of the Southern Ocean (IBCSO) Version 1.0—A new bathymetric compilation covering circum-Antarctic waters', *Geophysical Research Letters*, 40(12), pp. 3111–3117.

Arthur, J.F., Stokes, C.R., Jamieson, S.S.R., Miles, B.W.J., Carr, J.R. and Leeson, A.A. (2021) 'The triggers of the disaggregation of Voyeykov Ice Shelf (2007), Wilkes Land, East Antarctica, and its subsequent evolution', *Journal of Glaciology*, 67(265), pp. 933–951.

Aschwanden, A., Bartholomaus, T.C., Brinkerhoff, D.J. and Truffer, M. (2021) 'Brief communication: A roadmap towards credible projections of ice sheet contribution to sea level', *The Cryosphere*, 15(12), pp. 5705–5715.

Badger, M.P.S., Lear, C.H., Pancost, R.D., Foster, G.L., Bailey, T.R., Leng, M.J. and Abels, H.A. (2013) 'CO_2 drawdown following the middle Miocene expansion of the Antarctic Ice Sheet', *Paleoceanography*, 28(1), pp. 42–53.

Bamber, J.L., Westaway, R.M., Marzeion, B. and Wouters, B. (2018) 'The land ice contribution to sea level during the satellite era', *Environmental Research Letters*, 13(6), pp. 063008.

Banwell, A.F. and Macayeal, D.R. (2015) 'Ice-shelf fracture due to viscoelastic flexure stress induced by fill/drain cycles of supraglacial lakes', *Antarctic Science*, 27(6), pp. 587–597.

Banwell, A.F., MacAyeal, D.R. and Sergienko, O.V. (2013) 'Breakup of the Larsen B Ice Shelf triggered by chain reaction drainage of supraglacial lakes', *Geophysical Research Letters*, 40(22), pp. 5872–5876.

Baumhoer, C., Dietz, A., Dech, S. and Kuenzer, C. (2018) 'Remote Sensing of Antarctic Glacier and Ice-Shelf Front Dynamics – A Review', *Remote Sensing*, 10(9), pp. 1445.

Bell, R.E., Banwell, A.F., Trusel, L.D. and Kingslake, J. (2018) 'Antarctic surface hydrology and impacts on ice-sheet mass balance', *Nature Climate Change*, 8(12), pp. 1044–1052.

Benn, D.I., Warren, C.R. and Mottram, R.H. (2007) 'Calving processes and the dynamics of calving glaciers', *Earth-Science Reviews*, 82(3-4), pp. 143–179.

Bensi, M., Kovačević, V., Donda, F., O'Brien, P.E., Armbrecht, L. and Armand, L. (2022) 'Water masses distribution offshore the Sabrina Coast (East Antarctica)', *Earth Syst. Sci. Data*, 14, pp. 65–78.

Berthier, E., Scambos, T.A. and Shuman, C.A. (2012) 'Mass loss of Larsen B tributary glaciers (Antarctic Peninsula) unabated since 2002', *Geophysical Research Letters*, 39(13), pp. L13501.

Bevan, S.L., Luckman, A.J. and Murray, T. (2012) 'Glacier dynamics over the last quarter of a century at Helheim, Kangerdlugssuaq and 14 other major Greenland outlet glaciers', *The Cryosphere*, 6(5), pp. 923–937.

Bindschadler, R. and Choi, H. (2011) 'High-resolution Image-derived Grounding and Hydrostatic Lines for the Antarctic Ice Sheet', U.S. Antarctic Program (USAP) Data Center. DOI:10.7265/N56T0JK2. [Date Accessed: 01/04/22].

Bindschadler, R., Choi, H., Wichlacz, A., Bingham, R., Bohlander, J., Brunt, K., Corr, H., Drews, R., Fricker, H., Hall, M., Hindmarsh, R., Kohler, J., Padman, L., Rack, W., Rotschky, G., Urbini, S., Vornberger, P. and Young, N. (2011) 'Getting around Antarctica: new high-resolution mappings of the grounded and freely-floating boundaries of the Antarctic ice sheet created for the International Polar Year', *The Cryosphere*, 5(3), pp. 569-588.

Bindschadler, R., Vornberger, P., Fleming, A., Fox, A., Mullins, J., Binnie, D., Paulsen, S., Granneman, B. and Gorodetzky, D. (2008) 'The Landsat Image Mosaic of Antarctica', *Remote Sensing of Environment*, 112(12), pp. 4214–4226.

Blackburn, T., Edwards, G.H., Tulaczyk, S., Scudder, M., Piccione, G., Hallet, B., McLean, N., Zachos, J.C., Cheney, B. and Babbe, J.T. (2020) 'Ice retreat in Wilkes Basin

of East Antarctica during a warm interglacial', *Nature*, 583(7817), pp. 554–559.

Boening, C., Lebsock, M., Landerer, F. and Stephens, G. (2012) 'Snowfall-driven mass change on the East Antarctic ice sheet', *Geophysical Research Letters*, 39(21), L21501.

Bradley, S.L., Siddall, M., Milne, G.A., Masson-Delmotte, V. and Wolff, E. (2013) 'Combining ice core records and ice sheet models to explore the evolution of the East Antarctic Ice sheet during the Last Interglacial period', *Global and Planetary Change*, 100, pp. 278–290.

Brancato, V., Rignot, E., Milillo, P., Morlighem, M., Mouginot, J., An, L., Scheuchl, B., Jeong, S., Rizzoli, P., Bueso Bello, J.L. and Prats-Iraola, P. (2020) 'Grounding Line Retreat of Denman Glacier, East Antarctica, Measured With COSMO-SkyMed Radar Interferometry Data', *Geophysical Research Letters*, 47(7), pp. e2019GL086291.

Briggs, K.H., Shepherd, A., Hogg, A.E., Ivins, E., Schlegel, N., Joughin, I., Smith, B., Krinner, G., Moyano, G., Nowicki, S., Payne, T.J., Rignot, E., Velicogna, I., Scambos, T., van den Broeke, M.R., and Whitehouse, P.L. (2016) 'Charting ice sheet contributions to global sea level rise', *EOS,* 97.

Bronselaer, B., Winton, M., Griffies, S.M., Hurlin, W.J., Rodgers, K.B., Sergienko, O.V., Stouffer, R.J. and Russell, J.L. (2018) 'Change in future climate due to Antarctic meltwater', *Nature*, 564(7734), pp. 53–58.

Brunt, K.M., Fricker, H.A., Padman, L., Scambos, T.A. and O'Neel, S. (2010) 'Mapping the grounding zone of the Ross Ice Shelf, Antarctica, using ICESat laser altimetry', *Annals of Glaciology*, 51(55), pp. 71–79.

Carlson, A.E. and Winsor, K. (2012) 'Northern Hemisphere ice-sheet responses to past climate warming', *Nature Geoscience*, 5(9), pp. 607–613.

Chen, J., Ke, C., Zhou, X., Shao, Z. and Li, L. (2016) 'Surface velocity estimations of ice shelves in the northern Antarctic Peninsula derived from MODIS data', *Journal of Geographical Sciences*, 26(2), pp. 243–256.

Chen, J.L., Wilson, C.R., Blankenship, D. and Tapley, B.D. (2009) 'Accelerated Antarctic ice loss from satellite gravity measurements', *Nature Geoscience*, 2(12), pp. 859–862.

Christie, F.D.W., Bingham, R.G., Gourmelen, N., Tett, S.F.B. and Muto, A. (2016) 'Four-decade record of pervasive grounding line retreat along the Bellingshausen margin of West Antarctica', *Geophysical Research Letters*, 43(11), pp. 5741–5749.

Chuter, S.J., Martín-Español, A., Wouters, B. and Bamber, J.L. (2017) 'Mass balance reassessment of glaciers draining into the Abbot and Getz Ice Shelves of West Antarctica', *Geophysical Research Letters*, 44(14), pp. 7328–7337.

Cook, A.J. and Vaughan, D.G. (2010) 'Overview of areal changes of the ice shelves on the Antarctic Peninsula over the past 50 years', *The Cryosphere*, 4, pp. 77–98.

Cook, A.J., Fox, A.J., Vaughan, D.G. and Ferrigno, J.G. (2005) 'Retreating Glacier Fronts on the Antarctic Peninsula over the Past Half-Century', *Science*, 308(5721), pp. 541–544.

Cook, A.J., Holland, P.R., Meredith, M.P., Murray, T., Luckman, A. and Vaughan, D.G. (2016) 'Ocean forcing of glacier retreat in the western Antarctic Peninsula', *Science*, 353(6296), pp. 283–286.

Cook, C.P., van de Flierdt, T., Williams, T., Hemming, S.R., Iwai, M., Kobayashi, M., Jimenez-Espejo, F.J., Escutia, C., González, J.J., Khim, B.-K., McKay, R.M., Passchier, S., Bohaty, S.M., Riesselman, C.R., Tauxe, L., Sugisaki, S., Galindo, A.L., Patterson, M.O., Sangiorgi, F., Pierce, E.L., Brinkhuis, H., Klaus, A., Fehr, A., Bendle, J.A.P., Bijl, P.K., Carr, S.A., Dunbar, R.B., Flores, J.A., Hayden, T.G., Katsuki, K., Kong, G.S., Nakai, M., Olney, M.P., Pekar, S.F., Pross, J., Röhl, U., Sakai, T., Shrivastava, P.K., Stickley, C.E., Tuo, S., Welsh, K. and Yamane, M. (2013) 'Dynamic behaviour of the East Antarctic ice sheet during Pliocene warmth', *Nature Geoscience*, 6(9), pp. 765–769.

Crotti, I., Quiquet, A., Landais, A., Stenni, B., Wilson, D.J., Severi, M., Mulvaney, R., Wilhelms, F., Barbante, C. and Frezzotti, M. (2022) 'Wilkes subglacial basin ice sheet response to Southern Ocean warming during late Pleistocene interglacials', *Nature Communications*, 13(1), pp. 5328.

Davies, B.J., Carrivick, J.L., Glasser, N.F., Hambrey, M.J. and Smellie, J.L. (2012) 'Variable glacier response to atmospheric warming, northern Antarctic Peninsula, 1988–2009', *The Cryosphere*, 6(5), pp. 1031–1048.

Davis, C. H., Li, Y., McConnell, J. R., Frey, M. M. and Hanna, E. (2005) 'Snowfall-driven growth in East Antarctic Ice Sheet mitigates recent sea-level rise', *Science*, 308, pp. 1898–1901.

De Rydt, J., Gudmundsson, G.H., Rott, H. and Bamber, J.L. (2015) 'Modeling the instantaneous response of glaciers after the collapse of the Larsen B Ice Shelf', *Geophysical Research Letters*, 42(13), pp. 5355–5363.

DeBeer, C.M. and Sharp, M.J. (2007) 'Recent changes in glacier area and volume within the southern Canadian Cordillera', *Annals of Glaciology*, 46, pp. 215-221.

DeConto, R.M. and Pollard, D. (2016) 'Contribution of Antarctica to past and future sea-level rise', *Nature*, 531(7596), pp. 591–597.

DeConto, R.M., Pollard, D., Alley, R.B., Velicogna, I., Gasson, E., Gomez, N., Sadai, S., Condron, A., Gilford, D.M., Ashe, E.L., Kopp, R.E., Li, D. and Dutton, A. (2021) 'The Paris Climate Agreement and future sea-level rise from Antarctica', *Nature*, 593(7857), pp. 83–89.

Denton, G.H., Sugden, D.E., Marchant, D.R., Hall, B.L. and Wilch, T.I. (1993) 'East Antarctic Ice Sheet Sensitivity to Pliocene Climatic Change from a Dry Valleys Perspective', *Geografiska Annaler: Series A, Physical Geography*, 75(4), pp. 155–204.

Depoorter, M.A., Bamber, J.L., Griggs, J.A., Lenaerts, J.T.M., Ligtenberg, S.R.M., van den Broeke, M.R. and Moholdt, G. (2013) 'Calving fluxes and basal melt rates of Antarctic ice shelves', *Nature*, 502(7469), pp. 89–92.

Diener, T., Sasgen, I., Agosta, C., Fürst, J.J., Braun, M.H., Konrad, H. and Fettweis, X.

(2021) ‘Acceleration of Dynamic Ice Loss in Antarctica From Satellite Gravimetry’, *Frontiers in Earth Science*, 9, pp. 741789.

DLR (Deutsches Zentrum für Luft- und Raumfahrt), German Aerospace Center (2021) ‘Grounding line for key glaciers, Antarctica, derived from ERS-1/2, TerraSAR-X and Copernicus Sentinel-1 data acquired in 1994-2021. 2021-03-10, v2.0’. Available at: http://cryoportal.enveo.at/data/. [Date Accessed: 10/04/22].

Dow, C.F., Lee, W.S., Greenbaum, J.S., Greene, C.A., Blankenship, D.D., Poinar, K., Forrest, A.L., Young, D.A. and Zappa, C.J. (2018) ‘Basal channels drive active surface hydrology and transverse ice shelf fracture’, *Science Advances*, 4(6), pp. eaao7212.

Downes, S.M. and Hogg, A.McC. (2013) ‘Southern Ocean Circulation and Eddy Compensation in CMIP5 Models’, *Journal of Climate*, 26(18), pp. 7198–7220.

Dupont, T.K. and Alley, R.B. (2005) ‘Assessment of the importance of ice-shelf buttressing to ice-sheet flow’, *Geophysical Research Letters*, 32(4), L04503.

Dutton, A., Carlson, A.E., Long, A.J., Milne, G.A., Clark, P.U., DeConto, R., Horton, B.P., Restore, S. and Raymo, M.E. (2015) ‘Sea-level rise due to polar ice-sheet mass loss during past warm periods’, *Science*, 349(6244), pp. 153–153.

Edwards, T.L., Nowicki, S., Marzeion, B., Hock, R., Goelzer, H., Seroussi, H., Jourdain, N.C., Slater, D.A., Turner, F.E., Smith, C.J., McKenna, C.M., Simon, E., Abe-Ouchi, A., Gregory, J.M., Larour, E., Lipscomb, W.H., Payne, A.J., Shepherd, A., Agosta, C., Alexander, P., Albrecht, T., Anderson, B., Asay-Davis, X., Aschwanden, A., Barthel, A., Bliss, A., Calov, R., Chambers, C., Champollion, N., Choi, Y., Cullather, R., Cuzzone, J., Dumas, C., Felikson, D., Fettweis, X., Fujita, K., Galton-Fenzi, B.K., Gladstone, R., Golledge, N.R., Greve, R., Hattermann, T., Hoffman, M.J., Humbert, A., Huss, M., Huybrechts, P., Immerzeel, W., Kleiner, T., Kraaijenbrink, P., Le clec’h, S., Lee, V., Leguy, G.R., Little, C.M., Lowry, D.P., Malles, J.-H., Martin, D.F., Maussion, F., Morlighem, M., O’Neill, J.F., Nias, I., Pattyn, F., Pelle, T., Price, S.F., Quiquet, A., Radić, V., Reese, R., Rounce, D.R., Rückamp, M., Sakai, A., Shafer, C., Schlegel, N.-J., Shannon, S., Smith, R.S., Straneo, F., Sun, S., Tarasov, L., Trusel, L.D., Van Breedam, J., van de Wal, R., van den Broeke, M., Winkelmann, R., Zekollari, H., Zhao, C., Zhang, T. and Zwinger, T. (2021) ‘Projected land ice contributions to twenty-first-century sea level rise’, *Nature*, 593(7857), pp. 74–82.

ENVEO Environmental Earth Observation IT GmbH (2022) ‘Antarctic Ice Sheet monthly ice velocity – 2019, 2020, 2021’. Available at: http://cryoportal.enveo.at/data/. [Date Accessed: 25/05/22].

Etourneau, J., Sgubin, G., Crosta, X., Swingedouw, D., Willmott, V., Barbara, L., Houssais, M.-N., Schouten, S., Damsté, J.S.S., Goosse, H., Escutia, C., Crespin, J., Massé, G. and Kim, J.-H. (2019) ‘Ocean temperature impact on ice shelf extent in the eastern Antarctic Peninsula’, *Nature Communications*, 10(1), pp. 304.

Fahnestock, M.A., Abdalati, W. and Shuman, C. (2002) ‘Long melt seasons on ice shelves of the Antarctic Peninsula: An analysis using satellite-based microwave emission measurements’, *Annals of Glaciology*, 34, pp. 127–133.

Favier, L., Durand, G., Cornford, S.L., Gudmundsson, G.H., Gagliardini, O., Gillet-Chaulet, F., Zwinger, T., Payne, A.J. and Le Brocq, A.M. (2014) 'Retreat of Pine Island Glacier controlled by marine ice-sheet instability', *Nature Climate Change*, 4(2), pp. 117–121.

Feldmann, J. and Levermann, A. (2015) 'Collapse of the West Antarctic Ice Sheet after local destabilization of the Amundsen Basin', *Proceedings of the National Academy of Sciences*, 112(46), pp. 14191–14196.

Fettweis, X., Hanna, E., Lang, C., Belleflamme, A., Erpicum, M. and Gallée, H. (2013) 'Brief communication: Important role of the mid-tropospheric atmospheric circulation in the recent surface melt increase over the Greenland ice sheet', *The Cryosphere*, 7(1), pp. 241–248.

Fraser, A.D., Massom, R.A., Handcock, M.S., Reid, P., Ohshima, K.I., Raphael, M.N., Cartwright, J., Klekociuk, A.R., Wang, Z. and Porter-Smith, R. (2021) 'Eighteen-year record of circum-Antarctic landfast-sea-ice distribution allows detailed baseline characterisation and reveals trends and variability', *The Cryosphere*, 15(11), pp. 5061–5077.

Fraser, A.D., Massom, R.A., Ohshima, K.I., Willmes, S., Kappes, P.J., Cartwright, J. and Porter-Smith, R. (2020) 'High-resolution mapping of circum-Antarctic landfast sea ice distribution, 2000–2018', *Earth System Science Data*, 12(4), pp. 2987–2999.

Fretwell, P., Pritchard, H.D., Vaughan, D.G., Bamber, J.L., Barrand, N.E., Bell, R., Bianchi, C., Bingham, R.G., Blankenship, D.D., Casassa, G., Catania, G., Callens, D., Conway, H., Cook, A.J., Corr, H.F.J., Damaske, D., Damm, V., Ferraccioli, F., Forsberg, R., Fujita, S., Gim, Y., Gogineni, P., Griggs, J.A., Hindmarsh, R.C.A., Holmlund, P., Holt, J.W., Jacobel, R.W., Jenkins, A., Jokat, W., Jordan, T., King, E.C., Kohler, J., Krabill, W., Riger-Kusk, M., Langley, K.A., Leitchenkov, G., Leuschen, C., Luyendyk, B.P., Matsuoka, K., Mouginot, J., Nitsche, F.O., Nogi, Y., Nost, O.A., Popov, S.V., Rignot, E., Rippin, D.M., Rivera, A., Roberts, J., Ross, N., Siegert, M.J., Smith, A.M., Steinhage, D., Studinger, M., Sun, B., Tinto, B.K., Welch, B.C., Wilson, D., Young, D.A., Xiangbin, C. and Zirizzotti, A. (2013) 'Bedmap2: improved ice bed, surface and thickness datasets for Antarctica', *The Cryosphere*, 7(1), pp. 375–393. Fahnestock, M.A., Abdalati, W. and Shuman, C.A. (2002) 'Long melt seasons on ice shelves of the Antarctic Peninsula: an analysis using satellite-based microwave emission measurements', *Annals of Glaciology*, 34, pp. 127–133.

Fricker, H.A. and Padman, L. (2006) 'Ice shelf grounding zone structure from ICESat laser altimetry', *Geophysical Research Letters*, 33(15), L15502.

Fricker, H.A., Coleman, R., Padman, L., Scambos, T.A., Bohlander, J. and Brunt, K.M. (2009) 'Mapping the grounding zone of the Amery Ice Shelf, East Antarctica using InSAR, MODIS and ICESat', *Antarctic Science*, 21(5), pp. 515–532.

Friedl, P., Weiser, F., Fluhrer, A. and Braun, M.H. (2020) 'Remote sensing of glacier and ice sheet grounding lines: A review', *Earth-Science Reviews*, 201, pp. 102948.

Fürst, J. J., Durand, G., Gillet-Chaulet, F., Tavard, L., Rankl, M., Braun, M. and

Gagliardini, O. (2016) 'The safety band of Antarctic ice shelves', *Nature Climate Change*, 6(5), pp. 479–482.

Gagliardini, O., Durand, G., Zwinger, T., Hindmarsh, R.C.A. and Le Meur, E. (2010) 'Coupling of ice-shelf melting and buttressing is a key process in ice-sheets dynamics', *Geophysical Research Letters*, 37(14).

Gardner, A.S., Fahnestock, M.A., and Scambos, T.A. (2019a) 'ITS_LIVE Regional Glacier and Ice Sheet Surface Velocities'. Data archived at National Snow and Ice Data Center. DOI:10.5067/6II6VW8LLWJ7. [Date accessed: 01/02/2022].

Gardner, A.S., Fahnestock, M.A., and Scambos, T.A. (2019b) 'MEaSUREs ITS_LIVE Landsat Image-Pair Glacier and Ice Sheet Surface Velocities: Version 1', Data archived at National Snow and Ice Data Center. DOI:10.5067/IMR9D3PEI28U. [Date accessed: 01/02/2022].

Gardner, A.S., Moholdt, G., Scambos, T., Fahnstock, M., Ligtenberg, S., van den Broeke, M., and Nilsson, J. (2018) 'Increased West Antarctic and unchanged East Antarctic ice discharge over the last 7 years', *The Cryosphere*, 12(2), pp. 521–547.

Gasson, E., DeConto, R.M., Pollard, D. and Levy, R.H. (2016) 'Dynamic Antarctic ice sheet during the early to mid-Miocene', *Proceedings of the National Academy of Sciences*, 113(13), pp. 3459–3464.

Glasser, N.F. and Scambos, T.A. (2008) 'A structural glaciological analysis of the 2002 Larsen B ice-shelf collapse', *Journal of Glaciology*, 54(184), pp. 3–16.

Glasser, N.F., Scambos, T.A., Bohlander, J., Truffer, M., Pettit, E. and Davies, B.J. (2011) 'From ice-shelf tributary to tidewater glacier: continued rapid recession, acceleration and thinning of Röhss Glacier following the 1995 collapse of the Prince Gustav Ice Shelf, Antarctic Peninsula', *Journal of Glaciology*, 57(203), pp. 397–406.

Gohl, K., Uenzelmann-Neben, G., Gille-Petzoldt, J., Hillenbrand, C.-D., Klages, J.P., Bohaty, S.M., Passchier, S., Frederichs, T., Wellner, J.S., Lamb, R., Leitchenkov, G. and Scientists, I.E. 379 (2021) 'Evidence for a Highly Dynamic West Antarctic Ice Sheet During the Pliocene', *Geophysical Research Letters*, 48(14), pp. e2021GL093103.

Golledge, N.R., Kowalewski, D.E., Naish, T.R., Levy, R.H., Fogwill, C.J. and Gasson, E.G.W. (2015) 'The multi-millennial Antarctic commitment to future sea-level rise', *Nature*, 526(7573), pp. 421–425.

Golledge, N.R., Thomas, Z.A., Levy, R.H., Gasson, E.G.W., Naish, T.R., McKay, R.M., Kowalewski, D.E. and Fogwill, C.J. (2017) 'Antarctic climate and ice-sheet configuration during the early Pliocene interglacial at 4.23 Ma', *Climate of the Past*, 13(7), pp. 959–975.

Grant, G.R., Naish, T.R., Dunbar, G.B., Stocchi, P., Kominz, M.A., Kamp, P.J.J., Tapia, C.A., McKay, R.M., Levy, R.H. and Patterson, M.O. (2019) 'The amplitude and origin of sea-level variability during the Pliocene epoch', *Nature*, 574(7777), pp. 237–241.

Greenbaum, J.S., Blankenship, D.D., Young, D.A., Richter, T.G., Roberts, J.L., Aitken, A.R.A., Legresy, B., Schroeder, D.M., Warner, R.C., van Ommen, T.D. and Siegert, M.J.

(2015) ‘Ocean access to a cavity beneath Totten Glacier in East Antarctica’, *Nature Geoscience*, 8(4), pp. 294–298.

Greene, C.A., Blankenship, D.D., Gwyther, D.E., Silvano, A. and van Wijk, E. (2017) ‘Wind causes Totten Ice Shelf melt and acceleration’, *Science Advances*, 3(11), pp. e1701681.

Greene, C.A., Gardner, A.S., Schlegel, N.-J. and Fraser, A.D. (2022) ‘Antarctic calving loss rivals ice-shelf thinning’, *Nature*, 609(7929), pp. 948–953.

Greene, C.A., Young, D.A., Gwyther, D.E., Galton-Fenzi, B.K. and Blankenship, D.D. (2018) ‘Seasonal dynamics of Totten Ice Shelf controlled by sea ice buttressing’, *The Cryosphere*, 12(9), pp. 2869-2882.

Gudmundsson, G.H. (2013) ‘Ice-shelf buttressing and the stability of marine ice sheets’, *The Cryosphere*, 7(2), pp. 647–655.

Gudmundsson, G.H., Paolo, F.S., Adusumilli, S. and Fricker, H.A. (2019) ‘Instantaneous Antarctic ice sheet mass loss driven by thinning ice shelves’, *Geophysical Research Letters*, 46(23), pp. 13903–13909.

Gudmundsson, G.H., Paolo, F.S., Adusumilli, S. and Fricker, H.A. (2019) ‘Instantaneous Antarctic ice sheet mass loss driven by thinning ice shelves’, *Geophysical Research Letters*, 46(23), pp. 13903–13909.

Gulick, S.P.S., Shevenell, A.E., Montelli, A., Fernandez, R., Smith, C., Warny, S., Bohaty, S.M., Sjunneskog, C., Leventer, A., Frederick, B. and Blankenship, D.D. (2017) ‘Initiation and long-term instability of the East Antarctic Ice Sheet’, *Nature*, 552(7684), pp. 225–229.

Gwyther, D.E., Galton-Fenzi, B.K., Hunter, J.R. and Roberts, J.L. (2014) ‘Simulated melt rates for the Totten and Dalton ice shelves’, *Ocean Science*, 10(3), pp. 267–279.

Gwyther, D.E., O’Kane, T.J., Galton-Fenzi, B.K., Monselesan, D.P. and Greenbaum, J.S. (2018) ‘Intrinsic processes drive variability in basal melting of the Totten Glacier Ice Shelf’, *Nature Communications*, 9(1), pp. 3141.

Hanna, E., Mernild, S.H., Cappelen, J. and Steffen, K. (2012) ‘Recent warming in Greenland in a long-term instrumental (1881–2012) climatic context: I. Evaluation of surface air temperature records’, *Environmental Research Letters*, 7(4), pp. 045404.

Hanna, E., Navarro, F.J., Pattyn, F., Domingues, C.M., Fettweis, X., Ivins, E.R., Nicholls, R.J., Ritz, C., Smith, B., Tulaczyk, S., Whitehouse, P.L. and Zwally, H.J. (2013) ‘Ice-sheet mass balance and climate change’, *Nature*, 498(7452), pp. 51–59.

Hanna, E., Pattyn, F., Navarro, F., Favier, V., Goelzer, H., van den Broeke, M.R., Vizcaino, M., Whitehouse, P.L., Ritz, C., Bulthuis, K. and Smith, B. (2020) ‘Mass balance of the ice sheets and glaciers – Progress since AR5 and challenges’, *Earth-Science Reviews*, 201, pp. 102976.

Haran, T., Klinger, M., Bohlander, J., Fahnestock, M., Painter, T., and Scambos, T.

(2018). MEaSUREs MODIS Mosaic of Antarctica 2013-2014 (MOA2014) Image Map, Version 1 [Data Set]. Boulder, Colorado USA. NASA National Snow and Ice Data Center Distributed Active Archive Center. DOI: https://doi.org/10.5067/RNF17BP824UM.

Harig, C. and Simons, F.J. (2015) 'Accelerated West Antarctic ice mass loss continues to outpace East Antarctic gains', *Earth and Planetary Science Letters*, 415, pp. 134–141.

Harwood, D.M. and Webb, P.N. (1998) 'Glacial transport of diatoms in the Antarctic Sirius Group: Pliocene refrigerator', *GSA Today*, 8(4), pp. 1–8.

Haywood, A.M., Hill, D.J., Dolan, A.M., Otto-Bliesner, B.L., Bragg, F., Chan, W.-L., Chandler, M.A., Contoux, C., Dowsett, H.J., Jost, A., Kamae, Y., Lohmann, G., Lunt, D.J., Abe-Ouchi, A., Pickering, S.J., Ramstein, G., Rosenbloom, N.A., Salzmann, U., Sohl, L., Stepanek, C., Ueda, H., Yan, Q. and Zhang, Z. (2013) 'Large-scale features of Pliocene climate: results from the Pliocene Model Intercomparison Project', *Climate of the Past*, 9(1), pp. 191–209.

Herraiz-Borreguero, L. and Naveira Garabato, A.C. (2022) 'Poleward shift of Circumpolar Deep Water threatens the East Antarctic Ice Sheet', *Nature Climate Change*, 12(8), pp. 728–734.

Hill, E.A., Gudmundsson, G.H., Carr, J.R. and Stokes, C.R. (2018) 'Velocity response of Petermann Glacier, northwest Greenland, to past and future calving events', *The Cryosphere*, 12(12), pp. 3907–3921.

Hill, E.A., Gudmundsson, G.H., Carr, J.R., Stokes, C.R. and King, H.M. (2021) 'Twenty-first century response of Petermann Glacier, northwest Greenland to ice shelf loss', *Journal of Glaciology*, 67(261), pp. 147–157.

Hirano, D., Mizobata, K., Sasaki, H., Murase, H., Tamura, T. and Aoki, S. (2021) 'Poleward eddy-induced warm water transport across a shelf break off Totten Ice Shelf, East Antarctica', *Communications Earth & Environment*, 2(1), 153.

Hogg, A.E., Gilbert, L., Shepherd, A., Muir, A.S. and McMillan, M. (2021) 'Extending the record of Antarctic ice shelf thickness change, from 1992 to 2017', *Advances in Space Research*, 68(2), pp. 724–731.

Holland, P. R., Bracegirdle, T. J., Dutrieux, P., Jenkins, A., & Steig, E. J. (2019) 'West Antarctic ice loss influenced by internal climate variability and anthropogenic forcing', *Nature Geoscience,* 12(9), pp. 718–724.

Holt, T.O., Glasser, N.F., Quincey, D.J. and Siegfried, M.R. (2013) 'Speedup and fracturing of George VI Ice Shelf, Antarctic Peninsula', *The Cryosphere*, 7(3), pp. 797–816.

Howat, I.M., Porter, C., Smith, B.E., Noh, M.J., and Morin, P. (2019) 'The Reference Elevation Model of Antarctica', *The Cryosphere*, 13, pp. 665–674.

Hughes, T. (1975) 'The West Antarctic Ice Sheet: Instability, disintegration, and initiation of Ice Ages', *Reviews of Geophysics*, 13(4), pp. 502–526.

Hughes, T.J. (1981) 'The weak underbelly of the West Antarctic Ice Sheet', *Journal of*

Glaciology, 27, pp. 518–525.

Hulbe, C.L., Scambos, T.A., Youngberg, T., and Lamb, A.K. (2008) 'Patterns of glacier response to disintegration of the Larsen B ice shelf, Antarctic Peninsula', *Global Planet Change*, 63, pp. 1–8.

Jacobs, S.S., Jenkins, A., Giulivi, C.F., and Dutrieux, P. (2011) 'Stronger ocean circulation and increased melting under Pine Island Glacier ice shelf', *Nature Geoscience*, 4, 519–523.

Jamieson, S.S.R., Vieli, A., Cofaigh, C.Ó., Stokes, C.R., Livingstone, S.J. and Hillenbrand, C.-D. (2014) 'Understanding controls on rapid ice-stream retreat during the last deglaciation of Marguerite Bay, Antarctica, using a numerical model', *Journal of Geophysical Research: Earth Surface*, 119(2), pp. 247–263.

Jenkins, A., Shoosmith, D., Dutrieux, P., Jacobs, S., Kim, T.W., Lee, S.H., Ha, H.K. and Stammerjohn, S. (2018) 'West Antarctic Ice Sheet retreat in the Amundsen Sea driven by decadal oceanic variability', *Nature Geoscience*, 11(10), pp. 733–738.

Jezek, K.C., Curlander, J.C., Carsey, F., Wales, C. and Barry., R.G. (2013) 'RAMP AMM-1 SAR Image Mosaic of Antarctica, Version 2'. Boulder, Colorado USA. NASA National Snow and Ice Data Center Distributed Active Archive Center. DOI:10.5067/8AF4ZRPULS4H. [Date Accessed: 15/11/21].

John, C.M., Karner, G.D., Browning, E., Leckie, R.M., Mateo, Z., Carson, B. and Lowery, C. (2011) 'Timing and magnitude of Miocene eustasy derived from the mixed siliciclastic-carbonate stratigraphic record of the northeastern Australian margin', *Earth and Planetary Science Letters*, 304(3–4), pp. 455–467.

Jordan, J.R., Miles, B.W.J., Gudmundsson, G.H., Jamieson, S.S.R, Jenkins, A., Stokes, C.R. (in review) 'Increased warm water intrusions could cause future East Antarctic mass loss within the next 100 years', *Nature Communications*.

Joughin, I. and Alley, R.B. (2011) 'Stability of the West Antarctic ice sheet in a warming world', *Nature Geoscience*, 4(8), pp. 506–513.

Joughin, I., Alley, R.B. and Holland, D.M. (2012) 'Ice-Sheet Response to Oceanic Forcing', *Science*, 338(6111), pp. 1172–1176.

Joughin, I., Gray, L., Bindschadler, R., Price, S., Morse, D., Hulbe, C., Mattar, K. and Werner, C. (1999) 'Tributaries of West Antarctic Ice Streams Revealed by RADARSAT Interferometry', *Science*, 286(5438), pp. 283–286.

Joughin, I., Smith, B.E. and Medley, B. (2014) 'Marine Ice Sheet Collapse Potentially Under Way for the Thwaites Glacier Basin, West Antarctica', *Science*, 344(6185), pp. 735–738.

Jouzel J., Masson-Delmotte V., Cattani O., Dreyfus G., Falourd S., Hoffmann G., Minster B., Nouet J., Barnola J. M., Chappellaz J., Fischer H., Gallet J. C., Johnsen S., Leuenberger M., Loulergue L., Luethi D., Oerter H., Parrenin F., Raisbeck G., Raynaud D., Schilt A., Schwander J., Selmo E., Souchez R., Spahni R., Stauffer B., Steffensen

J. P., Stenni B., Stocker T. F., Tison J. L., Werner M., Wolff E. W. (2007) 'Orbital and millennial Antarctic climate variability over the past 800,000 years', *Science*, 317, pp. 793–796.

Kellogg, D.E. and Kellogg, T.B. (1996) 'Diatoms in South Pole ice: Implications for eolian contamination of Sirius Group deposit', *Geology*, 24, pp. 115–118.

Kennett, J.P. (1977) 'Cenozoic evolution of Antarctic glaciation, the circum-Antarctic Ocean, and their impact on global paleoceanography', *Journal of Geophysical Research (1896-1977)*, 82(27), pp. 3843–3860.

Khazendar, A., Schodlok, M.P., Fenty, I., Ligtenberg, S.R.M., Rignot, E. and van den Broeke, M.R. (2013) 'Observed thinning of Totten Glacier is linked to coastal polynya variability', *Nature Communications*, 4(1), 2857.

Kim, K., Jezek, K.C. and Liu, H. (2007) 'Orthorectified image mosaic of Antarctica from 1963 Argon satellite photography: image processing and glaciological applications', *International Journal of Remote Sensing*, 28(23), pp. 5357–5373.

King, M.A., Bingham, R.J., Moore, P., Whitehouse, P.L., Bentley, M.J. and Milne, G.A. (2012) 'Lower satellite-gravimetry estimates of Antarctic sea-level contribution', *Nature*, 491(7425), pp. 586–589.

Kittel, C., Amory, C., Agosta, C., Jourdain, N.C., Hofer, S., Delhasse, A., Doutreloup, S., Huot, P.-V., Lang, C., Fichefet, T. and Fettweis, X. (2021) 'Diverging future surface mass balance between the Antarctic ice shelves and grounded ice sheet', *The Cryosphere*, 15(3), pp. 1215–1236.

Konrad, H., Shepherd, A., Gilbert, L., Hogg, A.E., McMillan, M., Muir, A., and Slater, T. (2018) 'Net retreat of Antarctic glacier grounding lines' Nature Geoscience Vol. 11. pp. 258–262.

Kopp, R.E., Simons, F.J., Mitrovica, J.X., Maloof, A.C. and Oppenheimer, M. (2009) 'Probabilistic assessment of sea level during the last interglacial stage', *Nature*, 462(7275), pp. 863–867.

Kopp, R.E., Simons, F.J., Mitrovica, J.X., Maloof, A.C. and Oppenheimer, M. (2013) 'A probabilistic assessment of sea level variations within the last interglacial stage', *Geophysical Journal International*, 193(2), pp. 711–716.

Kopp, R.E., Simons, F.J., Mitrovica, J.X., Maloof, A.C. and Oppenheimer, M. (2009) 'Probabilistic assessment of sea level during the last interglacial stage', *Nature*, 462(7275), pp. 863–867.

Kowal, K.N., Pegler, S.S. and Worster, M.G. (2016) 'Dynamics of laterally confined marine ice sheets', *Journal of Fluid Mechanics*, 790, pp. R2.

Kulp, S.A. and Strauss, B.H. (2019) 'New elevation data triple estimates of global vulnerability to sea-level rise and coastal flooding', *Nature Communications*, 10(1), pp. 4844.

Leeson, A.A., Forster, E., Rice, A., Gourmelen, N. and van Wessem, J.M. (2020)

'Evolution of Supraglacial Lakes on the Larsen B Ice Shelf in the Decades Before it Collapsed', *Geophysical Research Letters*, 47(4), pp. e2019GL085591.

Leprince, S., Ayoub, F., Klinger, Y. and Avouac, J.-P. (2007) 'Co-Registration of Optically Sensed Images and Correlation (COSI-Corr): an operational methodology for ground deformation measurements', in *2007 IEEE International Geoscience and Remote Sensing Symposium*, pp. 1943–1946.

Levermann, A., Winkelmann, R., Albrecht, T., Goelzer, H., Golledge, N.R., Greve, R., Huybrechts, P., Jordan, J., Leguy, G., Martin, D., Morlighem, M., Pattyn, F., Pollard, D., Quiquet, A., Rodehacke, C., Seroussi, H., Sutter, J., Zhang, T., Van Breedam, J., Calov, R., DeConto, R., Dumas, C., Garbe, J., Gudmundsson, G.H., Hoffman, M.J., Humbert, A., Kleiner, T., Lipscomb, W.H., Meinshausen, M., Ng, E., Nowicki, S.M.J., Perego, M., Price, S.F., Saito, F., Schlegel, N.-J., Sun, S. and van de Wal, R.S.W. (2020) 'Projecting Antarctica's contribution to future sea level rise from basal ice shelf melt using linear response functions of 16 ice sheet models (LARMIP-2)', *Earth System Dynamics*, 11(1), pp. 35–76.

Levy, R., Harwood, D., Florindo, F., Sangiorgi, F., Tripati, R., von Eynatten, H., Gasson, E., Kuhn, G., Tripati, A., DeConto, R., Fielding, C., Field, B., Golledge, N., McKay, R., Naish, T., Olney, M., Pollard, D., Schouten, S., Talarico, F., Warny, S., Willmott, V., Acton, G., Panter, K., Paulsen, T., Taviani, M., and SMS Science Team (2016) 'Antarctic ice sheet sensitivity to atmospheric CO2 variations in the early to mid-Miocene', *Proceedings of the National Academy of Sciences*, 113(13), pp. 3453–3458.

Lewis, A.R., Marchant, D.R., Ashworth, A.C., Hedenäs, L., Hemming, S.R., Johnson, J.V., Leng, M.J., Machlus, M.L., Newton, A.E., Raine, J.I., Willenbring, J.K., Williams, M. and Wolfe, A.P. (2008) 'Mid-Miocene cooling and the extinction of tundra in continental Antarctica', *Proceedings of the National Academy of Sciences*, 105(31), pp. 10676–10680.

Li, T., Dawson, G.J., Chuter, S.J. and Bamber, J.L. (2021) 'ICESat-2-derived grounding zone product for Antarctica'. DOI:10.5523/bris.bnqqyngt89eo26qk8keckglww. [Date Accessed: 25/07/22].

Li, T., Dawson, G.J., Chuter, S.J. and Bamber, J.L. (2022a) 'Grounding line retreat and tide-modulated ocean channels at Moscow University and Totten Glacier ice shelves, East Antarctica', *The Cryosphere Discussions*, [preprint], https://doi.org/10.5194/tc-2022-129.

Li, T., Dawson, G.J., Chuter, S.J. and Bamber, J.L. (2022b) 'A high-resolution Antarctic grounding zone product from ICESat-2 laser altimetry', *Earth System Science Data*, 14(2), pp. 535–557.

Li, X., Rignot, E., Morlighem, M., Mouginot, J., and Scheuchl, B. (2015) 'Grounding Line Retreat of Totten Glacier, 1996 to 2013', *Geophysical research Letters*, 42(19), pp. 8049–8056.

Li, X., Rignot, E., Mouginot, J. and Scheuchl, B. (2016) 'Ice flow dynamics and mass loss of Totten Glacier, East Antarctica, from 1989 to 2015', *Geophysical Research Letters*, 43(12), pp. 6366–6373.

Liebrand, D., de Bakker, A.T.M., Beddow, H.M., Wilson, P.A., Bohaty, S.M., Ruessink, G., Pälike, H., Batenburg, S.J., Hilgen, F.J., Hodell, D.A., Huck, C.E., Kroon, D., Raffi, I., Saes, M.J.M., van Dijk, A.E. and Lourens, L.J. (2017) 'Evolution of the early Antarctic ice ages', *Proceedings of the National Academy of Sciences*, 114(15), pp. 3867–3872.

Liebrand, D., Lourens, L.J., Hodell, D.A., de Boer, B., van de Wal, R.S.W. and Pälike, H. (2011) 'Antarctic ice sheet and oceanographic response to eccentricity forcing during the early Miocene', *Climate of the Past*, 7(3), pp. 869–880.

Lovell, A.M., Stokes, C.R. and Jamieson, S.S.R. (2017) 'Sub-decadal variations in outlet glacier terminus positions in Victoria Land, Oates Land and George V Land, East Antarctica (1972–2013)', *Antarctic Science*, 29(5), pp. 468–483.

Lowry, D.P., Krapp, M., Golledge, N.R. and Alevropoulos-Borrill, A. (2021) 'The influence of emissions scenarios on future Antarctic ice loss is unlikely to emerge this century', *Communications Earth & Environment*, 2(1), pp. 1–14.

Luthcke, S.B., Sabaka, T.J., Loomis, B.D., Arendt, A.A., McCarthy, J.J. and Camp, J. (2013) 'Antarctica, Greenland and Gulf of Alaska land-ice evolution from an iterated GRACE global mascon solution', *Journal of Glaciology*, 59(216), pp. 613–631.

Lüthi, D., Le Floch, M., Bereiter, B., Blunier, T., Barnola, J.-M., Siegenthaler, U., Raynaud, D., Jouzel, J., Fischer, H., Kawamura, K. and Stocker, T.F. (2008) 'High-resolution carbon dioxide concentration record 650,000–800,000 years before present', *Nature*, 453(7193), pp. 379–382.

Martin-Español, A., Bamber, J.L. and Zammit-Mangion, A. (2017) 'Constraining the mass balance of East Antarctica', *Geophysical Research Letters*, 44(9), pp. 4168–4175.

Massom, R.A., Giles, A.B., Fricker, H.A., Warner, R.C., Legrésy, B., Hyland, G., Young, N. and Fraser, A.D. (2010) 'Examining the interaction between multi-year landfast sea ice and the Mertz Glacier Tongue, East Antarctica: Another factor in ice sheet stability?', *Journal of Geophysical Research: Oceans*, 115(C12).

Massom, R.A., Harris, P.T., Michael, K.J. and Potter, M.J. (1998) 'The distribution and formative processes of latent-heat polynyas in East Antarctica', *Annals of Glaciology*, 27, pp. 420–426.

Massom, R.A., Scambos, T.A., Bennetts, L.G., Reid, P., Squire, V.A. and Stammerjohn, S.E. (2018) 'Antarctic ice shelf disintegration triggered by sea ice loss and ocean swell', *Nature*, 558(7710), pp. 383–389.

McKay, N.P., Overpeck, J.T. and Otto-Bliesner, B.L. (2011) 'The role of ocean thermal expansion in Last Interglacial sea level rise', *Geophysical Research Letters*, 38(14).

McMillan, M., Shepherd, A., Sundal, A., Briggs, K., Muir, A., Ridout, A., Hogg, A. and Wingham, D. (2014) 'Increased ice losses from Antarctica detected by CryoSat-2', *Geophysical Research Letters*, 41(11), pp. 3899–3905.

Melsheimer, C. and Spreen, G. (2019) AMSR2 ASI sea ice concentration data, Antarctic, version 5.4 (NetCDF) (July 2012 - December 2018). PANGAEA,

https://doi.org/10.1594/PANGAEA.898400

Mengel, M. and Levermann, A. (2014) 'Ice plug prevents irreversible discharge from East Antarctica', *Nature Climate Change*, 4(6), pp. 451–455.

Mercer, J.H. (1978) 'West Antarctic ice sheet and CO2 greenhouse effect: A threat of disaster', *Nature*, 271(5643), pp. 321–325.

Miles, B.W.J., Jordan, J.R., Stokes, C.R., Jamieson, S.S.R., Gudmundsson, H.G. and Jenkins, A. (2021) 'Recent acceleration of Denman Glacier (1972–2017), East Antarctica, driven by grounding line retreat and changes in ice tongue configuration', *The Cryosphere*, 15(2), pp. 663–676.

Miles, B.W.J., Stokes, C.R. and Jamieson, S.S.R. (2016) 'Pan–ice-sheet glacier terminus change in East Antarctica reveals sensitivity of Wilkes Land to sea-ice changes', *Science Advances*, 2(5), pp. e1501350.

Miles, B.W.J., Stokes, C.R. and Jamieson, S.S.R. (2017) 'Simultaneous disintegration of outlet glaciers in Porpoise Bay (Wilkes Land), East Antarctica, driven by sea ice break-up', *The Cryosphere*, 11(1), pp. 427–442.

Miles, B.W.J., Stokes, C.R. and Jamieson, S.S.R. (2018) 'Velocity increases at Cook Glacier, East Antarctica, linked to ice shelf loss and a subglacial flood event', *The Cryosphere*, 12(10), pp. 3123–3136.

Miles, B.W.J., Stokes, C.R., Jamieson, S.S.R., Jordan, J.R., Gudmundsson, G.H. and Jenkins, A. (2022) 'High spatial and temporal variability in Antarctic ice discharge linked to ice shelf buttressing and bed geometry', *Scientific Reports*, 12(1), pp. 10968.

Miles, B.W.J., Stokes, C.R., Vieli, A. and Cox, N.J. (2013) 'Rapid, climate-driven changes in outlet glaciers on the Pacific coast of East Antarctica', *Nature*, 500(7464), pp. 563–566.

Milillo, P., Rignot, E., Mouginot, J., Scheuchl, B., Morlighem, M., Li, X. and Salzer, J.T. (2017) 'On the Short-term Grounding Zone Dynamics of Pine Island Glacier, West Antarctica, Observed With COSMO-SkyMed Interferometric Data', *Geophysical Research Letters*, 44(20), p. 10,436–10,444.

Milillo, P., Rignot, E., Rizzoli, P., Scheuchl, B., Mouginot, J., Bueso-Bello, J.L., Prats-Iraola, P. and Dini, L. (2022) 'Rapid glacier retreat rates observed in West Antarctica', *Nature Geoscience*, 15(1), pp. 48–53.

Miller, K.G., Kominz, M.A., Browning, J.V., Wright, J.D., Mountain, G.S., Katz, M.E., Sugarman, P.J., Cramer, B.S., Christie-Blick, N. and Pekar, S.F. (2005) 'The Phanerozoic record of global sea-level change', *Science (New York, N.Y.)*, 310(5752), pp. 1293–1298.

Minchew, B.M., Gudmundsson, G.H., Gardner, A.S., Paolo, F.S. and Fricker, H.A. (2018) 'Modeling the dynamic response of outlet glaciers to observed ice-shelf thinning in the Bellingshausen Sea Sector, West Antarctica', *Journal of Glaciology*, 64(244), pp. 333–342.

Mohajerani, Y., Jeong, S., Scheuchl, B., Velicogna, I., Rignot, E. and Milillo, P. (2021) 'Automatic delineation of glacier grounding lines in differential interferometric synthetic-aperture radar data using deep learning', *Scientific Reports*, 11(1), pp. 4992.

Mohajerani, Y., Velicogna, I. and Rignot, E. (2018) 'Mass Loss of Totten and Moscow University Glaciers, East Antarctica, Using Regionally Optimized GRACE Mascons', *Geophysical Research Letters*, 45(14), pp. 7010–7018.

Moon, T. and Joughin, I. (2008) 'Changes in ice front position on Greenland's outlet glaciers from 1992 to 2007', *Journal of Geophysical Research*, 113(F2), F02022.

Moon, T., Joughin, I. and Smith, B. (2015) 'Seasonal to multiyear variability of glacier surface velocity, terminus position, and sea ice/ice mélange in northwest Greenland', *Journal of Geophysical Research: Earth Surface*, 120(5), pp. 818–833.

Morlighem, M. (2020) 'MEaSUREs BedMachine Antarctica, Version 2'. Boulder, Colorado USA. NASA National Snow and Ice Data Center Distributed Active Archive Center. https://doi.org/10.5067/E1QL9HFQ7A8M. [Date Accessed: 10/05/22].

Morlighem, M., Rignot, E., Binder, T., Blankenship, D., Drews, R., Eagles, G., Eisen, O., Ferraccioli, F., Forsberg, R., Fretwell, P., Goel, V., Greenbaum, J.S., Gudmundsson, H., Guo, J., Helm, V., Hofstede, C., Howat, I., Humbert, A., Jokat, W., Karlsson, N.B., Lee, W.S., Matsuoka, K., Millan, R., Mouginot, J., Paden, J., Pattyn, F., Roberts, J., Rosier, S., Ruppel, A., Seroussi, H., Smith, E.C., Steinhage, D., Sun, B., Broeke, M.R. van den, Ommen, T.D. van, Wessem, M. van and Young, D.A. (2020) 'Deep glacial troughs and stabilizing ridges unveiled beneath the margins of the Antarctic ice sheet', *Nature Geoscience*, 13(2), pp. 132–137.

Mouginot, J., Rignot, E. and Scheuchl, B. (2014) 'Sustained increase in ice discharge from the Amundsen Sea Embayment, West Antarctica, from 1973 to 2013', *Geophysical Research Letters*, 41(5), pp. 1576–1584.

Mouginot, J., Rignot, E., Scheuchl, B. and Millan, R. (2017a) 'Comprehensive Annual Ice Sheet Velocity Mapping Using Landsat-8, Sentinel-1, and RADARSAT-2 Data', *Remote Sensing*, 9(4), p. 364.

Mouginot, J., Scheuchl, B. and E. Rignot (2017b) 'MEaSUREs Annual Antarctic Ice Velocity Maps 2005-2017, Version 1' Boulder, Colorado USA. NASA National Snow and Ice Data Center Distributed Active Archive Center. https://doi.org/10.5067/9T4EPQXTJYW9.

Mulvaney, R., Abram, N.J., Hindmarsh, R.C.A., Arrowsmith, C., Fleet, L., Triest, J., Sime, L.C., Alemany, O. and Foord, S. (2012) 'Recent Antarctic Peninsula warming relative to Holocene climate and ice-shelf history', *Nature*, 489, pp. 141–204.

Nagler, T., Rott, H., Hetzenecker, M., Wuite, J. and Potin, P. (2015) 'The Sentinel-1 Mission: New Opportunities for Ice Sheet Observations', *Remote Sensing,* 7(7), pp. 9371–9389.

Nagler, T., Wuite, J., Libert, L., Hetzenecker, M., Keuris, L. and Rott, H. (2021) 'Continuous Monitoring of Ice Motion and Discharge of Antarctic and Greenland Ice Sheets

and Outlet Glaciers by Sentinel-1 A & B', *IGARSS 2021 - 2021 IEEE International Geoscience and Remote Sensing Symposium*, Brussels, Belgium: IEEE, pp. 1061-1064.

Naish, T., Powell, R., Levy, R., Wilson, G., Scherer, R., Talarico, F., Krissek, L., Niessen, F., Pompilio, M., Wilson, T., Carter, L., DeConto, R., Huybers, P., McKay, R., Pollard, D., Ross, J., Winter, D., Barrett, P., Browne, G., Cody, R., Cowan, E., Crampton, J., Dunbar, G., Dunbar, N., Florindo, F., Gebhardt, C., Graham, I., Hannah, M., Hansaraj, D., Harwood, D., Helling, D., Henrys, S., Hinnov, L., Kuhn, G., Kyle, P., Läufer, A., Maffioli, P., Magens, D., Mandernack, K., McIntosh, W., Millan, C., Morin, R., Ohneiser, C., Paulsen, T., Persico, D., Raine, I., Reed, J., Riesselman, C., Sagnotti, L., Schmitt, D., Sjunneskog, C., Strong, P., Taviani, M., Vogel, S., Wilch, T. and Williams, T. (2009) 'Obliquity-paced Pliocene West Antarctic ice sheet oscillations', *Nature*, 458(7236), pp. 322–328.

Naish, T.R., Woolfe, K.J., Barrett, P.J., Wilson, G.S., Atkins, C., Bohaty, S.M., Bücker, C.J., Claps, M., Davey, F.J., Dunbar, G.B., Dunn, A.G., Fielding, C.R., Florindo, F., Hannah, M.J., Harwood, D.M., Henrys, S.A., Krissek, L.A., Lavelle, M., van der Meer, J., McIntosh, W.C., Niessen, F., Passchier, S., Powell, R.D., Roberts, A.P., Sagnotti, L., Scherer, R.P., Strong, C.P., Talarico, F., Verosub, K.L., Villa, G., Watkins, D.K., Webb, P.-N. and Wonik, T. (2001) 'Orbitally induced oscillations in the East Antarctic ice sheet at the Oligocene/Miocene boundary', *Nature*, 413(6857), pp. 719–723.

Nakayama, Y., Greene, C.A., Paolo, F.S., Mensah, V., Zhang, H., Kashiwase, H., Simizu, D., Greenbaum, J.S., Blankenship, D.D., Abe-Ouchi, A. and Aoki, S. (2021) 'Antarctic Slope Current Modulates Ocean Heat Intrusions Towards Totten Glacier', *Geophysical Research Letters*, 48(17), pp. e2021GL094149.

Nias, I.J., Cornford, S.L. and Payne, A.J. (2016) 'Contrasting the modelled sensitivity of the Amundsen Sea Embayment ice streams', *Journal of Glaciology*, 62(233), pp. 552–562.

Nick, F.M., Luckman, A., Vieli, A., Van Der Veen, C.J., Van As, D., Van De Wal, R.S.W., Pattyn, F., Hubbard, A.L. and Floricioiu, D. (2012) 'The response of Petermann Glacier, Greenland, to large calving events, and its future stability in the context of atmospheric and oceanic warming', *Journal of Glaciology*, 58(208), pp. 229–239.

Nihashi, S., Ohshima, K.I. and Tamura, T. (2017) 'Sea-Ice Production in Antarctic Coastal Polynyas Estimated From AMSR2 Data and Its Validation Using AMSR-E and SSM/I-SSMIS Data', *IEEE Journal of Selected Topics in Applied Earth Observations and Remote Sensing*, 10(9), pp. 3912–3922.

Nilsson, J., Gardner, A.S. and Paolo, F.S. (2022) 'Elevation change of the Antarctic Ice Sheet: 1985 to 2020', *Earth System Science Data*, 14(8), pp. 3573–3598.

Nilsson, J., Gardner, A.S., and Paolo, F. S. (2021) 'MEaSUREs ITS_LIVE Antarctic Grounded Ice Sheet Elevation Change, Version 1', Data archived at National Snow and Ice Data Center. DOI:10.5067/L3LSVDZS15ZV. [Date Accessed: 20/05/22].

Nitsche, F.O., Porter, D., Williams, G., Cougnon, E.A., Fraser, A.D., Correia, R. and Guerrero, R. (2017) 'Bathymetric control of warm ocean water access along the East Antarctic Margin', *Geophysical Research Letters*, 44(17), pp. 8936–8944.

Noble, T.L., Rohling, E.J., Aitken, A.R.A., Bostock, H.C., Chase, Z., Gomez, N., Jong, L.M., King, M.A., Mackintosh, A.N., McCormack, F.S., McKay, R.M., Menviel, L., Phipps, S.J., Weber, M.E., Fogwill, C.J., Gayen, B., Golledge, N.R., Gwyther, D.E., Hogg, A.McC., Martos, Y.M., Pena-Molino, B., Roberts, J., van de Flierdt, T. and Williams, T. (2020) 'The Sensitivity of the Antarctic Ice Sheet to a Changing Climate: Past, Present, and Future', *Reviews of Geophysics*, 58(4), pp. e2019RG000663.

O'Leary, M.J., Hearty, P.J., Thompson, W.G., Raymo, M.E., Mitrovica, J.X. and Webster, J.M. (2013) 'Ice sheet collapse following a prolonged period of stable sea level during the last interglacial', *Nature Geoscience*, 6(9), pp. 796–800.

Oppenheimer, M. (1998) 'Global warming and the stability of the West Antarctic Ice Sheet', *Nature*, 393(6683), pp. 325–332.

Orsi, A.H. and Webb, C.J. (2022) 'Impact of Sea Ice Production off Sabrina Coast, East Antarctica', *Geophysical Research Letters*, 49(5), pp. e2021GL095613.

Overpeck, J.T., Otto-Bliesner, B.L., Miller, G.H., Muhs, D.R., Alley, R.B. and Kiehl, J.T. (2006) 'Paleoclimatic Evidence for Future Ice-Sheet Instability and Rapid Sea-Level Rise', *Science*, 311(5768), pp. 1747–1750.

Paolo, F.S., Fricker, H.A. and Padman, L. (2015) 'Volume loss from Antarctic ice shelves is accelerating', *Science*, 348(6232), pp. 327–331.

Pattyn, F. and Morlighem, M. (2020) 'The uncertain future of the Antarctic Ice Sheet', *Science*, 367(6484), pp. 1331–1335.

Payne, A.J., Nowicki, S., Abe-Ouchi, A., Agosta, C., Alexander, P., Albrecht, T., Asay-Davis, X., Aschwanden, A., Barthel, A., Bracegirdle, T.J., Calov, R., Chambers, C., Choi, Y., Cullather, R., Cuzzone, J., Dumas, C., Edwards, T.L., Felikson, D., Fettweis, X., Galton-Fenzi, B.K., Goelzer, H., Gladstone, R., Golledge, N.R., Gregory, J.M., Greve, R., Hattermann, T., Hoffman, M.J., Humbert, A., Huybrechts, P., Jourdain, N.C., Kleiner, T., Munneke, P.K., Larour, E., Le clec'h, S., Lee, V., Leguy, G., Lipscomb, W.H., Little, C.M., Lowry, D.P., Morlighem, M., Nias, I., Pattyn, F., Pelle, T., Price, S.F., Quiquet, A., Reese, R., Rückamp, M., Schlegel, N.-J., Seroussi, H., Shepherd, A., Simon, E., Slater, D., Smith, R.S., Straneo, F., Sun, S., Tarasov, L., Trusel, L.D., Van Breedam, J., van de Wal, R., van den Broeke, M., Winkelmann, R., Zhao, C., Zhang, T. and Zwinger, T. (2021) 'Future Sea Level Change Under Coupled Model Intercomparison Project Phase 5 and Phase 6 Scenarios From the Greenland and Antarctic Ice Sheets', *Geophysical Research Letters*, 48(16), pp. e2020GL091741.

Pegler, S.S. (2016) 'The dynamics of confined extensional flows', *Journal of Fluid Mechanics*, 804, pp. 24–57.

Pegler, S.S. (2018) 'Marine ice sheet dynamics: the impacts of ice-shelf buttressing', *Journal of Fluid Mechanics*, 857, pp. 605–647.

Pelle, T., Morlighem, M., Nakayama, Y. and Seroussi, H. (2021) 'Widespread Grounding Line Retreat of Totten Glacier, East Antarctica, Over the 21st Century', *Geophysical Research Letters*, 48(17), pp. e2021GL093213.

Pollard, D. and DeConto, R.M. (2009) 'Modelling West Antarctic ice sheet growth and collapse through the past five million years', *Nature*, 458(7236), pp. 329–332.

Pollard, D., DeConto, R.M. and Alley, R.B. (2015) 'Potential Antarctic Ice Sheet retreat driven by hydrofracturing and ice cliff failure', *Earth Planet. Sci. Lett.*, 412, pp. 112–121.

Pollard, D., DeConto, R.M. and Nyblade, A.A. (2005) 'Sensitivity of Cenozoic Antarctic ice sheet variations to geothermal heat flux', *Global and Planetary Change*, 49(1), pp. 63–74.

Pope, A., Rees, W.G., Fox, A.J. and Fleming, A. (2014) 'Open Access Data in Polar and Cryospheric Remote Sensing', *Remote Sensing*, 6(7), pp. 6183–6220.

Pritchard, H.D. and Vaughan, D.G. (2007) 'Widespread acceleration of tidewater glaciers on the Antarctic Peninsula', *Journal of Geophysical Research: Earth Surface*, 112(F3).

Pritchard, H.D., Arthern, R.J., Vaughan, D.G. and Edwards, L.A. (2009) 'Extensive dynamic thinning on the margins of the Greenland and Antarctic ice sheets', *Nature*, 461(7266), pp. 971–975.

Pritchard, H.D., Ligtenberg, S.R.M., Fricker, H.A., Vaughan, D.G., van den Broeke, M.R. and Padman, L. (2012) 'Antarctic ice-sheet loss driven by basal melting of ice shelves', *Nature*, 484(7395), pp. 502–505.

Pritchard, H.D., Luthcke, S.B. and Fleming, A.H. (2010) 'Understanding ice-sheet mass balance: progress in satellite altimetry and gravimetry', *Journal of Glaciology*, 56(200), pp. 1151–1161.

Qi, M., Liu, Y., Liu, J., Cheng, X., Lin, Y., Feng, Q., Shen, Q. and Yu, Z. (2021) A 15-year circum-Antarctic iceberg calving dataset derived from continuous satellite observations, Earth Syst. Sci. Data, 13(9), pp. 4583–4601.

Raymo, M.E. and Mitrovica, J.X. (2012) 'Collapse of polar ice sheets during the stage 11 interglacial', *Nature*, 483(7390), pp. 453–456.

Reese, R., Gudmundsson, G.H., Levermann, A. and Winkelmann, R. (2018) 'The far reach of ice-shelf thinning in Antarctica', *Nature Climate Change*, 8(1), pp. 53–57.

Ribeiro, N., Herraiz-Borreguero, L., Rintoul, S.R., McMahon, C.R., Hindell, M., Harcourt, R. and Williams, G. (2021) 'Warm Modified Circumpolar Deep Water Intrusions Drive Ice Shelf Melt and Inhibit Dense Shelf Water Formation in Vincennes Bay, East Antarctica', *Journal of Geophysical Research: Oceans*, 126(8), pp. e2020JC016998.

Rignot E., Mouginot, J. and Scheuchl, B. (2016) 'MEaSUREs Antarctic Grounding Line from Differential Satellite Radar Interferometry', Version 2 Boulder, Colorado, USA: NASA National Snow and Ice Data Center Distributed Active Archive Center. DOI:10.5067/IKBWW4RYHF1Q. [Date Accessed: 20/10/2021].

Rignot E., Mouginot, J. and Scheuchl, B. (2017) MEaSUREs InSAR-Based Antarctica Ice Velocity Map, Version 2. Boulder, Colorado USA. NASA National Snow and Ice Data Center Distributed Active Archive Center. doi: https://doi.org/10.5067/D7GK8F5 J8M8R.

Rignot, E., Casassa, G., Gogineni, P., Krabill, W., Rivera, A. and Thomas, R. (2004), 'Accelerated ice discharge from the Antarctic Peninsula following the collapse of Larsen B Ice Shelf', *Geophysical Research Letters*, 31(18), pp. L18401.

Rignot, E., Jacobs, S., Mouginot, J. and Scheuchl, B. (2013) 'Ice-Shelf Melting Around Antarctica', *Science*, 341(6143), pp. 266–270.

Rignot, E., Mouginot, J. and Scheuchl, B. (2011a) 'Antarctic grounding line mapping from differential satellite radar interferometry', *Geophysical Research Letters*, Vol. 38(10).

Rignot, E., Mouginot, J. and Scheuchl, B. (2011b) 'Ice Flow of the Antarctic Ice Sheet', *Science*, 333(6048), pp. 1427–1430.

Rignot, E., Mouginot, J., Morlighem, M., Seroussi, H. and Scheuchl, B. (2014) 'Widespread, rapid grounding line retreat of Pine Island, Thwaites, Smith, and Kohler glaciers, West Antarctica, from 1992 to 2011', *Geophysical Research Letters*, 41(10), pp. 3502–3509.

Rignot, E., Mouginot, J., Scheuchl, B., van den Broeke, M., van Wessem, M.J. and Morlighem, M. (2019) 'Four decades of Antarctic Ice Sheet mass balance from 1979–2017', *Proceedings of the National Academy of Sciences*, 116(4), pp. 1095–1103.

Rignot, E., Velicogna, I., van den Broeke, M.R., Monaghan, A. and Lenaerts, J.T.M. (2011c) 'Acceleration of the contribution of the Greenland and Antarctic ice sheets to sea level rise', *Geophysical Research Letters*, 38(5), L05503.

Rintoul, S.R., Silvano, A., Pena-Molino, B., van Wijk, E., Rosenberg, M., Greenbaum, J.S. and Blankenship, D.D. (2016) 'Ocean heat drives rapid basal melt of the Totten Ice Shelf', *Science Advances*, 2(12), pp. e1601610.

Ritz, C., Edwards, T.L., Durand, G., Payne, A.J., Peyaud, V. and Hindmarsh, R.C.A. (2015) 'Potential sea-level rise from Antarctic ice-sheet instability constrained by observations', *Nature*, 528(7580), pp. 115–118.

Roberts, J., Galton-Fenzi, B.K., Paolo, F.S., Donnelly, C., Gwyther, D.E., Padman, L., Young, D., Warner, R., Greenbaum, J., Fricker, H.A., Payne, A.J., Cornford, S., Le Brocq, A., van Ommen, T., Blankenship, D. and Siegert, M.J. (2018) 'Ocean forced variability of Totten Glacier mass loss', *Geological Society, London, Special Publications*, 461(1), pp. 175–186.

Roberts, J., Plummer, C., Vance, T., van Ommen, T., Moy, A., Poynter, S., Treverrow, A., Curran, M. and George, S. (2015) 'A 2000-year annual record of snow accumulation rates for Law Dome, East Antarctica', *Climate of the Past*, 11(5), pp. 697–707.

Roberts, J., Warner, R.C., Young, D., Wright, A., van Ommen, T.D., Blankenship, D.D., Siegert, M., Young, N.W., Tabacco, I.E., Forieri, A., Passerini, A., Zirizzotti, A. and Frezzotti, M. (2011) 'Refined broad-scale sub-glacial morphology of Aurora Subglacial Basin, East Antarctica derived by an ice-dynamics-based interpolation scheme', *The Cryosphere*, 5(3), pp. 551–560.

Rott, H., Müller, F., Nagler, T. and Floricioiu, D. (2011) 'The imbalance of glaciers after

disintegration of Larsen-B ice shelf, Antarctic Peninsula', *The Cryosphere*, 5(1), pp. 125–134.

Rovere, A., Raymo, M.E., Mitrovica, J.X., Hearty, P.J., O'Leary, M.J. and Inglis, J.D. (2014) 'The Mid-Pliocene sea-level conundrum: Glacial isostasy, eustasy and dynamic topography', *Earth and Planetary Science Letters*, 387, pp. 27–33.

Royston, S. and Gudmundsson, G.H. (2016) 'Changes in ice-shelf buttressing following the collapse of Larsen A Ice Shelf, Antarctica, and the resulting impact on tributaries', *Journal of Glaciology*, 62(235), pp. 905–911.

Scambos, T. A., Bohlander, J., Shuman, C. A. and Skvarca, P. (2004), 'Glacier acceleration and thinning after ice shelf collapse in the Larsen B embayment, Antarctica', *Geophysical Research Letters*, 31(18), pp. L18402.

Scambos, T., Haran, T.M., Fahnstock, M.A., Painter, T.H., and Bohlander, J. (2007) 'MODIS based Mosaic of Antarctica (MOA) data sets: Continent-wide surface morphology and snow grain size', *Remote Sensing of the Environment*, Vol. 111, pp. 242–257.

Scambos, T., Hulbe, C. and Fahnestock, M. (2003) 'Climate-Induced Ice Shelf Disintegration in the Antarctic Peninsula', in *Antarctic Peninsula Climate Variability: Historical and Paleoenvironmental Perspectives*. American Geophysical Union (AGU), pp. 79–92.

Scambos, T.A., Hulbe, C., Fahnestock, M., and Bohlander, J. (2000) 'The link between climate warming and break-up of ice shelves in the Antarctic Peninsula', *Journal of Glaciology*, 46, pp. 516–530.

Scherer, R.P., Aldahan, A., Tulaczyk, S., Possnert, G., Engelhardt, H. and Kamb, B. (1998) 'Pleistocene Collapse of the West Antarctic Ice Sheet', *Science*, 281(5373), pp. 82–85.

Scherer, R.P., DeConto, R.M., Pollard, D. and Alley, R.B. (2016) 'Windblown Pliocene diatoms and East Antarctic Ice Sheet retreat', *Nature Communications*, 7(1), pp. 12957.

Schodlok, M.P., Menemenlis, D. and Rignot, E.J. (2016) 'Ice shelf basal melt rates around Antarctica from simulations and observations: Ice shelf basal melt around Antarctica', *Journal of Geophysical Research: Oceans*, 121(2), pp. 1085–1109.

Schoof, C. (2007) 'Ice sheet grounding line dynamics: Steady states, stability, and hysteresis', *Journal of Geophysical Research: Earth Surface*, 112(F3).

Schröder, L., Horwath, M., Dietrich, R., Helm, V., van den Broeke, M.R. and Ligtenberg, S.R.M. (2019) 'Four decades of Antarctic surface elevation changes from multi-mission satellite altimetry', *The Cryosphere*, 13(2), pp. 427–449.

Seehaus, T., Cook, A.J., Silva, A.B. and Braun, M. (2018) 'Changes in glacier dynamics in the northern Antarctic Peninsula since 1985', *The Cryosphere*, 12(2), pp. 577–594.

Seroussi, H., Nowicki, S., Payne, A.J., Goelzer, H., Lipscomb, W.H., Abe-Ouchi, A., Agosta, C., Albrecht, T., Asay-Davis, X., Barthel, A., Calov, R., Cullather, R., Dumas,

C., Galton-Fenzi, B.K., Gladstone, R., Golledge, N.R., Gregory, J.M., Greve, R., Hattermann, T., Hoffman, M.J., Humbert, A., Huybrechts, P., Jourdain, N.C., Kleiner, T., Larour, E., Leguy, G.R., Lowry, D.P., Little, C.M., Morlighem, M., Pattyn, F., Pelle, T., Price, S.F., Quiquet, A., Reese, R., Schlegel, N.-J., Shepherd, A., Simon, E., Smith, R.S., Straneo, F., Sun, S., Trusel, L.D., Van Breedam, J., van de Wal, R.S.W., Winkelmann, R., Zhao, C., Zhang, T. and Zwinger, T. (2020) 'ISMIP6 Antarctica: a multi-model ensemble of the Antarctic ice sheet evolution over the 21st century', *The Cryosphere*, 14(9), pp. 3033–3070.

Shen, Q., Wang, H., Shum, C.K., Jiang, L., Hsu, H.T. and Dong, J. (2018) 'Recent high-resolution Antarctic ice velocity maps reveal increased mass loss in Wilkes Land, East Antarctica', *Scientific Reports*, 8(1), pp. 4477.

Shepherd, A., Gilbert, L., Muir, A.S., Konrad, H., McMillan, M., Slater, T., Briggs, K.H., Sundal, A.V., Hogg, A.E. and Engdahl, M.E. (2019) 'Trends in Antarctic Ice Sheet Elevation and Mass', *Geophysical Research Letters*, 46(14), pp. 8174–8183.

Shepherd, A., Ivins, E.R., A, G., Barletta, V.R., Bentley, M.J., Bettadpur, S., Briggs, K.H., Bromwich, D.H., Forsberg, R., Galin, N., Horwath, M., Jacobs, S., Joughin, I., King, M.A., Lenaerts, J.T.M., Li, J., Ligtenberg, S.R.M., Luckman, A., Luthcke, S.B., McMillan, M., Meister, R., Milne, G., Mouginot, J., Muir, A., Nicolas, J.P., Paden, J., Payne, A.J., Pritchard, H., Rignot, E., Rott, H., Sørensen, L.S., Scambos, T.A., Scheuchl, B., Schrama, E.J.O., Smith, B., Sundal, A.V., van Angelen, J.H., van de Berg, W.J., van den Broeke, M.R., Vaughan, D.G., Velicogna, I., Wahr, J., Whitehouse, P.L., Wingham, D.J., Yi, D., Young, D. and Zwally, H.J. (2012) 'A Reconciled Estimate of Ice-Sheet Mass Balance', *Science*, 338(6111), pp. 1183–1189.

Shepherd, A., Wingham, D. and Rignot, E. (2004) 'Warm ocean is eroding West Antarctic Ice Sheet', *Geophys. Res. Lett*., 31, L23402.

Shepherd, A., Wingham, D., Payne, T. and Skvarca, P. (2003) 'Larsen Ice Shelf Has Progressively Thinned', *Science*, 302(5646), pp. 856–859.

Shevenell, A.E., Kennett, J.P. and Lea, D.W. (2008) 'Middle Miocene ice sheet dynamics, deep-sea temperatures, and carbon cycling: A Southern Ocean perspective', *Geochemistry, Geophysics, Geosystems*, 9(2).

Silvano, A., Rintoul, S. R., Kusahara, K., Peña-Molino, B., van Wijk, E., Gwyther, D. E., and Williams, G. D. (2019) 'Seasonality of warm water intrusions onto the continental shelf near the Totten Glacier', *Journal of Geophysical Research: Oceans*, 124(6), pp. 4272–4289.

Silvano, A., Rintoul, S.R., Peña-Molino, B. and Williams, G.D. (2017) 'Distribution of water masses and meltwater on the continental shelf near the Totten and Moscow University ice shelves', *Journal of Geophysical Research: Oceans*, 122(3), pp. 2050–2068.

Silvano, A., Rintoul, S.R., Peña-Molino, B., Hobbs, W.R., van Wijk, E., Aoki, S., Tamura, T. and Williams, G.D. (2018) 'Freshening by glacial meltwater enhances melting of ice shelves and reduces formation of Antarctic Bottom Water', *Science Advances*, 4(4), pp. eaap9467.

Slater, T., Hogg, A. and Mottram, R. (2020) 'Ice-sheet losses track high-end sea-level rise projections', *Nature Climate Change*, 10, pp. 879–881.

Smith, B., Fricker, H.A., Gardner, A.S., Medley, B., Nilsson, J., Paolo, F.S., Holschuh, N., Adusumilli, S., Brunt, K., Csatho, B., Harbeck, K., Markus, T., Neumann, T., Siegfried, M.R. and Zwally, H.J. (2020) 'Pervasive ice sheet mass loss reflects competing ocean and atmosphere processes', *Science*, 368(6496), pp. 1239–1242.

Sole, A., Payne, T., Bamber, J., Nienow, P. and Krabill, W. (2008) 'Testing hypotheses of the cause of peripheral thinning of the Greenland Ice Sheet: is land-terminating ice thinning at anomalously high rates?', *The Cryosphere*, 2, pp. 205–218.

Spence, P., Griffies, S.M., England, M.H., Hogg, A.McC., Saenko, O.A. and Jourdain, N.C. (2014) 'Rapid subsurface warming and circulation changes of Antarctic coastal waters by poleward shifting winds', *Geophysical Research Letters*, 41(13), pp. 4601–4610.

Stammerjohn, S., Maksymm, T., Heil, P. and Massom, R. (2011) 'The influence of winds, sea-surface temperature and precipitation anomalies on Antarctic regional sea-ice conditions during IPY 2007' *Deep-Sea Research Part II: Topical Studies in Oceanography*, 58(9–10), pp. 999–1018.

Steinthorsdottir, M., Coxall, H.K., de Boer, A.M., Huber, M., Barbolini, N., Bradshaw, C.D., Burls, N.J., Feakins, S.J., Gasson, E., Henderiks, J., Holbourn, A.E., Kiel, S., Kohn, M.J., Knorr, G., Kürschner, W.M., Lear, C.H., Liebrand, D., Lunt, D.J., Mörs, T., Pearson, P.N., Pound, M.J., Stoll, H. and Strömberg, C. (2021) 'The Miocene: The Future of the Past', *Paleoceanography and Paleoclimatology*, 36(4), pp. e2020PA004037.

Stokes, C.R., Abram, N.J., Bentley, M.J., Edwards, T.L., England, M.H., Foppert, A., Jamieson, S.S.R., Jones, R.S., King, M.A., Lenaerts, J.T.M., Medley, B., Miles, B.W.J., Paxman, G.J.G., Ritz, C., van de Flierdt, T. and Whitehouse, P.L. (2022) 'Response of the East Antarctic Ice Sheet to past and future climate change', *Nature*, 608(7922), pp. 275–286.

Stokes, C.R., Corner, G.D., Winsborrow, M.C.M., Husum, K. and Andreassen, K. (2014) 'Asynchronous response of marine-terminating outlet glaciers during deglaciation of the Fennoscandian Ice Sheet', *Geology*, 42(5), pp. 455–458.

Stroeven, A.P., Burckle, L.H., Kleman, J. and Prentice, M.L. (1998) 'Atmospheric transport of diatoms in the Sirius Group: Pliocene deepfreeze', *GSA Today*, 8, pp. 1–5.

Sugden, D., Marchant, D., and Denton, G. (1993) 'The Case for a Stable East Antarctic Ice Sheet: The Background', *Geografiska Annaler. Series A, Physical Geography*, 75(4), pp. 151–154.

Sun, S., Cornford, S.L., Gwyther, D.E., Gladstone, R.M., Galton-Fenzi, B.K., Zhao, L. and Moore, J.C. (2016) 'Impact of ocean forcing on the Aurora Basin in the 21st and 22nd centuries', *Annals of Glaciology*, 57(73), pp. 79–86.

Sun, S., Pattyn, F., Simon, E.G., Albrecht, T., Cornford, S., Calov, R., Dumas, C., Gillet-Chaulet, F., Goelzer, H., Golledge, N.R., Greve, R., Hoffman, M.J., Humbert, A.,

Kazmierczak, E., Kleiner, T., Leguy, G.R., Lipscomb, W.H., Martin, D., Morlighem, M., Nowicki, S., Pollard, D., Price, S., Quiquet, A., Seroussi, H., Schlemm, T., Sutter, J., Wal, R.S.W. van de, Winkelmann, R. and Zhang, T. (2020) 'Antarctic ice sheet response to sudden and sustained ice-shelf collapse (ABUMIP)', *Journal of Glaciology*, 66(260), pp. 891–904.

Sutter, J., Eisen, O., Werner, M., Grosfeld, K., Kleiner, T. and Fischer, H. (2020) 'Limited Retreat of the Wilkes Basin Ice Sheet During the Last Interglacial', *Geophysical Research Letters*, 47(13), pp. e2020GL088131.

Sutterley, T.C., Velicogna, I., Rignot, E., Mouginot, J., Flament, T., van den Broeke, M.R., van Wessem, J.M. and Reijmer, C.H. (2014) 'Mass loss of the Amundsen Sea Embayment of West Antarctica from four independent techniques', *Geophysical Research Letters*, 41(23), pp. 8421–8428.

Talley, L.D., Pickard, G.L., Emery, W.J. and Swift, J.H. (2011) 'Physical Properties of Seawater', in *Descriptive Physical Oceanography (Sixth Edition)*. Elsevier, pp. 29–65.

Tamura, T., Ohshima, K.I. and Nihashi, S. (2008) 'Mapping of sea ice production for Antarctic coastal polynyas', *Geophysical Research Letters*, 35(7), L07606.

The IMBIE Team (2018) 'Mass balance of the Antarctic Ice Sheet from 1992 to 2017', *Nature*, 558(7709), pp. 219–222.

The IMBIE Team (2020) 'Mass balance of the Greenland Ice Sheet from 1992 to 2018', *Nature*, 579(7798), pp. 233–239.

Thoma, M., Jenkins, A., Holland, D. and Jacobs, S. (2008) 'Modelling Circumpolar Deep Water intrusions on the Amundsen Sea continental shelf, Antarctica', *Geophys. Res. Lett.*, 35, L18602.

Thompson, A.F., Stewart, A.L., Spence, P. and Heywood, K.J. (2018) 'The Antarctic Slope Current in a Changing Climate', *Reviews of Geophysics*, 56(4), pp. 741–770.

Timmermann, R. and Hellmer, H.H. (2013) 'Southern Ocean warming and increased ice shelf basal melting in the twenty-first and twenty-second centuries based on coupled ice-ocean finite-element modelling', *Ocean Dynamics*, 63(9), pp. 1011–1026.

Trusel, L.D., Das, S.B., Osman, M.B., Evans, M.J., Smith, B.E., Fettweis, X., McConnell, J.R., Noël, B.P.Y. and van den Broeke, M.R. (2018) 'Nonlinear rise in Greenland runoff in response to post-industrial Arctic warming', *Nature*, 564(7734), pp. 104–108.

Turner, J., Orr, A., Gudmundsson, G.H., Jenkins, A., Bingham, R.G., Hillenbrand, C.-D. and Bracegirdle, T.J. (2017) 'Atmosphere-ocean-ice interactions in the Amundsen Sea Embayment, West Antarctica', *Reviews of Geophysics*, 55(1), pp. 235–276.

Turney, C.S.M., Fogwill, C.J., Golledge, N.R., McKay, N.P., van Sebille, E., Jones, R.T., Etheridge, D., Rubino, M., Thornton, D.P., Davies, S.M., Ramsey, C.B., Thomas, Z.A., Bird, M.I., Munksgaard, N.C., Kohno, M., Woodward, J., Winter, K., Weyrich, L.S., Rootes, C.M., Millman, H., Albert, P.G., Rivera, A., van Ommen, T., Curran, M., Moy, A., Rahmstorf, S., Kawamura, K., Hillenbrand, C.-D., Weber, M.E., Manning, C.J., Young,

J. and Cooper, A. (2020) 'Early Last Interglacial ocean warming drove substantial ice mass loss from Antarctica', *Proceedings of the National Academy of Sciences*, 117(8), pp. 3996–4006.

Van Achter, G., Fichefet, T., Goosse, H., Pelletier, C., Sterlin, J., Huot, P.V., Lemieux, J.F., Fraser, A.D., Haubner, K. and Porter-Smith, R. (2022) 'Modelling landfast sea ice and its influence on ocean–ice interactions in the area of the Totten Glacier, East Antarctica', *Ocean Modelling*, 169, 101920.

van den Broeke, M. (2005) 'Strong surface melting preceded collapse of Antarctic Peninsula ice shelf', *Geophysical Research Letters*, 32(12), pp. L12815.

van den Broeke, M., Bamber, J., Ettema, J., Rignot, E., Schrama, E., van de Berg, W.J., van Meijgaard, E., Velicogna, I. and Wouters, B. (2009) 'Partitioning Recent Greenland Mass Loss', *Science*, 326(5955), pp. 984–986.

van Ommen, T.D. and Morgan, V. (2010) 'Snowfall increase in coastal East Antarctica linked with southwest Western Australian drought', *Nature Geoscience*, 3(4), pp. 267–272.

van Wijk, E.M., Rintoul, S.R., Wallace, L.O., Ribeiro, N. and Herraiz-Borreguero, L. (2022) 'Vulnerability of Denman Glacier to Ocean Heat Flux Revealed by Profiling Float Observations', *Geophysical Research Letters*, 49(18), pp. e2022GL100460.

Vaughan, D., Comiso, J., Allison, I., Carrascho, J., Kaser, G., Kwok, R., Mote, P., Murray, T., Paul, F., Ren, J. and Rignot, E. (2013). In T. F. Stocker, D. Qin, G.-K. Plattner, M. Tignor, S. K. Allen, J. Boschung, A. Nauels, Y. Xia, V. Bex, & P. M. Midgeley (Eds.), Observations: Cryosphere. In: Climate change 2013: The physical science basis. *Contribution of Working Group I to the Fifth Assessment Report of the Intergovernmental Panel on Climate Change*. Cambridge, United Kingdom and New York, NY, USA: Cambridge University Press. pp. 317–382.

Vaughan, D.G., Marshall, G.J., Connolley, W.M., King, J.C., and Mulvaney, R. (2001) 'Climate Change: Devil in the Detail', *Science*, 293, pp. 1777–1779.

Velicogna, I. & Wahr, J. (2006) 'Measurements of time-variable gravity show mass loss in Antarctica', *Science,* 311, pp. 1754–1756.

Velicogna, I., Mohajerani, Y., A, G., Landerer, F., Mouginot, J., Noel, B., Rignot, E., Sutterley, T., van den Broeke, M., van Wessem, M. and Wiese, D. (2020) 'Continuity of Ice Sheet Mass Loss in Greenland and Antarctica From the GRACE and GRACE Follow-On Missions', *Geophysical Research Letters*, 47(8), pp. e2020GL087291.

Velicogna, I., Sutterley, T.C. and van den Broeke, M.R. (2014) 'Regional acceleration in ice mass loss from Greenland and Antarctica using GRACE time-variable gravity data', *Geophysical Research Letters*, 41(22), pp. 8130–8137.

Wang, J., Tang, Z., Wilson, D.J., Chang, F., Xiong, Z., Li, D. and Li, T. (2022) 'Ocean-Forced Instability of the West Antarctic Ice Sheet Since the Mid-Pleistocene', *Geochemistry, Geophysics, Geosystems*, 23(9), pp. e2022GC010470.

Wang, L., Davis, J.L. and Howat, I.M. (2021) 'Complex Patterns of Antarctic Ice Sheet

Mass Change Resolved by Time-Dependent Rate Modeling of GRACE and GRACE Follow-On Observations', *Geophysical Research Letters*, 48(1), pp. e2020GL090961.

Wearing, M.G., Kingslake, J. and Worster, M.G. (2020) 'Can unconfined ice shelves provide buttressing via hoop stresses?', *Journal of Glaciology*, 66(257), pp. 349–361.

Webb, P.N., Harwood, D.M., McKelvey, B.C., Mercer, J.H. and Stott, L.D. (1984) 'Cenozoic marine sedimentation and ice-volume variation on the East Antarctic craton', *Geology*, 12(5), pp. 287–291.

Weertman, J. (1974) 'Stability of the Junction of an Ice Sheet and an Ice Shelf', *Journal of Glaciology*, 13(67), pp. 3–11.

Whitehouse, P.L. (2018) 'Glacial isostatic adjustment modelling: historical perspectives, recent advances, and future directions', *Earth Surface Dynamics*, 6(2), pp. 401–429.

Williams, G.D., Meijers, A.J.S., Poole, A., Mathiot, P., Tamura, T., and Klocker, A. (2011) 'Late winter oceanography off the Sabrina and BANZARE coast (117-128 degrees E), East Antarctica', *Deep-Sea Research Part II*, 58, pp. 1194–1210.

Williams, S.D.P., Moore, P., King, M.A. and Whitehouse, P.L. (2014) 'Revisiting GRACE Antarctic ice mass trends and accelerations considering autocorrelation', *Earth and Planetary Science Letters*, 385, pp. 12–21.

Williams, T., van de Flierdt, T., Hemming, S.R., Chung, E., Roy, M. and Goldstein, S.L. (2010) 'Evidence for iceberg armadas from East Antarctica in the Southern Ocean during the late Miocene and early Pliocene', *Earth and Planetary Science Letters*, 290(3–4), pp. 351–361.

Wilson, D.J., Bertram, R.A., Needham, E.F., van de Flierdt, T., Welsh, K.J., McKay, R.M., Mazumder, A., Riesselman, C.R., Jimenez-Espejo, F.J. and Escutia, C. (2018) 'Ice loss from the East Antarctic Ice Sheet during late Pleistocene interglacials', *Nature*, 561(7723), pp. 383–386.

Wilson, G.S., Roberts, A.P., Verosub, K.L., Florindo, F. and Sagnotti, L. (1998) 'Magnetobiostratigraphic chronology of the Eocene—Oligocene transition in the CIROS-1 core, Victoria Land margin, Antarctica: Implications for Antarctic glacial history', *GSA Bulletin*, 110(1), pp. 35–47.

Wouters, B., Martin-Español, A., Helm, V., Flament, T., van Wessem, J.M., Ligtenberg, S.R.M., van den Broeke, M.R. and Bamber, J.L. (2015) 'Dynamic thinning of glaciers on the Southern Antarctic Peninsula', *Science*, 348(6237), pp. 899–903.

Wuite, J., Rott, H., Hetzenecker, M., Floricioiu, D., De Rydt, J., Gudmundsson, G., Nagler, T. and Kern, M. (2015), 'Evolution of surface velocities and ice discharge of Larsen B outlet glaciers from 1995 to 2013', The Cryosphere 9(3), pp. 957–969.

Yamazaki, K., Aoki, S., Katsumata, K., Hirano, D. and Nakayama, Y. (2021) 'Multidecadal poleward shift of the southern boundary of the Antarctic Circumpolar Current off East Antarctica', *Science Advances*, 7(24), pp. eabf8755.

Young, D.A., Wright, A.P., Roberts, J.L., Warner, R.C., Young, N.W., Greenbaum, J.S., Schroeder, D.M., Holt, J.W., Sugden, D.E., Blankenship, D.D., van Ommen, T.D. and Siegert, M.J. (2011) 'A dynamic early East Antarctic Ice Sheet suggested by ice-covered fjord landscapes', *Nature*, 474(7349), pp. 72–75.

Zachos, J.C., Quinn, T.M. and Salamy, K.A. (1996) 'High-resolution (104 years) deep-sea foraminiferal stable isotope records of the Eocene-Oligocene climate transition', *Paleoceanography*, 11(3), pp. 251–266.

Zheng, F., Li, J., Clark, R.T. and Nnamchi, H.C. (2013) 'Simulation and projection of the Southern Hemisphere Annular Mode in CMIP5 models', *Journal of Climate,* 26, pp. 9860–9879.

Zwally, H.J., Giovinetto, M.B., Li, J., Cornejo, H.G., Beckley, M.A., Brenner, A.C., Saba, J.L. and Yi, D. (2005) 'Mass changes of the Greenland and Antarctic ice sheets and shelves and contributions to sea-level rise: 1992–2002', *Journal of Glaciology*, 51(175), pp. 509–527.

Zwally, H.J., Li, J., Robbins, J.W., Saba, J.L., Yi, D. and Brenner, A.C. (2015) 'Mass gains of the Antarctic ice sheet exceed losses', *Journal of Glaciology*, 61(230), pp. 1019–1036.

Zwally, H.J., Robbins, J.W., Luthcke, S.B., Loomis, B.D. and Rémy, F. (2021) 'Mass balance of the Antarctic ice sheet 1992–2016: reconciling results from GRACE gravimetry with ICESat, ERS1/2 and Envisat altimetry', *Journal of Glaciology*, 67(263), pp. 533–559.

Appendix

Supplementary Figure S1. ITS_LIVE (2000 – 2018; Gardner et al., 2018, 2019) and ENVEO (2019 – 2021; ENVEO, 2022) velocity mosaics. The inclusion of velocity values at the base of the DIT between 2019 and 2021 is a result of additional data coverage within the ENVEO mosaics compared to the ITS_LIVE dataset, rather than a terminus advance during this period.

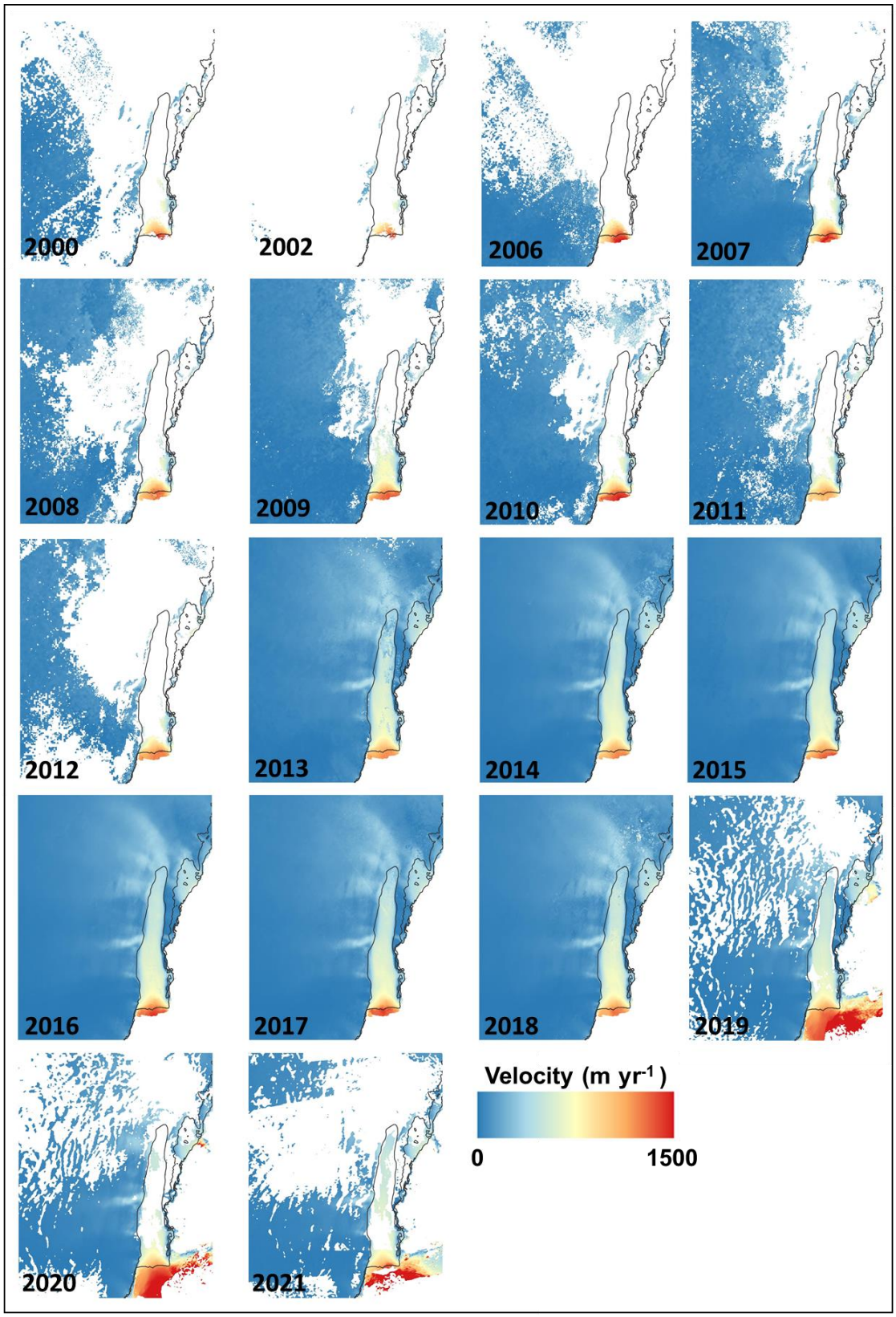

Supplementary Figure S2. (a) Box A average surface elevation change relative to 2013 extracted from the Schröder et al. (2019) dataset with error calculated as standard deviation. (b) Box A average surface elevation change relative to 2010 extracted from the ITS_LIVE dataset with RMSE.

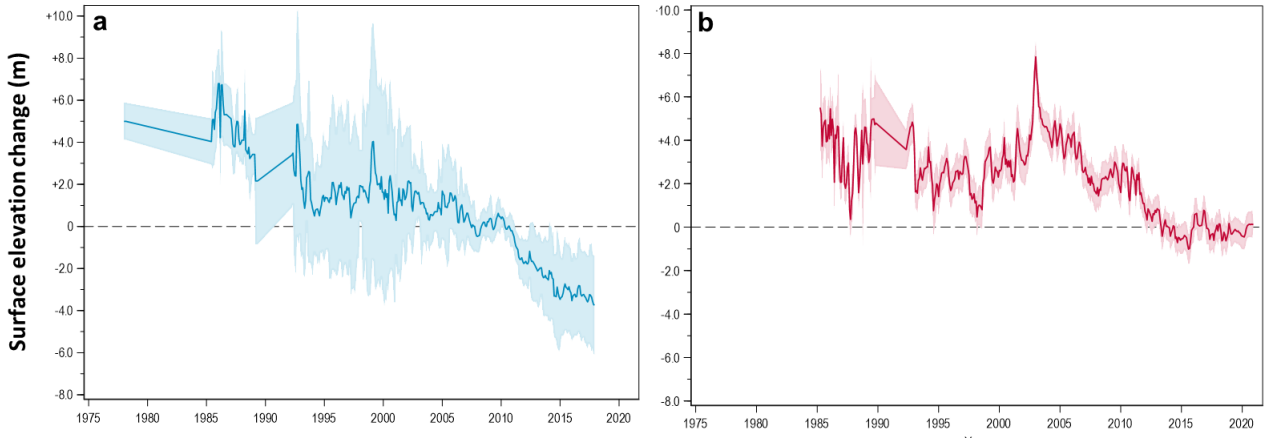

Supplementary Figure S3. (a) Box B average surface elevation change relative to 2013 extracted from the Schröder et al. (2019) dataset with error calculated as standard deviation. (b) Box B average surface elevation change relative to 2010 extracted from the ITS_LIVE dataset with RMSE.

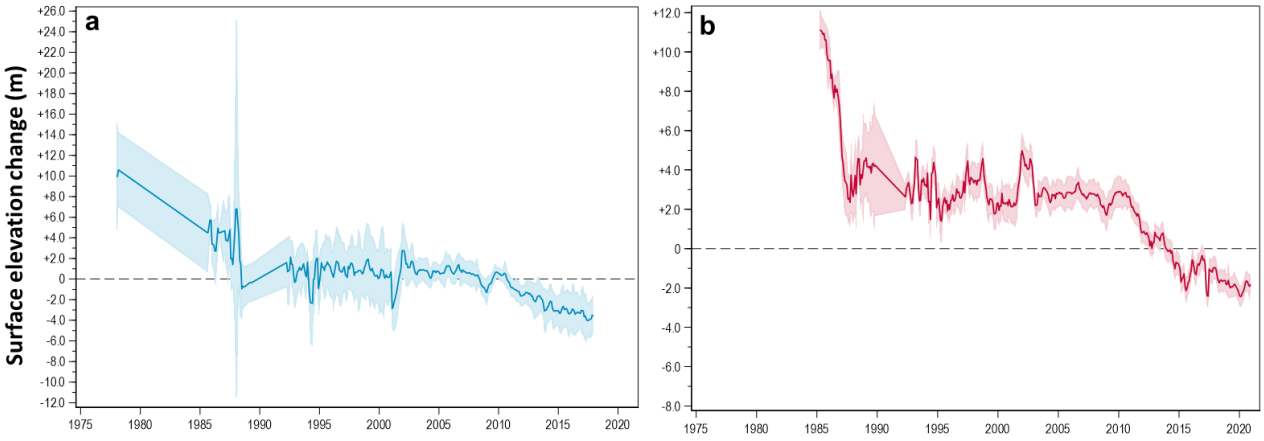

Supplementary Figure S4. (a) Box A and Box B average surface elevation change relative to 2013 extracted from the Schröder et al. (2019) dataset. (b) Box A and Box B average surface elevation change relative to 2010 extracted from the ITS_LIVE dataset.

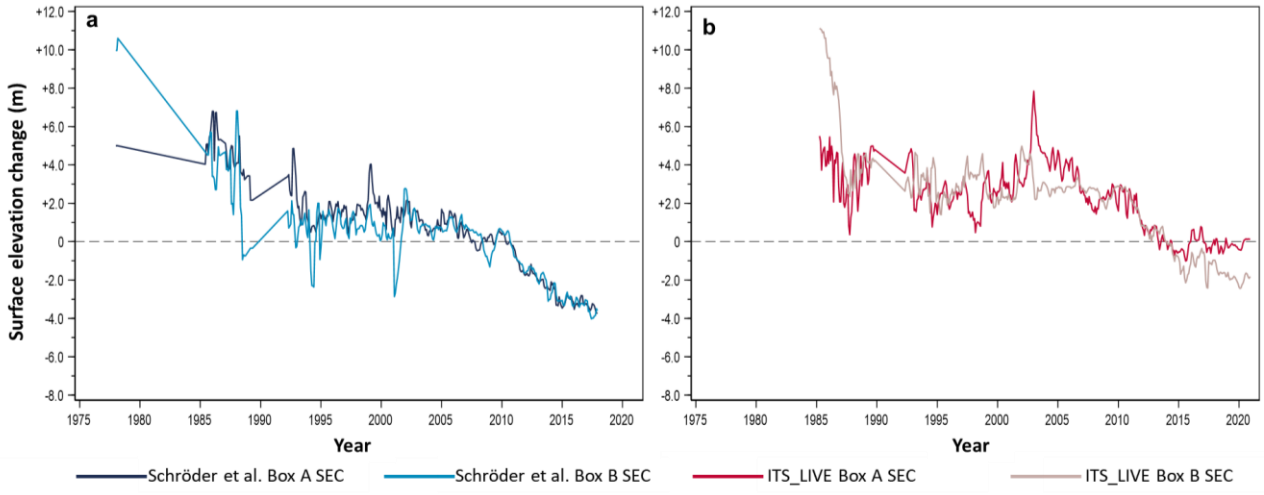

Supplementary Table S1: Overview of satellite imagery sources used in this study and associated error in digitised terminus position. We use Level-1GT Tier 2 Landsat imagery since Level-1TP or Level-1GT Tier 1 products are not available for the required area.

Source	Period	Pixel resolution (m)	Digitised terminus error (m)
Orthorectified Argon Image Mosaic of Antarctica	October 1963	140	±210
RAMP AMM-1 SAR Image Mosaic of Antarctica	September 1997	200	±300
Landsat 1 Multispectral Scanner (MSS) C2 L1GS	1972	60	±90
Landsat 7 Enhanced Thematic Mapper (ETM+) C2 L1GT	2000 – 2012	30	±45
Landsat 8 Operational Land Imager and Thermal Infrared Sensor (OLI/TIRS) C2 L1GT	2013 – 2022	30	±45
Landsat 9 Operational Land Imager and Thermal Infrared Sensor (OLI/TIRS) C2 L1GT	2022	30	±45
Sentinel-2B	2020	10	±15

Supplementary Table S2. Details of satellite imagery used to delineate MUIS terminus position. Where two tiles are listed, the second tile was used to provide complete image coverage where data collection from the majority (first) tile was limited by cloud cover or tile extent.

Year	Date	Sensor	Tile ID
1963	N/A	Argon	N/A
1972	01/12/1972	Landsat 1 MSS C2 L1	LM01_L1GS_103107_19721201_20200909_02_T2
1997	Sept-Oct	RAMP AMM-1 SAR	N/A
2000	03/01/2000	Landsat 7 ETM+ C2 L2	LE07_L2SR_097107_20000103_20200918_02_T2
2001	14/12/2001	Landsat 7 ETM+ C2 L1	LE07_L1GT_098107_20011214_20200917_02_T2
2002	15/11/2002	Landsat 7 ETM+ C2 L2	LE07_L2SR_098108_20021115_20200916_02_T2
2003	04/01/2003 09/01/2003	Landsat 7 ETM+ C2 L1	LE07_L1GT_096107_20030104_20200916_02_T2 LE07_L1GT_099107_20030109_20200916_02_T2
2006	14/12/2006	Landsat 7 ETM+ C2 L1	LE07_L1GT_097107_20061221_20200913_02_T2
2007	20/01/2007 15/01/2007	Landsat 7 ETM+ C2 L1	LE07_L1GT_099107_20070120_20200913_02_T2 LE07_L1GT_096107_20070115_20200913_02_T2
2008	09/01/2008	Landsat 7 ETM+ C2 L1	LE07_L1GT_097107_20080109_20200913_02_T2
2009	02/01/2009	Landsat 7 ETM+ C2 L1	LE07_L1GT_098107_20090102_20200912_02_T2
2010	14/01/2010	Landsat 7 ETM+ C2 L1	LE07_L1GT_097107_20100114_20200911_02_T2
2010	22/02/2010	Landsat 7 ETM+ C2 L1	LE07_L1GT_098107_20100222_20200911_02_T2
2011	26/01/2011 15/01/2011	Landsat 7 ETM+ C2 L1	LE07_L1GT_096107_20110126_20200910_02_T2 LE07_L1GT_099107_20110115_20200910_02_T2
2011	03/12/2011	Landsat 7 ETM+ C2 L1	LE07_L1GT_097107_20111203_20200909_02_T2
2012	04/01/2012	Landsat 7 ETM+ C2 L1	LE07_L1GT_097107_20120104_20200909_02_T2
2012	28/12/2012	Landsat 7 ETM+ C2 L1	LE07_L1GT_098107_20121228_20200908_02_T2
2013	23/12/2013	Landsat 8 OLI/ TRS C2 L1	LC08_L1GT_098107_20131223_20201016_02_T2
2014	01/11/2014	Landsat 8 OLI/ TRS C2 L1	LC08_L1GT_097107_20141101_20201016_02_T2
2015	27/11/2015	Landsat 8 OLI/ TRS C2 L1	LC08_L1GT_098107_20151127_20201016_02_T2
2016	15/02/2016	Landsat 8 OLI/ TRS C2 L1	LC08_L1GT_098107_20160215_20201016_02_T2
2017	23/01/2017	Landsat 8 OLI/ TRS C2 L1	LC08_L1GT_099107_20170123_20201016_02_T2
2018	10/01/2018 05/01/2018	Landsat 8 OLI/ TRS C2 L1	LC08_L1GT_099107_20180110_20201016_02_T2 LC08_L1GT_096107_20180105_20201016_02_T2
2019	06/01/2019	Landsat 8 OLI/ TRS C2 L1	LC08_L1GT_098107_20190106_20201016_02_T2
2020	27/01/2020	Sentinel-2B	T51DVG_20200127T005509

2021	21/02/2021	Landsat 8 OLI/ TRS C2 L1	LC08_L1GT_097107_20210221_20210303_02_T2
2022	30/01/2022	Landsat 8 OLI/ TRS C2 L1	LC08_L1GT_098107_20220130_20220204_02_T2
2022	07/02/2022	Landsat 9 OLI/ TRS C2 L1	LC09_L1GT_098107_20220207_20220207_02_T2
2022	12/03/2022	Landsat 8 OLI/ TRS C2 L1	LC08_L1GT_097107_20220312_20220321_02_T2

Supplementary Table S3. Details of satellite imagery used to delineate ice front positions at Outlet West.

Year	Date	Sensor	Tile ID
1963	N/A	Argon	N/A
1997	Sept-Oct	RAMP AMM-1 SAR	N/A
2000	17/01/2000	Landsat 7 ETM+ C2 L2	LE07_L2SR_099107_20000117_20200918_02_T2
2001	14/12/2001	Landsat 7 ETM+ C2 L1	LE07_L1GT_098107_20011214_20200917_02_T2
2002	15/11/2002	Landsat 7 ETM+ C2 L1	LE07_L1GT_098107_20021115_20200916_02_T2
2003	09/01/2003	Landsat 7 ETM+ C2 L1	LE07_L1GT_099107_20030109_20200916_02_T2
2006	21/12/2006	Landsat 7 ETM+ C2 L1	LE07_L1GT_097107_20061221_20200913_02_T2
2007	20/01/2007	Landsat 7 ETM+ C2 L1	LE07_L1GT_099107_20070120_20200913_02_T2
2008	07/01/2008	Landsat 7 ETM+ C2 L1	LE07_L1GT_099107_20080107_20200913_02_T2
2009	02/01/2009	Landsat 7 ETM+ C2 L1	LE07_L1GT_098107_20090102_20200912_02_T2
2010	14/01/2010	Landsat 7 ETM+ C2 L1	LE07_L1GT_097107_20100114_20200911_02_T2
2011	15/01/2011	Landsat 7 ETM+ C2 L1	LE07_L1GT_099107_20110115_20200910_02_T2
2011	03/12/2011	Landsat 7 ETM+ C2 L1	LE07_L1GT_097107_20111203_20200909_02_T2
2012	04/01/2012	Landsat 7 ETM+ C2 L1	LE07_L1GT_097107_20120104_20200909_02_T2
2012	28/12/2012	Landsat 7 ETM+ C2 L1	LE07_L1GT_098107_20121228_20200908_02_T2
2013	23/12/2013	Landsat 8 OLI/ TRS C2 L1	LC08_L1GT_098107_20131223_20201016_02_T2
2014	15/11/2014	Landsat 8 OLI/ TRS C2 L1	LC08_L1GT_099107_20141115_20201016_02_T2
2015	27/11/2015	Landsat 8 OLI/ TRS C2 L1	LC08_L1GT_098107_20151127_20201016_02_T2
2016	15/02/2016	Landsat 8 OLI/ TRS C2 L1	LC08_L1GT_098107_20160215_20201016_02_T2
2017	23/01/2017	Landsat 8 OLI/ TRS C2 L1	LC08_L1GT_099107_20170123_20201016_02_T2
2018	10/01/2018	Landsat 8 OLI/ TRS C2 L1	LC08_L1GT_099107_20180110_20201016_02_T2
2019	06/01/2019	Landsat 8 OLI/ TRS C2 L1	LC08_L1GT_098107_20190106_20201016_02_T2
2020	01/02/2020	Landsat 8 OLI/ TRS C2 L1	LC08_L1GT_099107_20200201_20201016_02_T2
2021	19/02/2021	Landsat 8 OLI/ TRS C2 L1	LC08_L1GT_099107_20210219_20210302_02_T2
2022	07/02/2022	Landsat 9 OLI/ TRS C2 L1	LC09_L1GT_098107_20220207_20220207_02_T2
2022	09/03/2022	Landsat 9 OLI/ TRS C2 L1	LC09_L1GT_100107_20220309_20220309_02_T2

Supplementary Table S4. Details of satellite imagery used to delineate ice front positions at Outlet East.

Year	Date	Sensor	Tile ID
1963	N/A	Argon	N/A
1997	Sept-Oct	RAMP AMM-1 SAR	N/A
2000	03/01/2000	Landsat 7 ETM+ C2 L2	LE07_L2SR_097107_20000103_20200918_02_T2
2001	14/12/2001	Landsat 7 ETM+ C2 L1	LE07_L1GT_098107_20011214_20200917_02_T2
2002	15/11/2002	Landsat 7 ETM+ C2 L1	LE07_L1GT_098107_20021115_20200916_02_T2
2003	09/01/2003	Landsat 7 ETM+ C2 L1	LE07_L1GT_099107_20030109_20200916_02_T2
2006	21/12/2006	Landsat 7 ETM+ C2 L1	LE07_L1GT_097107_20061221_20200913_02_T2
2007	20/01/2007	Landsat 7 ETM+ C2 L1	LE07_L1GT_099107_20070120_20200913_02_T2
2008	09/01/2008	Landsat 7 ETM+ C2 L1	LE07_L1GT_097107_20080109_20200913_02_T2
2009	02/01/2009	Landsat 7 ETM+ C2 L1	LE07_L1GT_098107_20090102_20200912_02_T2
2010	14/01/2010	Landsat 7 ETM+ C2 L1	LE07_L1GT_097107_20100114_20200911_02_T2
2011	15/01/2011	Landsat 7 ETM+ C2 L1	LE07_L1GT_099107_20110115_20200910_02_T2
2011	03/12/2011	Landsat 7 ETM+ C2 L1	LE07_L1GT_097107_20111203_20200909_02_T2
2012	04/01/2012	Landsat 7 ETM+ C2 L1	LE07_L1GT_097107_20120104_20200909_02_T2
2012	28/12/2012	Landsat 7 ETM+ C2 L1	LE07_L1GT_098107_20121228_20200908_02_T2
2013	23/12/2013	Landsat 8 OLI/ TRS C2 L1	LC08_L1GT_098107_20131223_20201016_02_T2
2014	15/11/2014	Landsat 8 OLI/ TRS C2 L1	LC08_L1GT_099107_20141115_20201016_02_T2
2015	27/11/2015	Landsat 8 OLI/ TRS C2 L1	LC08_L1GT_098107_20151127_20201016_02_T2
2016	15/02/2016	Landsat 8 OLI/ TRS C2 L1	LC08_L1GT_098107_20160215_20201016_02_T2
2017	23/01/2017	Landsat 8 OLI/ TRS C2 L1	LC08_L1GT_099107_20170123_20201016_02_T2
2018	10/01/2018	Landsat 8 OLI/ TRS C2 L1	LC08_L1GT_099107_20180110_20201016_02_T2
2019	06/01/2019	Landsat 8 OLI/ TRS C2 L1	LC08_L1GT_098107_20190106_20201016_02_T2
2020	01/02/2020	Landsat 8 OLI/ TRS C2 L1	LC08_L1GT_099107_20200201_20201016_02_T2
2021	19/02/2021	Landsat 8 OLI/ TRS C2 L1	LC08_L1GT_099107_20210219_20210302_02_T2
2022	07/02/2022	Landsat 9 OLI/ TRS C2 L1	LC09_L1GT_098107_20220207_20220207_02_T2
2022	12/03/2022	Landsat 8 OLI/ TRS C2 L1	LC08_L1GT_097107_20220312_20220321_02_T2

Supplementary Table S5. Details of satellite imagery used to map sea ice presence adjacent to MUIS.

Year	Month	Date	Sensor	Tile ID
1963	Oct	N/A	Argon	N/A
1997	Sept	N/A	RAMP AMM1 V2	N/A
2000	Jan	19/01/2000	Landsat 7 ETM+ C2 L2	LE07_L2SR_097106_20000119_20200918_02_T2
		17/01/2000	Landsat 7 ETM+ C2 L2	LE07_L2SR_099107_20000117_20200918_02_T2
		17/01/2000	Landsat 7 ETM+ C2 L1	LE07_L1GT_099106_20000117_20200918_02_T2
		06/01/2000	Landsat 7 ETM+ C2 L2	LE07_L2SR_102107_20000106_20200918_02_T2
		06/01/2000	Landsat 7 ETM+ C2 L2	LE07_L2SR_102106_20000106_20200918_02_T2
		03/01/2000	Landsat 7 ETM+ C2 L2	LE07_L2SR_097107_20000103_20200918_02_T2
2001	Dec	09/12/2001	Landsat 7 ETM+ C2 L1	LE07_L1GT_095106_20011209_20200917_02_T2
		09/12/2001	Landsat 7 ETM+ C2 L1	LE07_L1GT_095107_20011209_20200917_02_T2
		12/12/2001	Landsat 7 ETM+ C2 L1	LE07_L1GT_100107_20011212_20200917_02_T2
		14/12/2001	Landsat 7 ETM+ C2 L1	LE07_L1GT_098106_20011214_20200917_02_T2
		14/12/2001	Landsat 7 ETM+ C2 L1	LE07_L1GT_098107_20011214_20200917_02_T2
2002	Nov	15/11/2002	Landsat 7 ETM+ C2 L1	LE07_L1GT_098106_20021115_20200916_02_T2
		15/11/2002	Landsat 7 ETM+ C2 L1	LE07_L1GT_098107_20021115_20200916_02_T2
		24/11/2002	Landsat 7 ETM+ C2 L1	LE07_L1GT_097106_20021124_20200916_02_T2
		27/11/2002	Landsat 7 ETM+ C2 L1	LE07_L1GT_102107_20021127_20200916_02_T2
		29/11/2002	Landsat 7 ETM+ C2 L1	LE07_L1GT_100107_20021129_20200916_02_T2
2003	Jan	09/01/2003	Landsat 7 ETM+ C2 L1	LE07_L1GT_099107_20030109_20200916_02_T2
		09/01/2003	Landsat 7 ETM+ C2 L1	LE07_L1GT_099106_20030109_20200916_02_T2
		04/01/2003	Landsat 7 ETM+ C2 L1	LE07_L1GT_096107_20030104_20200916_02_T2
		04/01/2003	Landsat 7 ETM+ C2 L1	LE07_L1GT_096106_20030104_20200916_02_T2
2006	Dec	21/12/2006	Landsat 7 ETM+ C2 L1	LE07_L1GT_097107_20061221_20200913_02_T2
		14/12/2006	Landsat 7 ETM+ C2 L1	LE07_L1GT_096107_20061214_20200913_02_T2
		26/12/2006	Landsat 7 ETM+ C2 L1	LE07_L1GT_100107_20061226_20200913_02_T2
		19/12/2006	Landsat 7 ETM+ C2 L1	LE07_L1GT_099106_20061219_20200913_02_T2
		14/12/2006	Landsat 7 ETM+ C2 L1	LE07_L1GT_096106_20061214_20200913_02_T2
2007	Jan	20/01/2007	Landsat 7 ETM+ C2 L1	LE07_L1GT_099107_20070120_20200913_02_T2
		20/01/2007	Landsat 7 ETM+ C2 L1	LE07_L1GT_099106_20070120_20200913_02_T2
		15/01/2007	Landsat 7 ETM+ C2 L1	LE07_L1GT_096107_20070115_20200913_02_T2
		15/01/2007	Landsat 7 ETM+ C2 L1	LE07_L1GT_096106_20070115_20200913_02_T2
2008	Jan	09/01/2008	Landsat 7 ETM+ C2 L1	LE07_L1GT_097107_20080109_20200913_02_T2
		09/01/2008	Landsat 7 ETM+ C2 L1	LE07_L1GT_097106_20080109_20200913_02_T2
		02/01/2008	Landsat 7 ETM+ C2 L1	LE07_L1GT_096107_20080102_20200913_02_T2
		02/01/2008	Landsat 7 ETM+ C2 L1	LE07_L1GT_096106_20080102_20200913_02_T2
		11/01/2008	Landsat 7 ETM+ C2 L1	LE07_L1GT_095106_20080111_20200913_02_T2
		14/01/2008	Landsat 7 ETM+ C2 L1	LE07_L1GT_100107_20080114_20200913_02_T2
		07/01/2008	Landsat 7 ETM+ C2 L1	LE07_L1GT_099107_20080107_20200913_02_T2
		07/01/2008	Landsat 7 ETM+ C2 L1	LE07_L1GT_099106_20080107_20200913_02_T2
2009	Jan	07/01/2009	Landsat 7 ETM+ C2 L1	LE07_L1GT_101107_20090107_20200912_02_T2
		02/01/2009	Landsat 7 ETM+ C2 L1	LE07_L1GT_098107_20090102_20200912_02_T2
		13/01/2009	Landsat 7 ETM+ C2 L1	LE07_L1GT_095107_20090113_20200912_02_T2
		08/01/2009	Landsat 7 ETM+ C2 L1	LE07_L1GT_092107_20090108_20200912_02_T2
		07/01/2009	Landsat 7 ETM+ C2 L1	LE07_L1GT_101108_20090107_20200912_02_T2
		02/01/2009	Landsat 7 ETM+ C2 L1	LE07_L1GT_098106_20090102_20200912_02_T2

2010	Jan	14/02/2010	Landsat 7 ETM+ C2 L1	LE07_L1GT_097107_20100114_20200911_02_T2
		14/01/2010	Landsat 7 ETM+ C2 L1	LE07_L1GT_097106_20100114_20200911_02_T2
		07/01/2010	Landsat 7 ETM+ C2 L1	LE07_L1GT_096107_20100107_20200911_02_T2
		12/01/2010	Landsat 7 ETM+ C2 L1	LE07_L1GT_099107_20100112_20200911_02_T2
		12/01/2010	Landsat 7 ETM+ C2 L1	LE07_L1GT_099106_20100112_20200911_02_T2
2010	Feb	22/02/2010	Landsat 7 ETM+ C2 L1	LE07_L1GT_098107_20100222_20200911_02_T2
		22/02/2010	Landsat 7 ETM+ C2 L1	LE07_L1GT_098106_20100222_20200911_02_T2
		20/02/2010	Landsat 7 ETM+ C2 L1	LE07_L1GT_100107_20100220_20200911_02_T2
		17/02/2010	Landsat 7 ETM+ C2 L1	LE07_L1GT_095107_20100217_20200911_02_T2
		17/02/2010	Landsat 7 ETM+ C2 L1	LE07_L1GT_095106_20100217_20200911_02_T2
		13/02/2010	Landsat 7 ETM+ C2 L1	LE07_L1GT_099107_20100213_20200911_02_T2
		13/02/2010	Landsat 7 ETM+ C2 L1	LE07_L1GT_099106_20100213_20200911_02_T2
		11/02/2010	Landsat 7 ETM+ C2 L1	LE07_L1GT_101107_20100211_20200911_02_T2
2011	Jan	15/01/2011	Landsat 7 ETM+ C2 L1	LE07_L1GT_099107_20110115_20200910_02_T2
		15/01/2011	Landsat 7 ETM+ C2 L1	LE07_L1GT_099106_20110115_20200910_02_T2
		01/01/2011	Landsat 7 ETM+ C2 L1	LE07_L1GT_097107_20110101_20200910_02_T2
		17/01/2011	Landsat 7 ETM+ C2 L1	LE07_L1GT_097106_20110117_20200910_02_T2
		26/01/2011	Landsat 7 ETM+ C2 L1	LE07_L1GT_096107_20110126_20200910_02_T2
		03/01/2011	Landsat 7 ETM+ C2 L1	LE07_L1GT_095107_20110103_20200910_02_T2
		13/01/2011	Landsat 7 ETM+ C2 L1	LE07_L1GT_101107_20110113_20200910_02_T2
		22/01/2011	Landsat 7 ETM+ C2 L1	LE07_L1GT_100107_20110122_20200910_02_T2
2011	Dec	01/12/2011	Landsat 7 ETM+ C2 L1	LE07_L1GT_099106_20111201_20200909_02_T2
		03/12/2011	Landsat 7 ETM+ C2 L1	LE07_L1GT_097106_20111203_20200909_02_T2
		03/12/2011	Landsat 7 ETM+ C2 L1	LE07_L1GT_097107_20111203_20200909_02_T2
		17/12/2011	Landsat 7 ETM+ C2 L1	LE07_L1GT_099107_20111217_20200909_02_T2
		31/12/2011	Landsat 7 ETM+ C2 L1	LE07_L1GT_101107_20111231_20200909_02_T2
2012	Jan	02/01/2012	Landsat 7 ETM+ C2 L1	LE07_L1GT_099106_20120102_20200909_02_T2
		02/01/2012	Landsat 7 ETM+ C2 L1	LE07_L1GT_099107_20120102_20200909_02_T2
		04/01/2012	Landsat 7 ETM+ C2 L1	LE07_L1GT_097106_20120104_20200909_02_T2
		04/01/2012	Landsat 7 ETM+ C2 L1	LE07_L1GT_097107_20120104_20200909_02_T2
		16/01/2012	Landsat 7 ETM+ C2 L1	LE07_L1GT_101107_20120116_20200909_02_T2
		20/01/2012	Landsat 7 ETM+ C2 L1	LE07_L1GT_097107_20120120_20200909_02_T2
2012		26/12/2012	Landsat 7 ETM+ C2 L1	LE07_L1GT_100106_20121226_20200908_02_T2
		26/12/2012	Landsat 7 ETM+ C2 L1	LE07_L1GT_100107_20121226_20200908_02_T2
		28/12/2012	Landsat 7 ETM+ C2 L1	LE07_L1GT_098106_20121228_20200908_02_T2
		28/12/2012	Landsat 7 ETM+ C2 L1	LE07_L1GT_098107_20121228_20200908_02_T2
		30/12/2012	Landsat 7 ETM+ C2 L1	LE07_L1GT_096106_20121230_20200908_02_T2
2013	Dec	07/12/2013	Landsat 8 OLI/ TRS C2 L1	LC08_L1GT_098106_20131207_20201016_02_T2
		14/12/2013	Landsat 8 OLI/ TRS C2 L1	LC08_L1GT_099107_20131214_20201016_02_T2
		12/12/2013	Landsat 8 OLI/ TRS C2 L1	LC08_L1GT_101107_20131212_20201016_02_T2
		16/12/2013	Landsat 8 OLI/ TRS C2 L1	LC08_L1GT_097108_20131216_20201016_02_T2
		18/12/2013	Landsat 8 OLI/ TRS C2 L1	LC08_L1GT_095107_20131218_20201016_02_T2
		23/12/2013	Landsat 8 OLI/ TRS C2 L1	LC08_L1GT_098107_20131223_20201016_02_T2
		25/12/2013	Landsat 8 OLI/ TRS C2 L1	LO08_L1GT_096106_20131225_20200925_02_T2
2014	Nov	01/11/2014	Landsat 8 OLI/ TRS C2 L1	LC08_L1GT_097107_20141101_20201016_02_T2
		01/11/2014	Landsat 8 OLI/ TRS C2 L1	LC08_L1GT_097108_20141101_20201016_02_T2
		10/11/2014	Landsat 8 OLI/ TRS C2 L1	LC08_L1GT_096107_20141110_20201016_02_T2
		13/11/2014	Landsat 8 OLI/ TRS C2 L1	LC08_L1GT_101107_20141113_20201016_02_T2
		13/11/2014	Landsat 8 OLI/ TRS C2 L1	LC08_L1GT_101108_20141113_20201016_02_T2

		15/11/2014	Landsat 8 OLI/ TRS C2 L1	LC08_L1GT_099106_20141115_20201016_02_T2
		17/11/2014	Landsat 8 OLI/ TRS C2 L1	LC08_L1GT_097106_20141117_20201016_02_T2
		17/11/2014	Landsat 8 OLI/ TRS C2 L1	LC08_L1GT_097107_20141117_20201016_02_T2
2015	Nov	06/11/2015	Landsat 8 OLI/ TRS C2 L1	LC08_L1GT_095107_20151106_20201016_02_T2
		13/11/2015	Landsat 8 OLI/ TRS C2 L1	LC08_L1GT_096106_20151113_20201016_02_T2
		25/11/2015	Landsat 8 OLI/ TRS C2 L1	LC08_L1GT_100106_20151125_20201016_02_T2
		25/11/2015	Landsat 8 OLI/ TRS C2 L1	LC08_L1GT_100107_20151125_20201016_02_T2
		27/11/2015	Landsat 8 OLI/ TRS C2 L1	LC08_L1GT_098106_20151127_20201016_02_T2
		27/11/2015	Landsat 8 OLI/ TRS C2 L1	LC08_L1GT_098107_20151127_20201016_02_T2
2016	Feb	01/02/2016	Landsat 8 OLI/ TRS C2 L1	LC08_L1GT_096107_20160201_20201016_02_T2
		10/02/2016	Landsat 8 OLI/ TRS C2 L1	LC08_L1GT_095106_20160210_20201016_02_T2
		13/02/2016	Landsat 8 OLI/ TRS C2 L1	LC08_L1GT_100107_20160213_20201016_02_T2
		15/02/2016	Landsat 8 OLI/ TRS C2 L1	LC08_L1GT_098106_20160215_20201016_02_T2
		15/02/2016	Landsat 8 OLI/ TRS C2 L1	LC08_L1GT_098107_20160215_20201016_02_T2
		20/02/2016	Landsat 8 OLI/ TRS C2 L1	LC08_L1GT_101107_20160220_20201016_02_T2
		26/02/2016	Landsat 8 OLI/ TRS C2 L1	LC08_L1GT_095107_20160226_20201016_02_T2
2017	Jan	09/01/2017	Landsat 8 OLI/ TRS C2 L1	LC08_L1GT_097106_20170109_20201016_02_T2
		12/01/2017	Landsat 8 OLI/ TRS C2 L1	LC08_L1GT_102106_20170112_20201016_02_T2
		12/01/2017	Landsat 8 OLI/ TRS C2 L1	LC08_L1GT_102107_20170112_20201016_02_T2
		14/01/2017	Landsat 8 OLI/ TRS C2 L1	LC08_L1GT_100107_20170114_20201016_02_T2
		16/01/2017	Landsat 8 OLI/ TRS C2 L1	LC08_L1GT_098106_20170116_20201016_02_T2
		18/01/2017	Landsat 8 OLI/ TRS C2 L1	LC08_L1GT_096108_20170118_20201016_02_T2
		23/01/2017	Landsat 8 OLI/ TRS C2 L1	LC08_L1GT_099107_20170123_20201016_02_T2
		30/01/2017	Landsat 8 OLI/ TRS C2 L1	LC08_L1GT_100106_20170130_20201016_02_T2
2018	Jan	01/01/2018	Landsat 8 OLI/ TRS C2 L1	LC08_L1GT_100106_20180101_20201016_02_T2
		01/01/2018	Landsat 8 OLI/ TRS C2 L1	LC08_L1GT_100107_20180101_20201016_02_T2
		01/01/2018	Landsat 8 OLI/ TRS C2 L1	LC08_L1GT_100108_20180101_20201016_02_T2
		03/01/2018	Landsat 8 OLI/ TRS C2 L1	LC08_L1GT_098106_20180103_20201016_02_T2
		05/01/2018	Landsat 8 OLI/ TRS C2 L1	LC08_L1GT_096107_20180105_20201016_02_T2
		08/01/2018	Landsat 8 OLI/ TRS C2 L1	LC08_L1GT_101107_20180108_20201016_02_T2
		10/01/2018	Landsat 8 OLI/ TRS C2 L1	LC08_L1GT_099107_20180110_20201016_02_T2
		14/01/2018	Landsat 8 OLI/ TRS C2 L1	LC08_L1GT_095106_20180114_20201016_02_T2
2019	Jan	06/01/2019	Landsat 8 OLI/ TRS C2 L1	LC08_L1GT_098106_20190106_20201016_02_T2
		06/01/2019	Landsat 8 OLI/ TRS C2 L1	LC08_L1GT_098107_20190106_20201016_02_T2
		08/01/2019	Landsat 8 OLI/ TRS C2 L1	LC08_L1GT_096106_20190108_20201016_02_T2
		08/01/2019	Landsat 8 OLI/ TRS C2 L1	LC08_L1GT_096107_20190108_20201016_02_T2
		09/01/2019	Landsat 8 OLI/ TRS C2 L1	LC08_L1GT_103107_20190109_20201016_02_T2
		27/01/2019	Landsat 8 OLI/ TRS C2 L1	LC08_L1GT_101106_20190127_20201016_02_T2
		27/01/2019	Landsat 8 OLI/ TRS C2 L1	LC08_L1GT_101107_20190127_20201016_02_T2
2020	Jan	16/01/2020	Sentinel-2B	T50DNM_20200116T022921
		16/01/2020	Sentinel-2B	T50DML_20200116T022921
		17/01/2020	Sentinel-2B	T51DVF_20200117T020111
		26/01/2020	Sentinel-2B	T50DNL_20200126T023015
		27/01/2020	Sentinel-2B	T50DPL_20200127T020127
		27/01/2020	Sentinel-2B	T50DPM_20200127T020127
		27/01/2020	Sentinel-2B	T51DVG_20200127T020127

2020	Feb	01/02/2020	Landsat 8 OLI/ TRS C2 L1	LC08_L1GT_099106_20200201_20201016_02_T2
		01/02/2020	Landsat 8 OLI/ TRS C2 L1	LC08_L1GT_099107_20200201_20201016_02_T2
		03/02/2020	Landsat 8 OLI/ TRS C2 L1	LC08_L1GT_097106_20200203_20201016_02_T2
		03/02/2020	Landsat 8 OLI/ TRS C2 L1	LC08_L1GT_097107_20200203_20201016_02_T2
		15/02/2020	Landsat 8 OLI/ TRS C2 L1	LC08_L1GT_101106_20200215_20201016_02_T2
		22/02/2020	Landsat 8 OLI/ TRS C2 L1	LC08_L1GT_102107_20200222_20201016_02_T2
		29/02/2020	Landsat 8 OLI/ TRS C2 L1	LC08_L1GT_103107_20200229_20201016_02_T2
2021	Feb	17/02/2021	Landsat 8 OLI/ TRS C2 L1	LC08_L1GT_101107_20210217_20210301_02_T2
		19/02/2021	Landsat 8 OLI/ TRS C2 L1	LC08_L1GT_099106_20210219_20210302_02_T2
		19/02/2021	Landsat 8 OLI/ TRS C2 L1	LC08_L1GT_099107_20210219_20210302_02_T2
		21/02/2021	Landsat 8 OLI/ TRS C2 L1	LC08_L1GT_097106_20210221_20210303_02_T2
		21/02/2021	Landsat 8 OLI/ TRS C2 L1	LC08_L1GT_097107_20210221_20210303_02_T2
		23/02/2021	Landsat 8 OLI/ TRS C2 L1	LC08_L1GT_095107_20210223_20210303_02_T2
		24/02/2021	Landsat 8 OLI/ TRS C2 L1	LC08_L1GT_102107_20210224_20210303_02_T2
		28/02/2021	Landsat 8 OLI/ TRS C2 L1	LC08_L1GT_098106_20210228_20210311_02_T2
2022	Feb	06/02/2022	Landsat 8 OLI/ TRS C2 L1	LC08_L1GT_099107_20220206_20220212_02_T2
		07/02/2022	Landsat 9 OLI/ TRS C2 L1	LC09_L1GT_098106_20220207_20220207_02_T2
		07/02/2022	Landsat 9 OLI/ TRS C2 L1	LC09_L1GT_098107_20220207_20220207_02_T2
		20/02/2022	Landsat 8 OLI/ TRS C2 L1	LC08_L1GT_101106_20220220_20220301_02_T2
		20/02/2022	Landsat 8 OLI/ TRS C2 L1	LC08_L1GT_101107_20220220_20220301_02_T2
2022	March	09/03/2022	Landsat 9 OLI/ TRS C2 L1	LC09_L1GT_100106_20220309_20220309_02_T2
		09/03/2022	Landsat 9 OLI/ TRS C2 L1	LC09_L1GT_100107_20220309_20220309_02_T2
		11/03/2022	Landsat 9 OLI/ TRS C2 L1	LC09_L1GT_098108_20220311_20220311_02_T2
		12/03/2022	Landsat 8 OLI/ TRS C2 L1	LC08_L1GT_097106_20220312_20220321_02_T2
		12/03/2022	Landsat 8 OLI/ TRS C2 L1	LC08_L1GT_097107_20220312_20220321_02_T2

Supplementary Table S6. Average ice surface velocity magnitude, associated error and pixel counts within Box A. Pixel counts equal to less than 25% of the total box area are shaded. No data values reflect missing data within the velocity magnitude mosaics.

Year	Mean velocity magnitude (m yr^{-1})	Mean velocity magnitude error (m yr^{-1})	Pixel count (number of pixel values used in velocity average)
2000	-	-	-
2002	-	-	-
2006	-	-	-
2007	-	-	-
2008	-	-	-
2009	-	-	-
2010	291.0783243	900.9062594	782
2011	-	-	-
2012	-	-	-
2013	285.6881152	431.358285	1666
2014	276.5654625	10.09583897	1666
2015	271.2845674	5.062125082	1666
2016	282.5879351	7.518685487	1666
2017	278.1070482	37.25628203	1666
2018	285.0287571	121.6607681	1659
2019	310.6979595	0.090860816	34
2020	-	-	-
2021	-	-	-

Supplementary Table S7. Average ice surface velocity magnitude, associated error and pixel counts within Box B. Pixel counts equal to less than 25% of the total box area are shaded. No data values reflect missing data within the velocity magnitude mosaics.

Year	Mean velocity magnitude (m yr^{-1})	Mean velocity magnitude error (m yr^{-1})	Pixel count (number of pixel values used in velocity average)
2000	-	-	-
2002	-	-	-
2006	-	-	-
2007	-	-	-
2008	-	-	-
2009	-	-	-
2010	416.2737214	175.5204609	534
2011	-	-	-
2012	-	-	-
2013	357.1858658	37.9290315	1662
2014	330.6422297	12.41263903	1667
2015	347.2553	5.298690137	1667
2016	353.322798	7.220002744	1667
2017	328.6950125	26.98999914	1667
2018	339.3371004	151.2364471	1665
2019	339.2101817	0.089203566	357
2020	350.7023711	0.038331018	913
2021	-	-	-

Supplementary Table S8. Average ice surface velocity magnitude, associated error and pixel counts within Box C. All pixel counts are greater than 25% of the total box area. No data values reflect missing data within the velocity magnitude mosaics.

Year	Mean velocity magnitude (m yr^{-1})	Mean velocity magnitude error (m yr^{-1})	Pixel count (number of pixel values used in velocity average)
2000	-	-	-
2002	-	-	-
2006	-	-	-
2007	-	-	-
2008	-	-	-
2009	-	-	-
2010	-	-	-
2011	-	-	-
2012	-	-	-
2013	399.2316684	29.12427533	1668
2014	499.6674615	7.865782769	1668
2015	504.2900397	4.624916942	1668
2016	510.2355223	8.046357182	1668
2017	527.990131	18.57690061	1668
2018	517.4377297	36.51978607	1668
2019	505.1805319	0.036306221	2402
2020	508.8403942	0.040616809	1283
2021	513.8294903	0.035170492	1746

Supplementary Table S9. Average ice surface velocity magnitude, associated error and pixel counts within Box D. Pixel counts equal to less than 25% of the total box area are shaded. No data values reflect missing data within the velocity magnitude mosaics.

Year	Mean velocity magnitude (m yr^{-1})	Mean velocity magnitude error (m yr^{-1})	Pixel count (number of pixel values used in velocity average)
2000	780.8879283	250.7109093	498
2002	823.2770071	30.96250433	33
2006	758.3699828	231.495494	402
2007	738.256	82.0175577	700
2008	716.8001573	56.360702	315
2009	720.708642	91.12706165	1590
2010	723.4922561	94.97099038	735
2011	687.7070901	120.8276786	1111
2012	747.5714477	56.15771169	486
2013	709.4588086	23.87767348	1668
2014	713.7563646	2.560056244	1672
2015	716.6886483	5.852199523	1672
2016	724.8230287	5.852171627	1672
2017	719.8259423	5.318063314	1672
2018	723.0614483	9.138631619	1672
2019	714.4509566	0.053321576	2356
2020	725.4813795	0.049669572	2091
2021	739.9257255	0.048286454	1274

Supplementary Table S10. Average ice surface velocity magnitude, associated error and pixel counts within Box E. Pixel counts equal to less than 25% of the total box area are shaded. No data values reflect missing data within the velocity magnitude mosaics.

Year	Mean velocity magnitude (m yr^{-1})	Mean velocity magnitude error (m yr^{-1})	Pixel count (number of pixel values used in velocity average)
2000	370.2830387	22.73161908	49
2002	410.2706902	29.30149617	20
2006	-	-	-
2007	405.8092178	216.5971544	205
2008	406.2526728	49.3582044	75
2009	414.0346511	94.93103267	94
2010	424.954581	56.03207745	114
2011	436.5997213	123.6912997	128
2012	409.6046002	179.9575773	78
2013	420.6544556	19.76371207	417
2014	397.1413638	4.641600985	417
2015	399.3834446	7.741436316	417
2016	398.4538544	11.87102776	417
2017	400.5769952	7.587453379	417
2018	385.9499589	11.71698747	417
2019	394.5578624	0.041745331	172
2020	394.2924794	0.040087125	275
2021	391.2294118	0.042445863	98